Design and Qualification of a Boundary-Layer Wind Tunnel for Modern CFD Validation Experiments

by

Mark Blanco

Submitted in Partial Fulfillment of the Requirements

for the Degree of

Master of Science in Engineering

in the

Mechanical Engineering

Program

YOUNGSTOWN STATE UNIVERSITY

May, 2019

Design and Qualification of a Boundary-Layer Wind Tunnel
for Modern CFD Validation Experiments

Mark Blanco

Signature:

Mark Blanco, Student Date

Approvals:

Dr. Kevin Disotell, Thesis Advisor Date

Dr. Hazel Marie, Committee Member Date

Dr. Stefan Moldovan, Committee Member Date

Dr. Salvatore A. Sanders, Dean of Graduate Studies Date

ABSTRACT

While computational fluid dynamics (CFD) is an important analytical tool for many aerodynamic applications, experimental wind tunnel analysis is an essential aspect of fully understanding the relevant physics behind many aerodynamic problems. Computational models are presently limited in modeling certain characteristics of turbulence found in many industrial fluid systems. The undertaken study has sought to compute mean flow characteristics of the flow through a low-speed, boundary layer wind tunnel to be built at Youngstown State University, laying the computational framework for future validation experiments of flow systems. Computational investigations were carried out in ANSYS Fluent 19.1 to characterize the expected flow through the tunnel in terms of uniformity, with test section operating velocity as a parameter. A full power examination of the centrifugal blower, located upstream of the test section, was included to ensure that the centrifugal blower will provide the necessary power to meet the desired operating envelope of the tunnel.

A MATLAB program was implemented to calculate the required power of the centrifugal blower based on an array of user-defined inputs, including the tunnel geometry, properties of flow conditioning devices, and air properties. It was determined that the minimum power of a blower to be provided for the facility should be approximately 20 HP, corresponding to an expected free-stream velocity in the test section of nearly 30 m/s.

An important question outlined in the study is how the inflow velocity profiles entering the rectangular contraction affect the characteristics of the flow entering the test section. Various turbulent velocity profiles were considered as boundary conditions for the inlet of the contraction. Both 2-D and 3-D geometries were assessed. For 2-D analysis, the primary concern was diagnosing the sensitivity between the inflow and the outflow boundary-layer properties. A k-ω SST solver was utilized for 2-D computations, which suggested that the boundary layer properties entering the contraction have little to no effect on the boundary layer properties entering the test section. For 3-D analysis, turbulent corner-flow characteristics imposed on the contraction inflow were considered to determine their effect on the flow properties entering the test-section. A Reynolds Stress-BSL solver was deployed for all 3-D computations. The sensitivity of the free-stream was diagnosed by assessing the development of the boundary layer through the contraction as well as the contraction outlet velocity and vorticity profiles. The corner-flow results indicated little to no effect on the boundary layer exiting the contraction. Three distinct test section speeds were considered. The inlet velocities correspond to test section free-stream velocities of 7.5, 15, and 30 m/s. Corresponding Reynolds numbers based on the hydraulic diameter at the outlet of the contraction were 1.83×10^5, 3.65×10^5, and 7.31×10^5.

An *a priori* analysis of the wide-angle diffuser section of the tunnel was carried out, creating foundational data sets for future experimental comparison. The perforated plates in the diffuser section were modeled with a porous-jump boundary condition, used to model the pressure losses associated with these devices for flow-separation control. The Reynolds Stress-BSL model was utilized for diffuser performance analysis, which indicated that the flow modeled in this way—without including the effects of turbulent mixing from the perforated plates which help to control separation—was on the verge of separation across the tunnel operating range considered.

DEDICATION

To Laura,

“When it snows, she has no fear for her household; for all of them are clothed in scarlet”
–Proverbs 31:21

ACKNOWLEDGMENTS

I am grateful for the support of my advisor, Dr. Kevin Disotell, who through the past two years, has helped me develop as a researcher and a writer. I also am very thankful for my committee members, Dr. Stefan Moldovan and Dr. Hazel Marie, who have been instrumental in my technical development.

I will never be able to fully thank my parents, Richard and Laura Blanco, for all of the love and support they have provided me over the years. The moral values instilled in me have had tremendous influence over my life and played a critical role during my development at Youngstown State University. I would also like to thank my wonderful sister, Amanda, who has always had the ability, through conversation, to put everything into perspective.

Finally, I would like to thank the Graduate School and Mechanical Engineering department at Youngstown State University for granting me a Graduate Assistantship throughout my studies, giving me an opportunity to provide research for the school while continuing my education.

TABLE OF CONTENTS

LIST OF FIGURES

LIST OF TABLES

NOMENCLATURE

Variables

A	cross-sectional area of local section (m^2)
A_{Flow}	cross-sectional area of local flow (m^2)
A_o	cross-sectional flow area of test section at upstream end (m^2)
AR	cross-sectional area ratio, $AR = A_2/A_1$
C_2	pressure-jump coefficient (1/m)
c	contraction ratio
D_h	hydraulic diameter (m) , $D_h = 4A/P$
H	shape factor
h_1	height of upstream end of section (m)
h_2	height of downstream end of section (m)
K	local total pressure loss coefficient of section
L	length of centerline across section (m)
l	characteristic length (m)
M	local Mach number
M_o	Mach number at upstream end of test section
P	perimeter (m)
P_{Input}	required power input of the centrifugal blower (W)
p_d	dynamic pressure (kPa)
p_s	static pressure (kPa)
p_t	total pressure (kPa)
Q	volumetric flow rate

Re_{Dh}	Reynolds number based on the hydraulic diameter
Re_L	Reynolds number based on the characteristic length, L
$thickness$	thickness of perforated plate
U_{cl}	mean streamwise velocity computed at tunnel centerline
U_∞	free-stream velocity (m/s)
U_τ	friction velocity (m/s)
V	local flow velocity (m/s)
w_1	width of upstream end of section (m)
w_2	width of downstream end of section (m)
x	streamwise flow direction
y	transverse flow direction
z	spanwise flow direction
α	permeability (m^2)
β	porosity
$\mathit{\Delta}$	surface roughness (m)
Δp	pressure drop across section
ΔS	wall-normal distance
δ^*	displacement thickness (mm)
δ_2	momentum thickness (mm)
δ_p	planarity of diffuser
η_F	aerodynamic efficiency of the blower (percent)
γ	specific heat ratio of gas
λ	friction coefficient for smooth surfaces

μ	dynamic viscosity (N×s/m^2)
ω_z	vorticity about the z-axis
ρ	density of air at rest (kg/m^3)
$\sum_{i=1}^{N} K_{o_i}$	summation of section total pressure losses referenced to test section conditions, with N being the total number of sections.
θ	diffuser half-angle (Rad)
2θ	diffuser equivalent cone angle : $2\,tan^{-1}\left(\frac{\sqrt{A_1}-\sqrt{A_2}}{L\sqrt{\pi}}\right)$, deg

Subscripts

1	upstream end of section
2	downstream end of section
con	contraction section
cl	centerline of wind tunnel
$diff$	diffuser section
$exit$	exit of the tunnel
exp	expansion
$flow$	local flow
$grid$	grid, perforated plate
$honey$	honeycomb section
$Input$	required input of the centrifugal blower
$Mesh$	mesh, screen
o	referenced to test section conditions
$Rectangular$	rectangular cross-section

SC	settling chamber
s	static
$Square$	square cross-section
TS	test section
τ	with respect to shear stress

Superscripts

$\circ$	Degrees
$+$	non-dimensional

Acronyms

AIAA	American Institute of Aeronautics and Astronautics
CAD	Computer-Aided Design
CFD	Computational Fluid Dynamics
DNS	Direct Numerical Simulation
MATLAB	Matrix Laboratory (Software)
NASA	National Aeronautics and Space Administration (United States)
RANS	Reynolds-Averaged Navier Stokes
TMR	Turbulence Modeling Resource, AIAA Turbulence Model Benchmarking Working Group
YSU	Youngstown State University

1 . INTRODUCTION

1.1 Motivation

With the current state of computational fluid dynamics (CFD), a challenge remains to model the physics necessary to fully validate turbulent flows featured in a variety of industrial fluid systems with complex geometries [1]. While CFD can reduce the scope of wind tunnel testing, wind tunnel validation continues to be necessary to evaluate models of complex flow behavior, such as boundary layer transition and separation [1, 2, 3]. In many instances, CFD is most reliable for problems in which there is already a comprehensive understanding [1]. CFD must overcome issues related to numerics, physical modeling, and workflow for grid generation/refinement before wind tunnels will no longer be relied upon for validation data [2]. CFD and experimental results can be compared in carefully-designed test cases, allowing researchers to assess the validity of computed quantities [4]. The aim of this work is to support the qualification of an open-circuit, boundary-layer wind tunnel design for CFD validation studies, laying the foundation for future comparisons with results obtained experimentally.

1.2 Low-Speed Wind Tunnel Design Consideration

The primary objective of most wind tunnels is to obtain well-controlled flow conditions that enable parametric adjustments for studying sensitivities of a given flow i.e. how the turbulence conditions of a flow effect a given system. An example of this would be modifying test section inlet conditions to understand how this alters the underlying physics of a particular flow. For blower driven, open-circuit wind tunnels, the flow exits a centrifugal blower, enters a wide-angle diffuser, then a settling chamber, followed by a contraction section, and finally a test section. Then, the air exits into the laboratory [5]. An example of a blower-driven low-speed wind tunnel is shown in Figure 1.1.

Figure 1.1: Blower-driven wind tunnel (J. Farnsworth [6], used with permission).

There are many design aspects that determine the quality of the flow entering the test section. Design considerations for low speed wind tunnels are provided in great detail by Barlow, Rae, and Pope [5]. Also, design rules for small, low speed wind tunnels are given by Mehta and Bradshaw [7]. The flow through a diffuser depends on the area ratio (AR), the equivalent cone angle (2θ), the wall contour, and the cross-section shape of each end of the diffuser. In the case of open-circuit wind tunnels, wide-angle diffusers are employed, typically between the blower and the settling chamber. Wide-angle diffusers use flow conditioning, such as perforated plates or screens to prevent the boundary layer from separating. Settling chambers typically consist of a honeycomb, followed by screens. Honeycombs remove swirl and lateral mean velocity variations as wells as reduce the turbulence level of the oncoming flow. Contraction design in also important for developing uniform test section flow. Contraction design considerations include but are not limited to, section length (L_c), contraction ratio (c), and the cross-section shape. Another key consideration for wind tunnel design is the size of the test section. Test section selection follows considerations of the Reynolds number capability [5] as well as the scope of the work to be implemented in the facility.

1.3 Target Facility

The motivation for wind tunnel construction in YSU's Flow Physics Laboratory was driven by the need for a research-grade wind tunnel to support a variety of investigations. The immediate investigations include understanding the fundamental physics of turbulent boundary layers common in industrial fluid systems, modeling the instabilities found in turbulent boundary layers, design testing advanced materials and actuators for boundary-layer control, and to contribute to the development of next-generation databases for computer model validation. This objective can only be achieved with the proper facility to support such investigations.

To advance research in the above areas, a blower-driven boundary layer wind tunnel previously located at NASA Ames Research Center and used extensively for various experimental validations in the late 1980s and early 1990s was decided upon for construction at YSU in 2017. The reconstructed tunnel at YSU will match the previous design of the facility as it last existed at NASA Ames Research Center in the late 1990s. In previous studies using this facility, a boundary layer developed on a test plate at a Reynolds number high enough to sustain turbulence and allow accurate experimental measurements, but sufficiently low to be computed with direct numerical simulation (DNS) capabilities of the time [8]. This is an essential feature because the matching of test conditions for computational analysis provided for direct comparison of experimental and computational results. While no turbulence modeling is required for DNS, the technique has not yet become the standard for routine industry workflows since it requires extensive computing power [9]. In addition, DNS solutions are generally considered for flows with low to moderate levels of turbulence [10]. Reynolds-averaged Navier-Stokes (RANS) solvers are far more common for industrial applications due to the low computational cost required for simulation. Resurrection of the wind tunnel will provide future experimental comparisons with turbulence models.

1.4 Boundary Layers

As mentioned in the previous introductory sections, understanding of boundary-layer flows can be supported by a tunnel design of the chosen type. A boundary layer develops when a viscous fluid flows over on a surface. At the surface, the fluid will have no relative motion to the surface, and farther from the surface, the velocity of each layer will increase until reaching the free-stream velocity (U). This behavior is caused by the shear stress acting between fluid layers [11]. A depiction of a boundary layer developing along a flat plate is shown in Figure 1.2. In the figure, τ_w is the shear stress exerted at the wall due to fluid viscosity as a function of streamwise distance (x), U is the free-stream velocity and $\delta(x)$ is the thickness of the boundary layer. The boundary layer can be thought of as blockage through the wind tunnel, as it has a displacement effect on the flow away from the walls. As the boundary layer grows along the walls of the tunnel, the cross-sectional area of the free-stream is reduced, increasing the core velocity through the section. Understanding the boundary layer development throughout the tunnel is paramount in characterizing its operating behavior and implementing appropriate boundary conditions for CFD validation.

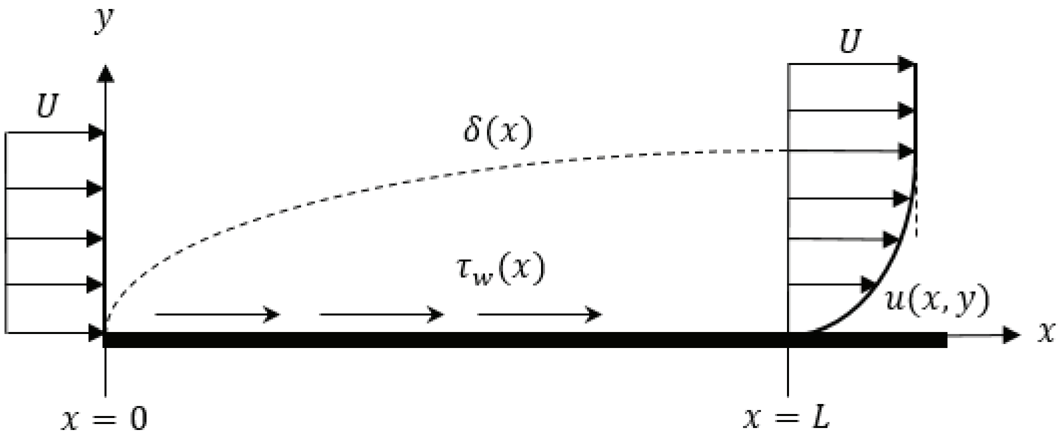

Figure 1.2. Boundary layer development along a flat plate. Adapted from White [12].

Understanding basic boundary layer physics also has industrial applications in many aerodynamic flow problems. In both internal and external flows, detachment of the boundary layer is associated with energy losses leading to increased drag (resistance), flow unsteadiness, and increased wake thickness [13]. Since the boundary layer will respond to environmental factors such as surface roughness and pressure gradients (accelerating or decelerating flow), it is important to understand the properties of the boundary layer to determine where separation may occur, or be on the verge of occurring. Similar problems manifest in other aerodynamic applications. Examples include internal flows, where boundary layer development increases the flow resistance and aircraft wings, where drag is increased and the wing will have a greater resistance to motion. Low-speed wind tunnel testing accompanied by CFD analysis is a necessary source of insight for these types of aerodynamic problems.

1.5 Scope

A full, three-dimensional, mean-flow CFD analysis of the wind tunnel aims to advance current practice in CFD validation experiments by contributing a full quantification of the expected tunnel boundary conditions, providing a basis for future comparison with experimental measurements and expanding upon the methods utilized during the previous lifespan of the wind tunnel.

For CFD validation, essential computed quantities include, but are not limited to, skin friction distribution, surface pressure coefficient distribution, corner flow velocity/vorticity profiles, core flow velocity profiles, and extraction of boundary-layer profiles and thicknesses. Knowledge of these quantities is critical in characterizing test-section entrance conditions that are needed to provide inflow boundary data for CFD cases.

2. WIND TUNNEL BACKROUND

This chapter provides a background of the wind tunnel, explaining the original design and describing how the facility was altered throughout the previous lifespan of the tunnel in arriving at the geometry defined for construction at Youngstown State University.

2.1 Original Geometry

The initial design, provided in detail by Wood and Westphal [14], contained a diffuser attached to the blower exhaust, a settling chamber, and a contraction section. The tunnel was an open circuit design, meaning that the air followed through an essentially straight path and exited into a laboratory. Initially, the contraction section had an overall contraction ratio of 7.5, with a 6.0:1 contraction ratio in the vertical x-y plane and a 1.25:1 contraction ratio in the horizontal x-z plane. The wind tunnel contained three, coarse-mesh, perforated plates. Two plates were located before the diffuser, while the third was located immediately following the diffuser. Wide-angle diffusers are implemented to reduce the length of a diffuser of a given area ratio, and do not necessarily affect pressure recovery [15]. However, perforated plates are implemented to reduced flow angularity and removed total pressure non-uniformities prior to the flow reaching the settling chamber [14]. Within the settling chamber, a honeycomb is installed to remove swirl and lateral mean velocity variations in conditioning the tunnel flow [7]. These considerations provide a more uniform flow, an essential characteristic in any wind tunnel. Following the honeycombs were four stainless steel screens that lead into the contraction section. Screens are used to improve the mean flow uniformity and reduce the intensity of the oncoming turbulence [16]. The contraction section was contoured with symmetric fifth-order polynomials with zero end slope and curvature that provided a reduction in both mean and fluctuating velocity variations to a smaller fraction of the average velocity and increased the flow mean velocity [7]. The contraction section fed directly into a 0.20 × 0.80 × 3.0 m test section. A schematic of the original wind tunnel is displayed in Figure 2.1 and described in Table 2.1. All of the annotations in Figure 2.1 (A-G) correspond to Table 2.1.

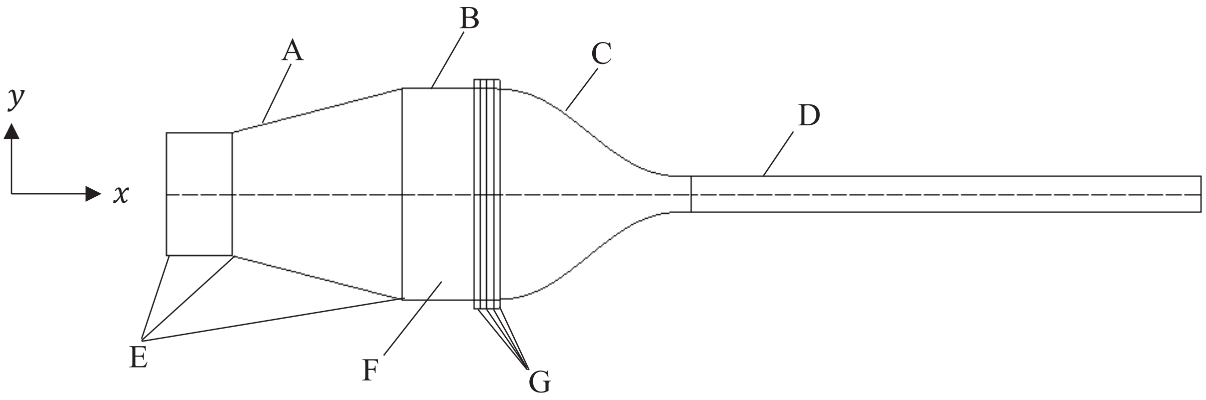

Figure 2.1: Schematic of wind tunnel configuration.

Table 2.1: Original tunnel description from Wood and Westphal [14].

Part	Description (dimensions in cm)
A. Diffuser	Area Ratio: 2.45
	Length: 100
B. Settling Chamber	100 × 120 (A=12,000 cm^2)
	Length: 50
C. Contraction	Area Ratio: 7.5
	Length: 120
	Contours: symmetric fifth-order polynomials with zero end slope and curvature
D. Test Section	Height, width, length: 20 × 80 × 300
E. Grids (three)	Open Area: 64%
	Material: perforated steel plate, 0.16 thickness
	Perforations: 1.27 square, 1.59 center-to-center
F. Honeycomb	Material: 0.0025 wall thickness aluminum
	Cell Size: 0.476 hexagonal section
	Cell Length: 3.8
G. Screens (four)	Open Area: 62.9 %
	Material: 0.0114 stainless steel wire, 32 mesh

2.2 Updated Geometry

Following the initial design, dimensional changes in the contraction and test section were implemented. The updated geometry was implemented to meet the strict requirements necessary for DNS by improving tunnel flow quality in the range supported by simulation [14]. From provisions given by Spalart and Watmuff [8], it is known that a 5:1 (inlet to outlet area-ratio) two-dimensional contraction with exit dimensions of 1.0 by 0.24 m and a new working section (test section) were implemented. The boundary layer developed on a 1.0 m wide by 2.1 m long polished aluminum plate forming the test section floor. A flexible ceiling could produce a tailored pressure distribution in which the boundary layer developed, and two Plexiglas sidewalls completed the test section. This modification allowed for a boundary layer with a Reynolds number high enough to sustain turbulence and allow accurate experimental measurements, but low enough to allow DNS. This property is a key motivation for tunnel reconstruction. The dimensional changes allowed for an investigation into the physics behind a turbulent boundary layer with pressure gradients. Both numerical and experimental approaches were applied during the previous lifespan of the tunnel. The resulting work concluded that the outright comparison of experimental and direct-simulation results, conducted at the same Reynolds number and for a non-trivial turbulent boundary layer, was possible [8]. This work was not continued further on the wind tunnel and with advancements in CFD, a continuation of direct-simulation and experimental result comparison shows promise. Both experimental and computational models are necessary to fully establish understanding of a given flow domain. CFD can allow for solving all flow field quantities at every point in a given domain, but all computational models need to be validated experimentally. Experiments will typically only allow for small measurement regions but are necessary to validate computer models and obtain a more accurate depiction of the underlying physics within a given system. The combination of both computational and experimental results are mutually beneficial for a complete understanding of the flow dynamics within a given system.

2.3 Final Reconstruction Geometry

The reconstructed wind tunnel will consist of the dimensionality given by Spalart and Watmuff [8]. A CAD model of the boundary layer wind tunnel with section labels is shown in Figure 2.2. The altered contraction and test section will provide the necessary boundary layer conditions (i.e. Reynolds numbers high enough to sustain turbulence but low enough for DNS) for experimental and CFD simulation result comparison. This is consistent with the objective of providing the CFD simulation framework necessary for future experimental comparison. The operating envelope of the tunnel will be enhanced. It is known that during the previous lifespan of the wind tunnel, the flow was able to enter the test section with a free-stream velocity of approximately 20 m/s [14]. The reconstructed wind tunnel aims at having an operating envelope that allows for a free-stream velocity in the test section of up to and potentially exceeding 30 m/s. Increasing the speed in the test section increases the Reynolds number range of the tunnel to support a variety of investigations. The operating envelope of the tunnel is driven by the blower located upstream of the test section. The dimensionality of the centrifugal blower at the inlet of the diffuser is a function of the power requirement of the blower. For this reason, power considerations were necessary for determining the exit geometry of the blower. The exit geometry of the blower needed to be adapted to the diffuser inlet, which was determined by reverse-engineering the previous design of the diffuser. A full power analysis is provided with details outlined in Chapter 3.

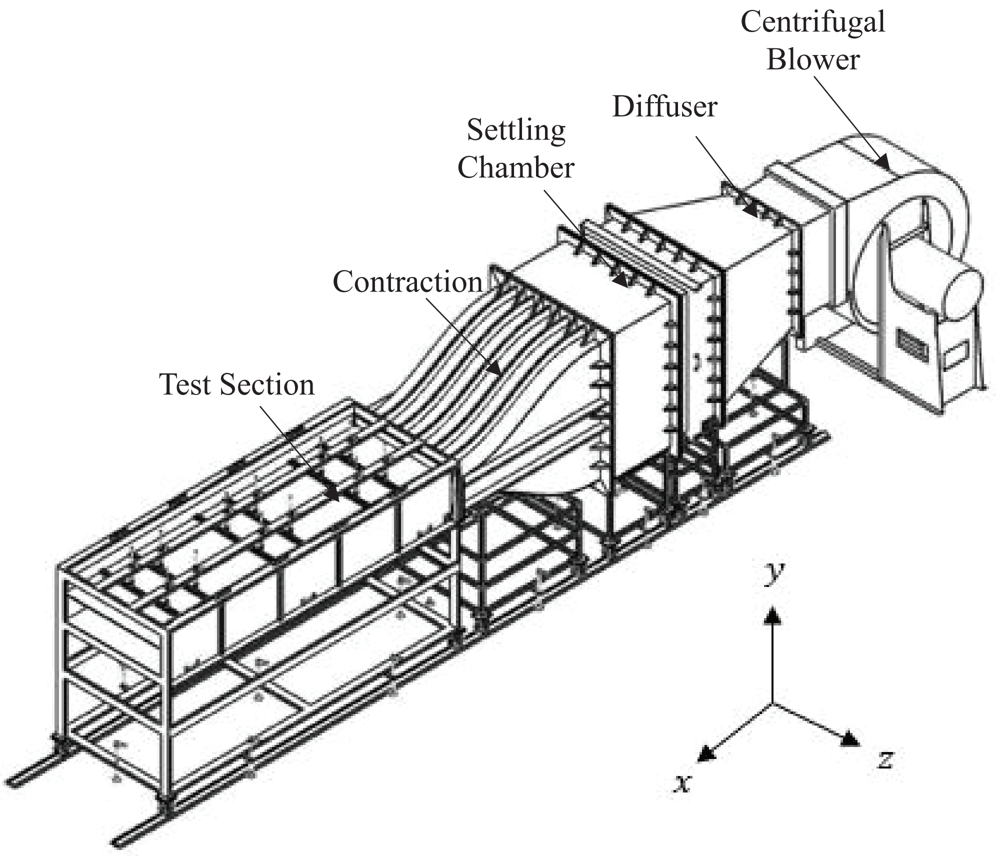

Figure 2.2: Rendering of boundary-layer wind tunnel at YSU [17].

3. POWER CONSIDERATIONS

Considering the overall flow properties of a wind tunnel can provide insight into the power requirements necessary to drive the flow. The power requirement is defined as the necessary power required to drive a desired test section speed. Most types of wind tunnel power analyses are one-dimensional in nature, meaning that the losses are only accounted for along the streamwise flow direction. This introduces some inaccuracy to the power considerations [5]. All the calculations were done with a computer program implemented in MATLAB. The entire program is displayed in Appendix B and a brief description of the program is included in this chapter. This chapter also includes the primary equations that were used to implement the program. All the equations shown in this chapter were provided by Eckert, Mort, and Jope [18]. The purpose of the program is to solve for the required power input of the centrifugal blower based on the pressure losses in each section as well as the operating envelope of the tunnel. The program allows for user-defined inputs so that the power requirement of the blower can be calculated based on wind tunnel conditions defined by the user.

3.1 Governing Loss Equations

The power input required by the centrifugal blower at the entrance of the wind tunnel is dependent upon many factors. The first being the local Reynolds number in each section. The Reynolds number is given by:

$$Re_{D_h} = \frac{\rho V D_h}{\mu} \tag{3.1}$$

where ρ is the local static density, V is the local flow velocity, D_h is the hydraulic diameter, and μ is the dynamic viscosity. Based on the Reynolds number for each section, the friction coefficient (λ) for smooth walls is defined by [18]:

$$\left[log_{10}\left(\lambda {Re_{D_h}}^2\right) - 0.8\right]^{-2} - \lambda = 0. \tag{3.2}$$

Solving for the friction coefficient in each section allows for pressure loss approximations in multiple sections.

3.1.1 Constant Area Ducts

The pressure loss in a constant area-duct and is given by the expression:

$$K = \frac{\lambda L}{D_h} \tag{3.3}$$

where L is the centerline length of the section and D_h is the hydraulic diameter. The pressure loss in the settling chamber is denoted as K_{SC} and the pressure loss in the test section is denoted as K_{TS}.

3.1.2 Contraction

An approximation of the loss in the contraction section, where the majority of the loss is due to frictional effects is given by [18]:

$$K_{con} = 0.32\frac{\lambda L}{D_h} \tag{3.4}$$

where L is the centerline length of the section and D_h is the hydraulic diameter.

3.1.3 Diffuser

A diffuser produces losses for both frictional effects and expansion effects. The severity of the loss in the diffuser is dependent on the geometry of the diffuser. The loss in the duct is given by the expression [18]:

$$K_{Diff} = \left[K_{EXP} + \left(\frac{\lambda}{8\sin\theta}\frac{AR+1}{AR-1}\right)\right]\left(\frac{AR-1}{AR}\right)^2 \tag{3.5}$$

where K_{EXP} is the pressure loss due to the expansion, λ is the friction coefficient in the diffuser, θ is the diffuser half-angle, and AR is the area ratio of the section. The equations used to approximate K_{EXP} are described in Appendix A.

3.1.4 Exit

The total pressure loss at the exit of the wind tunnel is dependent on both the Mach number and the specific heat ratio of the exiting fluid. The expression below accounts for the loss of the kinetic energy of the expelled flow [18]:

$$K_{exit} = \frac{2\left\{\left[1+\left(\frac{\gamma-1}{2}M^2\right)\right]^{\frac{\gamma}{\gamma-1}} - 1\right\}}{\gamma M^2} \tag{3.6}$$

where γ is the specific heat ratio and M is the local Mach number.

3.1.5 Honeycomb

The loss in the honeycomb section is a function of the geometry of the honeycomb as well as the surface roughness of the material that makes up the honeycomb section. The loss is expressed as [18]:

$$K_{honey} = \lambda\left(3+\frac{L}{D_h}\right)\left(\frac{A}{A_{Flow}}\right)^2 + \left(\frac{A}{A_{Flow}}-1\right)^2 \tag{3.7}$$

where A is the cross-sectional area of the local section, D_h is the hydraulic diameter of the honeycomb cell, L is the length of the honeycomb section, A_{Flow} is the cross-sectional area of the flow though the honeycomb, and λ is the skin friction coefficient. For the honeycomb section, the skin friction coefficient is a function of both the Reynolds number and the surface roughness of the material. The skin friction coefficient for the honeycomb section can be approximated using the equations below [18]:

For $Re \leq 275$:
$$\lambda = 0.375\, Re^{-0.1} \left(\frac{\Delta}{D_h}\right)^{0.4} \tag{3.7.1}$$

For $Re > 275$:
$$\lambda = 0.214 \left(\frac{\Delta}{D_h}\right)^{0.4} \tag{3.7.2}$$

where Δ is the surface roughness in the honeycomb cells.

3.1.6 Perforated Plates (Grids)

The loss produced by a perforated plate with a sharp-edged orifice is given by the expression [18]:

$$K_{grid} = \left\{\left[\sqrt{\frac{1}{2}\left(1-\frac{A_{Flow}}{A}\right)} + \left(1-\frac{A_{Flow}}{A}\right)\right]\frac{A}{A_{Flow}}\right\}^{2} \tag{3.8}$$

where A is the cross-sectional area of the local section and A_{Flow} is the cross-sectional area of the local flow through the grid. It is understood that to reduce the pressure losses, the screens must be placed in low-speed sections of the wind tunnel, mainly the diffuser or the settling chamber [19]. To account for the loss of multiple grids in the same section, simply multiply the above expression by the number of grids in that section.

3.1.7 Screens

The loss produced by a screen is expressed as [18]:

$$K_{screen} = K_{Re}K_{Mesh}\left(1 - \frac{A_{Flow}}{A}\right) + \left(\frac{A}{A_{Flow}} - 1\right)^2 \tag{3.9}$$

where K_{Re} is the Reynolds number influence factor and K_{Mesh} is the mesh constant. K_{Mesh} is 1.3 for average circular metal wire, 1.0 for new metal wire, and 2.1 for silk thread. The Reynolds number influence factor is given by the expressions [18]:

For $0 \leq Re < 400$:
$$K_{Re} = \frac{78.5\left(1 - \frac{RN}{354}\right)}{100} + 1.01 \tag{3.9.1}$$

For $Re \geq 400$:
$$K_{Re} = 1.0 \tag{3.9.2}$$

3.1.8 Fan (Power) Section

Fan sections are typically an amalgam of contractions, constant-area ducts, and diffusers. For analysis, the fan section should be divided accordingly.

3.1.9 Referencing Losses to Test Section

All the loss equations expressed to this point are based on local conditions at the smallest-area end of each section. To find the required power input of the centrifugal blower, the losses need to be referenced to the test section conditions. The losses can be referenced to the test section conditions with the expression [18]:

$$K_o = K\left[\frac{A_oM}{AM_o}\sqrt{\frac{1 + \left(\frac{\gamma - 1}{2}M_o{}^2\right)}{1 + \left(\frac{\gamma - 1}{2}M^2\right)}}\right] \tag{3.10}$$

where A_o is the cross sectional flow area of the test section at the upstream end, A is the cross-sectional area of the local section, M_o is the Mach number at the upstream end of the test section, M is the local Mach number, and γ is the specific heat ratio.

3.1.10 Solving for the Required Power Input

The power requirement for the centrifugal blower located at the upstream end of the diffuser is given by the expression [18]:

$$P_{Input} = \frac{\left(\sum_{i=1}^{N} K_{o_i}\right) {\rho_o}^2 A_o {V_o}^3}{2\rho_f \eta_f} \tag{3.11}$$

where $\sum_{i=1}^{N} K_{o_i}$ is the summation of section total pressure losses referenced to test section conditions, ρ_o is the static density at upstream end of test section, A_o is the cross-sectional flow area of test section at upstream end, V_o is the flow velocity at upstream end of test section, ρ_f is the static density at the fans, and η_f is the aerodynamic efficiency of the fan. Assuming that the density of the fluid is constant throughout the wind tunnel ($\rho_o = \rho_f$) will simplify Equation 3.11

3.2 MATLAB Program

The program was used to assess the power necessary to achieve a desired test section operating envelope based on various user-defined inputs. The desired operating envelope of the tunnel has been pushed to minimally 30 m/s in the free-stream of the test section. The program was implemented in MATLAB using the expressions given in Section 3.1. The program requires a vast array of user-defined inputs, allowing the user to define the specific wind tunnel conditions. The inputs include but are not limited to the tunnel geometry, the properties of the fluid, the blower efficiency, the atmospheric pressure, and the properties of the flow conditioners (perforated plates, screens, and honeycomb). The entire program is given in Appendix B. The analysis conducted using the program allowed for choosing a centrifugal blower as well as completing details of the tunnel geometry not explicitly available from literature. This process is outlined in Chapter 4.

4. RECONSTRUCTED DESIGN CALCULATIONS

This chapter aims to provide details of the tunnel that needed clarified from existing knowledge. These details include the power required to operate the tunnel, characteristics of the diffuser, properties of the honeycomb, and the geometry of the contraction. These details are outlined throughout the chapter.

4.1 Upstream Centrifugal Blower

A blower was selected based on the results of the power calculations outlined in Chapter 3. A streamwise velocity (U_{TS}) of 30 m/s in a clean test section (i.e., without any solid blockage from installed test models) was chosen for the power analysis, which is within the characteristic range of low-speed, blower-driven tunnel designs [15]. The power requirement of the blower is 14.052 HP. To err on the side of caution, a factor of safety was implemented in the analysis. The factor of safety consisted of calculating the loss due to a flow obstruction in the test section that spanned the width of the entire section and blocked 30% of the test-section height. This geometry may be implemented for future test models. If this case were to be considered, a test section speed of 30 m/s would still be desired. With this geometry implemented, it was determined that the minimum power of the purchased blower should be approximately 19.703 HP. At a power of 19.703 HP, a test speed of approximately 33.6 m/s can be achieved with no blockage in the tunnel, corresponding to a test section speed of 30 m/s with 30% blockage.

4.2 Diffuser Geometry

The diffuser geometry was selected based on the geometry described during the previous lifespan of the tunnel. The original AR of the diffuser was 2.45 [14]. Based on this, the original inlet cross-sectional area of the diffuser was approximately 0.4898 m^2.

From this insight, along with analysis from the scaled schematic provided by Wood and Westphal [14], it was determined that the original inlet of the diffuser had a dimensionality of approximately 0.880 m (H) × 0.557 m (W). This was not matched exactly due to factors such as the blower geometry found after completing the power analysis, as well as accounting for the expansion angles, θ_{xy} and θ_{xz}, in the diffuser. The expansion angles are sensitive parameters in wide-angle diffuser design. Large expansion angles can lead to flow separation which can cause adverse effects on the flow entering the test section. A wide-angle diffuser is implemented as a means of reducing the length for a given area ratio rather than effecting a pressure recovery [7], which ensures that the boundary layer development of the flow prior to reaching the test section remains small. The design goal of the diffuser is to achieve the largest pressure rise in the shortest distance without out causing the boundary layer to separate. Mehta and Bradshaw [7] have suggested that, for a diffuser with an area ratio less than 5, and a total included angle (θ) less than 50^o (which fits the description of the implemented diffuser), screens or plates should be executed in the diffuser. Therefore, perforated plates have been installed in the diffuser section of the tunnel which is consistent with the details provided by Wood and Westphal [14]. The final dimensionality chosen for the diffuser was 0.807 m (H) × 0.607 (W) m. These dimensions were employed because of both the similarity in surface area to the previous tunnel as well as the symmetric half-angles associated with this dimensionality. The area of the 0.807 m × 0.607 m inlet is 0.4898 m^2. The percent difference between this area and the area of the original diffuser is negligible. A calculation of the symmetric half-angles is shown below. An outlet height of 1.20 m and an inlet height of 0.807 m gives,

$$\theta_{xy} = \tan^{-1}\left(\frac{1.2 - 0.807}{2}\right) = 11.17°. \tag{4.1}$$

Similarly, an outlet width of 1 m and an inlet width of 0.607 m gives,

$$\theta_{xz} = \tan^{-1}\left(\frac{1-0.607}{2}\right) = 11.17°. \tag{4.2}$$

4.3 Honeycomb

Figure 4.1 gives a schematic of the honeycomb. The length and width shown in the figure is not correspondent with the actual geometry of the honeycomb section. The geometry was simplified to calculate the porosity of the honeycomb. The actual honeycomb will fit directly into the settling chamber of the tunnel which is 1m × 1.2m. The honeycomb specifications used in the tunnel match the specifications provided by Wood and Westphal [14]. A table documenting these specs is shown in Table 4.1.

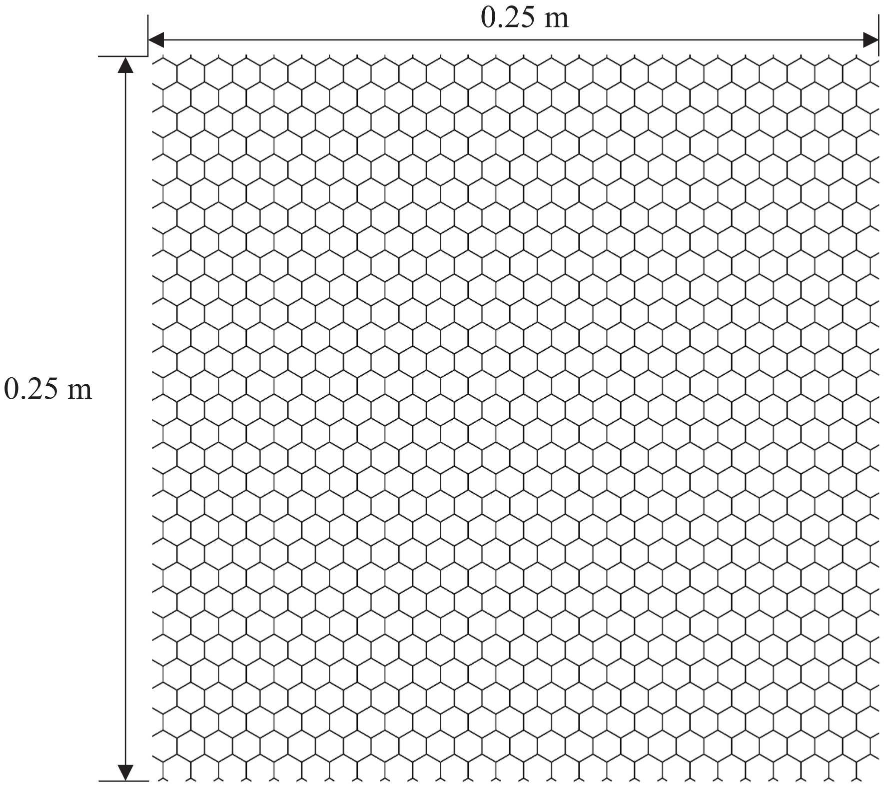

Figure 4.1: Honeycomb schematic**.**

Table 4.1: Honeycomb specifications

Material	Aluminum
Wall Thickness (mm)	0.025
Cell Size (mm)	4.76
Cell Length (mm)	38

The porosity is the measure of empty space in a particular area of material [5]. The porosity, β, is given by the expression

$$\beta = \frac{A_{Flow}}{A} \tag{4.3}$$

Figure 4.1 gives the cross-sectional area of the front face of the honeycomb as approximately 21.08 cm^2. Using this the calculate the open area of the section, A_{Flow}, gives 603.92 cm^2. The total cross-sectional area of the local section, A, would be 625 cm^2. This gives,

$$\beta = \frac{603.92\ cm^2}{625\ cm^2} = 0.966 = 96.6\%$$

4.4 Contraction Geometry

The dimensionality of the contraction section provided by Pook and Watmuff [20] was confirmed to ensure an unambiguous definition. The horizontal length of the contraction was given as 1.524 m and the shape of the contraction fits a 5th order polynomial, similar to the polynomial that defined the original wind tunnel. Equation 4.4 gives the shape of the contraction floor, following the functional form provided by Bell and

Mehta [21].

$$y = 0.3503x^5 - 1.3347x^4 + 1.3561x^3 - 0.6 \tag{4.4}$$

where x and y are in meters, and $0 \leq x \leq 1.524$ m. (To obtain the upper surface, the coefficients above are negated.)

4.5 Selected Power Consideration Outputs

The pressure differential between the internal air of the tunnel (static pressure), run at various flow speeds, and the ambient air in the laboratory (ΔP_s) experienced along the wall of the tunnel are documented in Figure 4.2. The x-axis is non-dimensionalized with respect to the length of the tunnel (L_t). The tunnel spans a total length of 7.069 m. The total pressure was solved for using the loss coefficients outlined in Chapter 3. The velocities assessed correspond to test section free-stream velocities (U_{TS}) of 7.5, 15, and 30 m/s. Corresponding Reynolds numbers based on the hydraulic diameter (Re_{Dh}), calculated using Equation 3.1, at the inlet of the contraction were 1.03×10^5, 2.06×10^5, and 4.12×10^5.

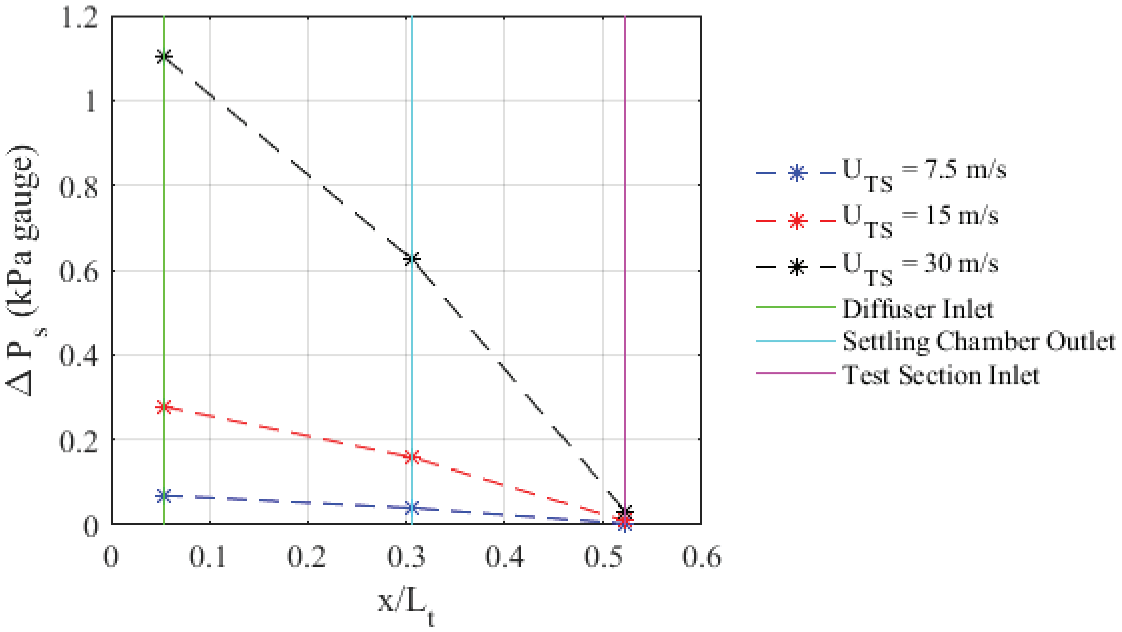

Figure 4.2: Pressure differential across tunnel walls, parameterized by U_{TS}.

Tables 4.2-4.4 display selected outputs from the power analysis carried out in MATLAB. The given outputs were critical in determining the necessary power to drive the tunnel at selected test section speeds. The power input is the power necessary to drive the flow with a clean test section and the power requirement is the power necessary to drive the flow with a 30% blockage in the test section (described in Section 4.1).

Table 4.2: Selected outputs for U_{TS} = 7.5 m/s.

Total K	9.301
Total K_o	2.412
Re_{Dh} at test section inlet	1.827×10^5
Power Input (HP)	0.222
Power Requirement (HP)	0.312

Table 4.3: Selected outputs for U_{TS} = 15 m/s.

Total K	9.289
Total K_o	2.400
Re_{Dh} at test section inlet	3.653×10^5
Power Input (HP)	1.766
Power Requirement (HP)	2.473

Table 4.4: Selected outputs for U_{TS} = 30 m/s.

Total K	9.273
Total K_o	2.386
Re_{Dh} at test section inlet	7.307×10^5
Power Input (HP)	14.052
Power Requirement (HP)	19.703

5. CONTRACTION ANALYSIS NUMERICAL SETUP

Full grid generation and contraction model set-ups have been implemented. Two contraction flow domains (2-D and 3-D) were deployed for analysis. All grids were validated using validation techniques described in detail throughout the chapter. Various velocity profiles were generated for contraction analysis. The motivation for velocity profile generation was to allow for assessment of the sensitivity between the incoming boundary-layer characteristics, specifically the displacement thickness, and the boundary-layer characteristics entering the test section.

ANSYS ICEM 19.1 was used to create the grids and ANSYS Fluent 19.1 was used to obtain the results. Both 2-D and 3-D models were implemented due to the fact that 2-D turbulence results may vary from 3-D analysis [22]. Also, there is evidence of strong secondary flows in the corners of similar wind-tunnels [23] that cannot be assessed in the 2-D model. Various velocity profiles at the inlet of the contraction for both 2-D and 3-D analysis were considered. For 3-D investigations, the corner-flow turbulent characteristics of the tunnel entering the contraction were gauged for their effect on the flow properties entering the test-section. The inflow to the 2-D contraction was supplied by a series of 2-D flat-plate, zero-pressure gradient cases to vary the incoming boundary layer. The inflow to the 3-D contraction was supplied by a series of rectangular duct velocity profiles, used to vary the magnitude of the corner-flow effects entering the contraction. For 2-D computation, the k-ω SST model was selected for a steady analysis. The k-ω SST model is typically accurate in calculating wall boundary-layer characteristics [24]. For 3-D computations, the Reynolds-Stress BSL model was selected for steady analysis. The Reynolds-Stress BSL model has capabilities of solving for important turbulence flow characteristics such as the anisotropy in the normal stresses [25], justifying its use in calculating 3-D characteristics that the standard k-ω model would not capture. The Reynolds-Stress BSL model consists of accurate and robust performance in solving for turbulent boundary layer properties [26]. Both 3-D and 2-D pressure-based, coupled solvers were implemented with second-order upwind differencing for pressure and third-order Monotonic Upwind Scheme for Conservation Laws (MUSCL) momentum differencing. Various inlet flow velocities were considered. The inlet velocities correspond to test section free-stream velocities (U_{TS}) of 7.5, 15, and 30 m/s. Corresponding Reynolds numbers based on the hydraulic diameter (Re_{Dh}), calculated using Equation 3.1, at the inlet of the contraction are 1.03×10^5, 2.06×10^5, and 4.12×10^5.

5.1 Contraction Grid and Model Generation

Figure 5.1 displays the non-dimensional geometry of the 2-D contraction grid with corresponding 2-D boundary conditions. The inlet extended 200 mm ahead of the start of the contraction, and the outlet extended 476 mm after the end of the contraction polynomial given in Equation 4.4. Half of the total 2-D geometry and one-fourth of the total 3-D geometry were modeled by invoking symmetry planes.

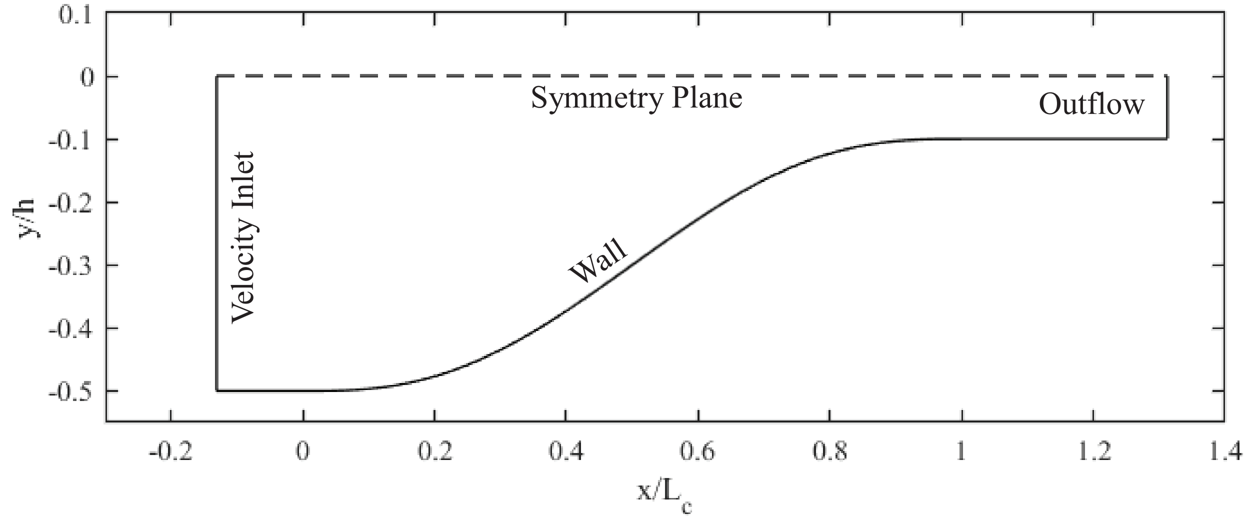

Figure 5.1: Geometry of 2-D contraction domain with boundary conditions.

Figure 5.2 displays the grid used for 3-D analysis of the contraction flow as well as the boundary conditions employed in the contraction for the 3-D domain. The boundary conditions for 3-D analysis were similar to those of the 2-D analysis. For the 3-D geometry, the side wall of the contraction and a symmetry plane perpendicular to the *z*-axis were incorporated. The grid consisted of near-orthogonal, quadrilateral control volumes (CV) with greatest density near the floor of the contraction. The 2-D grid contained similar topology and consisted of 452 CV along the *y*-axis and 1061 CV along the *x*-axis. This equates to a total grid size of 4.8×10^5 CV for 2-D analysis. For 3-D analysis, there are 133 CV along the *y*-axis, 309 CV along the *x*-axis and 106 CV along the *z*-axis. This equates to a total grid size of 4.36×10^6 CV. The CV along the *x* and *y* axes were reduced for the 3-D grid relative to the 2-D grid due to the extensive computational costs for 3-D analysis. All grids were given a first cell height of 1.2×10^{-5} m at the walls. This was chosen to match a minimum y^+ value of less than or equal to 1 for the highest Reynolds number computations [27]. The calculations for y^+ were taken from turbulent, flat-plate, boundary layer theory and are described in Equations 5.1-5.4 [12]. The grid spacing from each wall to its parallel symmetry plane was given a ratio of 1.05, defining the growth rate from one cell height to the next. A contour of y^+ along the side wall of the contraction (blue wall in Figure 5.2) for 3-D computations is provided in Figure 5.3 and a contour of y^+ along the floor of the contraction (green wall in Figure 5.2) for 3-D computations is provided in Figure 5.4. Both contours are with respect to $Re_{Dh} = 4.12\times10^5$ at the inlet of the contraction and the contours consist of no y^+ values greater than 1, matching the desired criterion. The nondimensional wall-normal coordinate within the boundary layer, y^+, is defined as:

$$y^+ = \frac{\rho U_\tau \Delta S}{\mu} \tag{5.1}$$

where ΔS is the wall-normal distance, U_τ is the friction velocity, ρ is the density of the fluid, and μ is the dynamic viscosity of the fluid.

The friction velocity is defined as:

$$U_\tau = \sqrt{\frac{\tau_{wall}}{\rho}} \tag{5.2}$$

where τ_{wall} is the shear stress at the wall. The wall shear can be calculated in Equation 5.3 as,

$$\tau_{wall} = \frac{C_f \rho {U_\infty}^2}{2} \tag{5.3}$$

where C_f is the skin-friction coefficient and U_∞ is the free-stream velocity. The skin friction coefficient can be expressed in Equation 5.4 as,

$$C_f = \frac{0.026}{(Re_{Dh})^{\frac{1}{7}}} \tag{5.4}$$

where Re_{Dh} is the Reynolds number based on the hydraulic diameter.

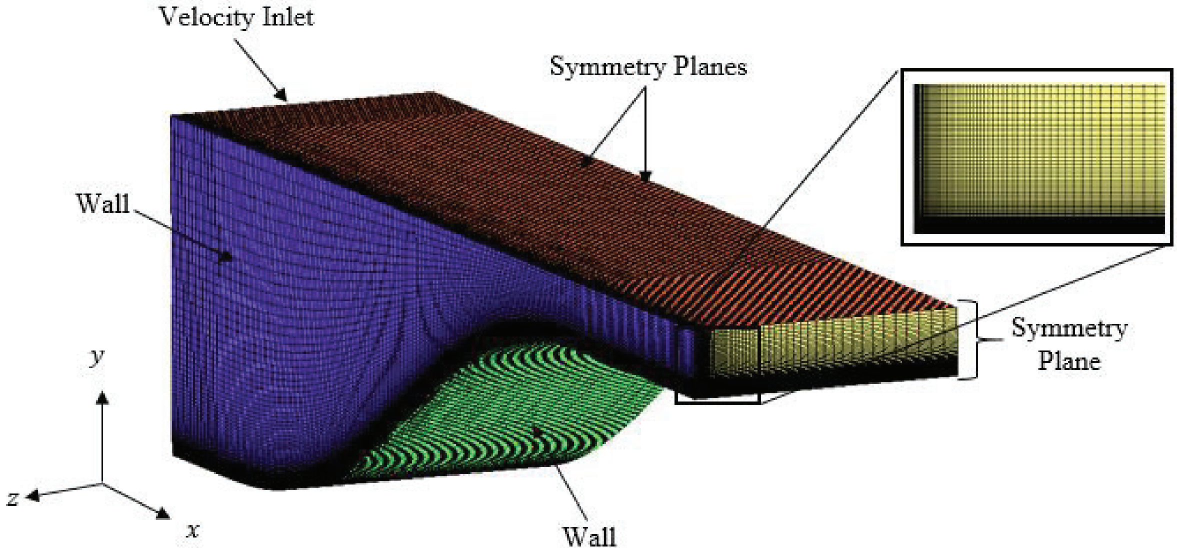

Figure 5.2: 3-D contraction grid with boundary conditions and corner topology.

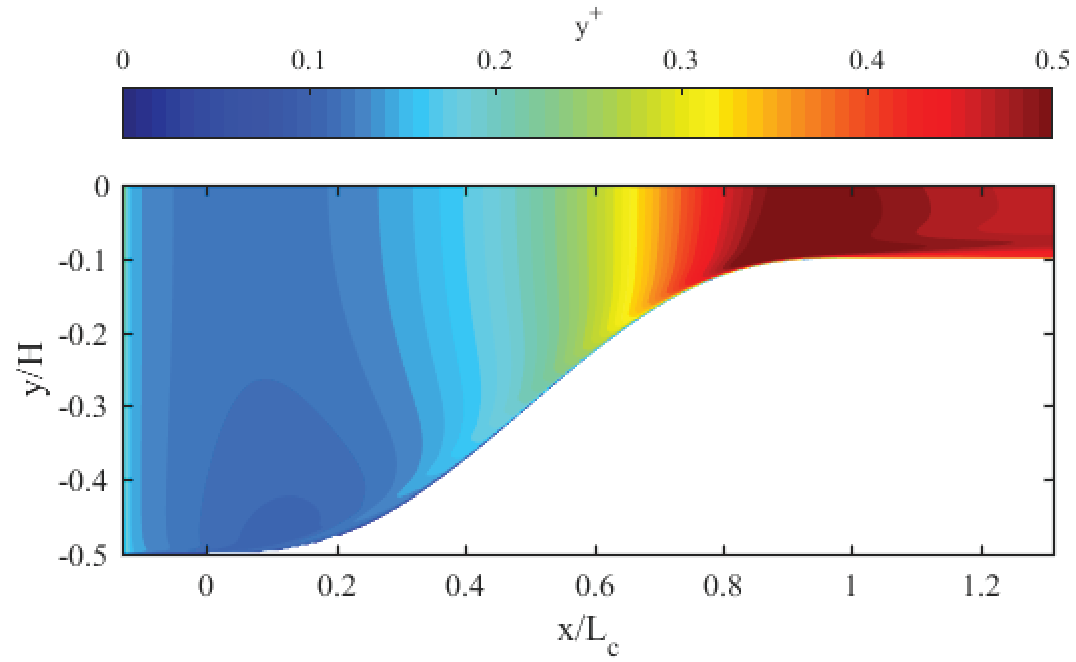

Figure 5.3: y+ along contraction side wall for $Re_{Dh} = 4.12\times10^5$ at contraction inlet.

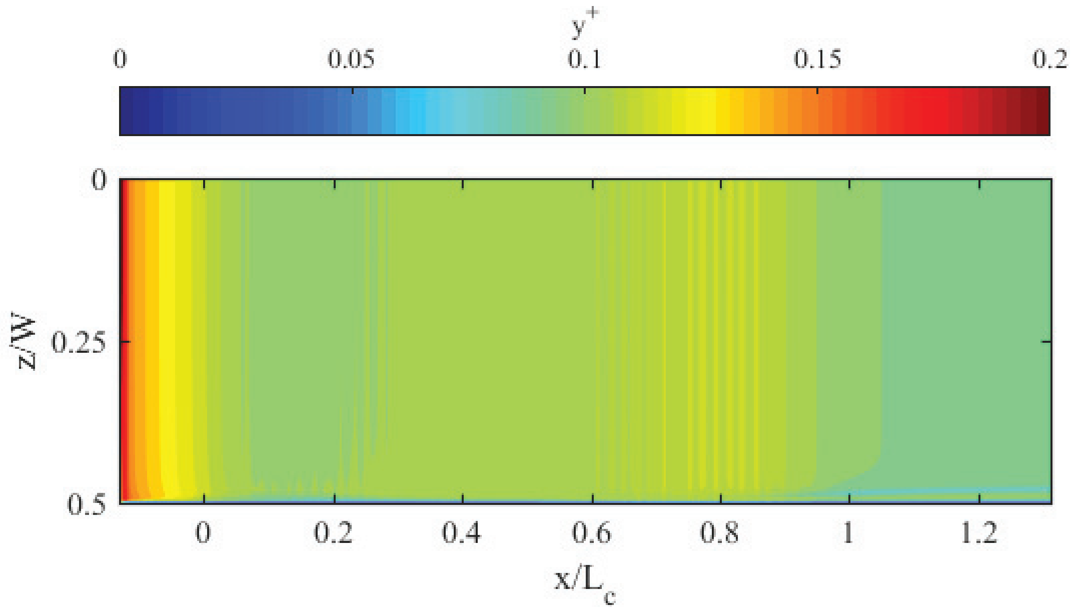

Figure 5.4: y+ along contraction floor for $Re_{Dh} = 4.12\times10^5$ at contraction inlet.

5.1.1 2-D contraction grid convergence

The grid-convergence through the contraction was determined by assessing the development of the boundary-layer (i.e. computing the displacement thickness) along the floor of the contraction for a uniform inflow boundary condition deployed at the inlet. Due to the pressure gradient through the contraction, it was necessary to determine the local edge velocity of the boundary layer in calculating displacement thickness. The streamwise velocity used for calculation of the displacement thickness was resolved into the local wall-tangent direction, which varies with the local curvature of contraction shape. Following the results of Spalart and Watmuff [8], the free-stream velocity at a given location can be defined as,

$$U_\infty = -\int_0^\infty \omega_z(y)dy, \tag{5.5}$$

where ω_z is the vorticity about the z-axis. Using U_∞ to calculate the boundary layer displacement thickness gives,

$$\delta^* = -\frac{1}{U_\infty}\int_0^\infty y\omega_z(y)dy, \tag{5.6}$$

where

$$\omega_z = \frac{\partial v}{\partial x} - \frac{\partial u}{\partial y} \tag{5.7}$$

from the curl of the velocity field. The vorticity was extracted along vectors oriented normal to the floor of the contraction. The vorticity extracted from Fluent in the global Cartesian coordinate system did not require rotation due to invariance of the gradient [28, 29].

The non-dimensional streamwise length along the contraction was plotted against the displacement thickness (δ^*) for all five grids, at all three test-section velocities (7.5, 15, and 30 m/s). The given velocities correspond to Reynolds numbers with the hydraulic diameter as the characteristic length at the inlet of the contraction (Re_{Dh}) of 1.03×10^5, 2.06×10^5, and 4.12×10^5. The results are shown in Figures 5.5-5.7 and correspond to uniform inflow velocity profiles. The total grid CV for each computational grid is given Table 5.1.

Table 5.1: CV specifications for 2-D contraction grid convergence.

Mesh	***x*-axis CV**	***y*-axis CV**	**Total CV**
1	206	88	1.81×10^4
2	372	160	5.95×10^4
3	465	200	9.30×10^4
4	700	301	2.12×10^5
5	1053	452	4.76×10^5

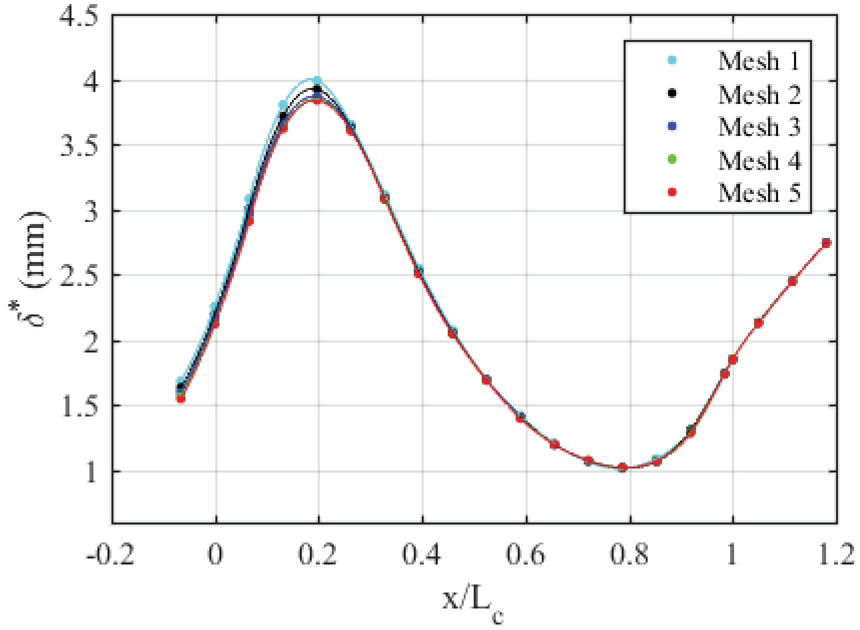

Figure 5.5*:* 2-D grid convergence results for $Re_{Dh} = 1.03\times10^5$ at contraction inlet.

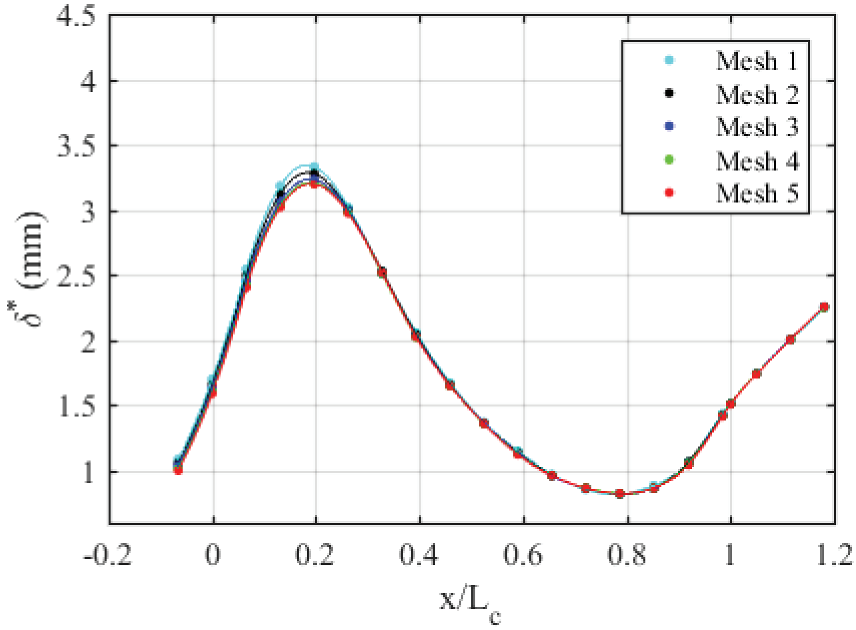

Figure 5.6: 2-D grid convergence results for $Re_{Dh} = 2.06\times10^5$ at contraction inlet.

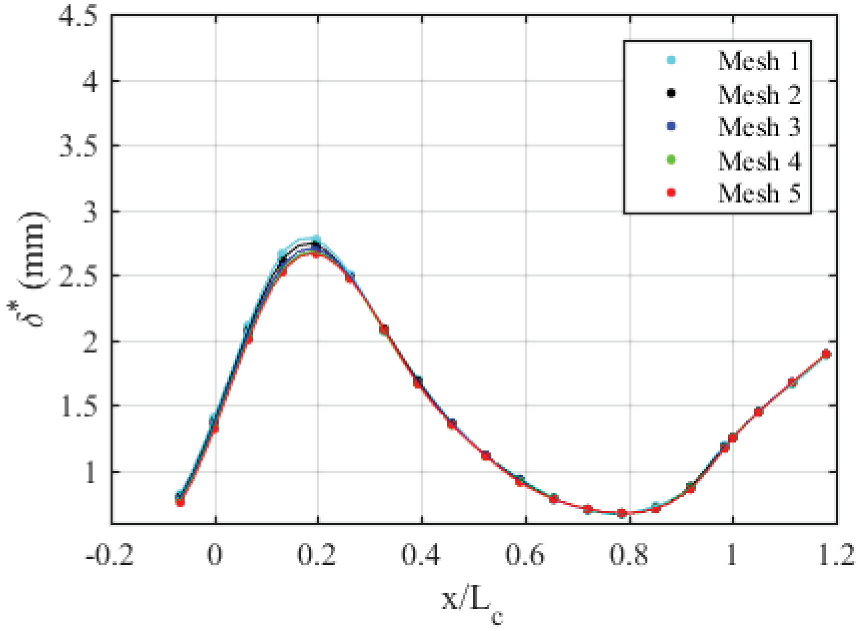

Figure 5.7: 2-D grid convergence results for $Re_{Dh} = 4.12\times10^5$ at contraction inlet.

The maximum percent difference in δ^* between mesh 4 and mesh 5 for all three case was 0.36%, validating the mesh. Mesh 5 was used for all 2-D analysis and was described in Section 5.1, since computational power was readily available.

5.1.2 3-D Contraction Grid Convergence

The 3-D contraction grid was verified using the boundary layer criterion described in Section 5.1.1. The data was analyzed at the intersection of the contraction floor and the centerline symmetry plane. The non-dimensional streamwise length along the contraction was plotted against the displacement thickness (δ^*) for all three grids, at all three test-section velocities. The CV implemented for each grid level is displayed in Table 5.2.

Table 5.2: 3-D contraction CV.

Mesh	***x*-axis CV**	***y*-axis CV**	***z*-axis CV**	**Total CV**
1	136	58	46	3.63×10^5
2	206	88	70	1.27×10^6
3	309	133	106	4.36×10^6

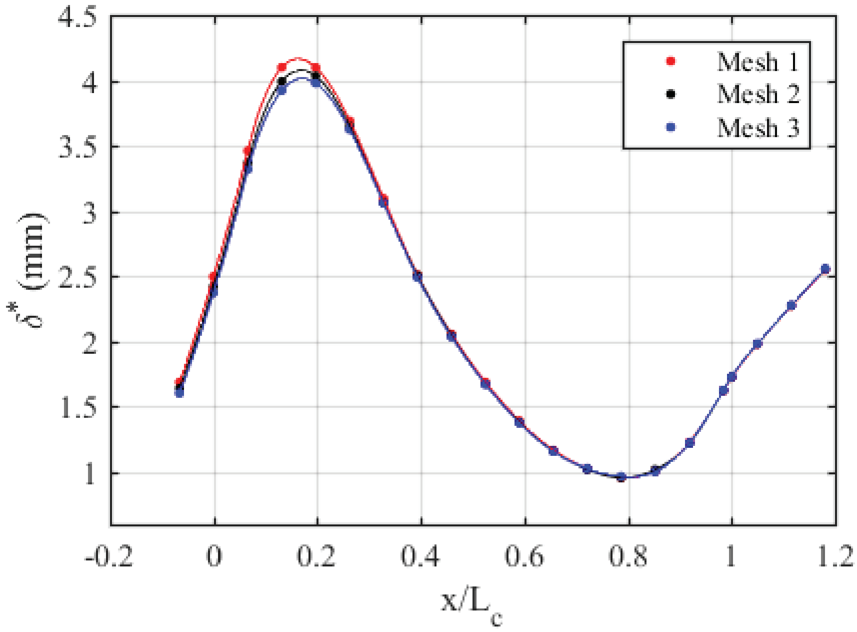

Figure 5.8: 3-D grid convergence Results for $Re_{Dh} = 1.03\times10^5$ at contraction inlet.

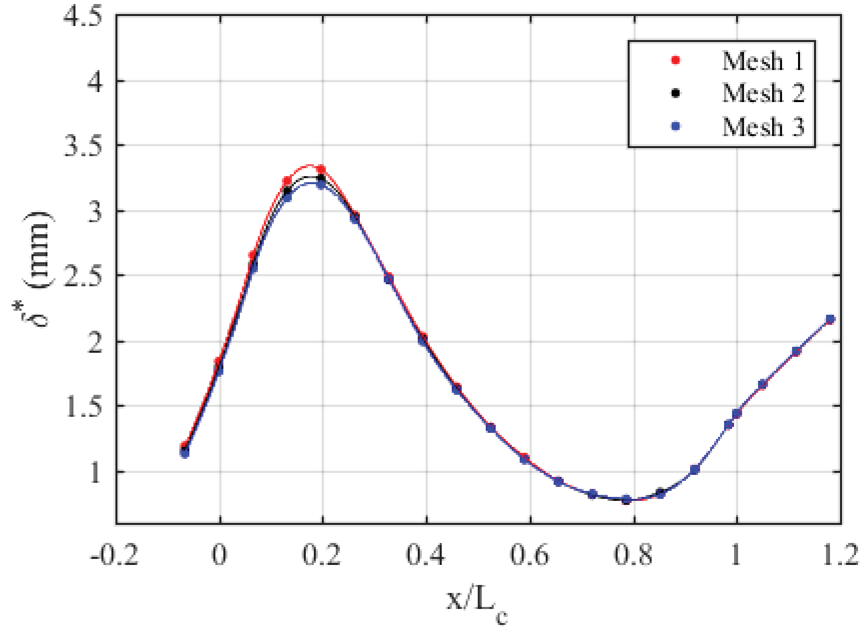

Figure 5.9: 3-D grid convergence results for $Re_{Dh} = 2.06\times10^5$ at contraction inlet.

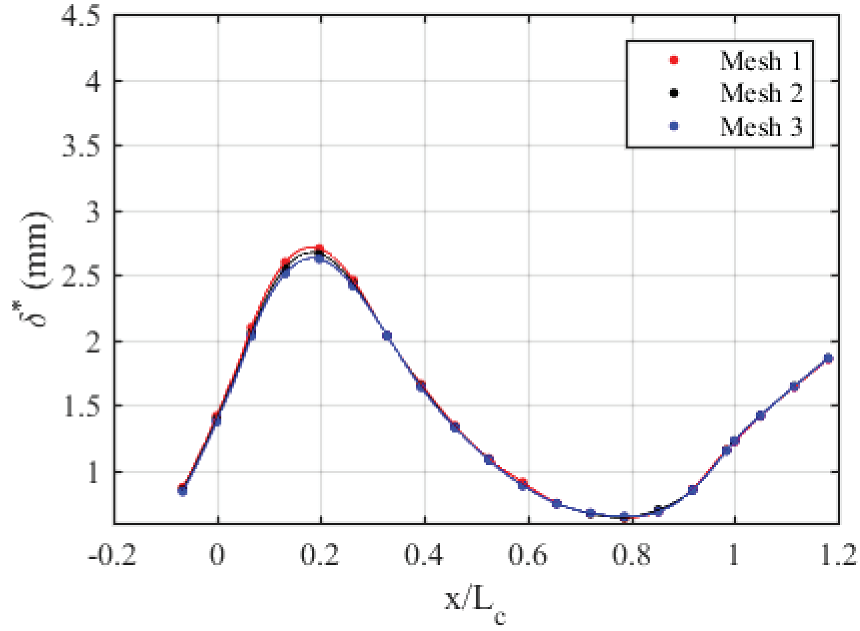

Figure 5.10: 3-D grid convergence results for $Re_{Dh} = 4.12\times10^5$ at contraction inlet.

The greatest difference in δ^* between mesh 2 and mesh 3 for all three 3-D cases was 1.65%, validating the mesh. Mesh 3 was used for all 3-D analysis and is described in Section 5.1.

5.2 2-D Velocity Profile Generation

The flow entering the contraction follows a series of screens, which reduce the thickness of the boundary layers growing along the walls of the tunnel and reorganize the turbulence structure [16]. Exact properties of the flow will be unknown entering the contraction, therefore, various 2-D velocity profiles entering the contraction are considered. The inflow velocity profiles for 2-D analysis were created using a flat place solution. It is known that the k-ω model is quite accurate for the flat-plate boundary layer [30]. The k-ω SST model was selected for a steady analysis in computation of the flat-plate solution. Spacing of the grid points for the flat plate matched the spacing described for the contraction. The entire domain of the grid extended 35.6 m in the *y*-direction and 35 m in the *x*-direction, resulting in a total mesh size of approximately 1.83×10^5. The plate extended a total length of 15 m. A topological depiction of the mesh with the corresponding boundary conditions is shown in Figure 5.11. The figure displays only 25% of the total CV.

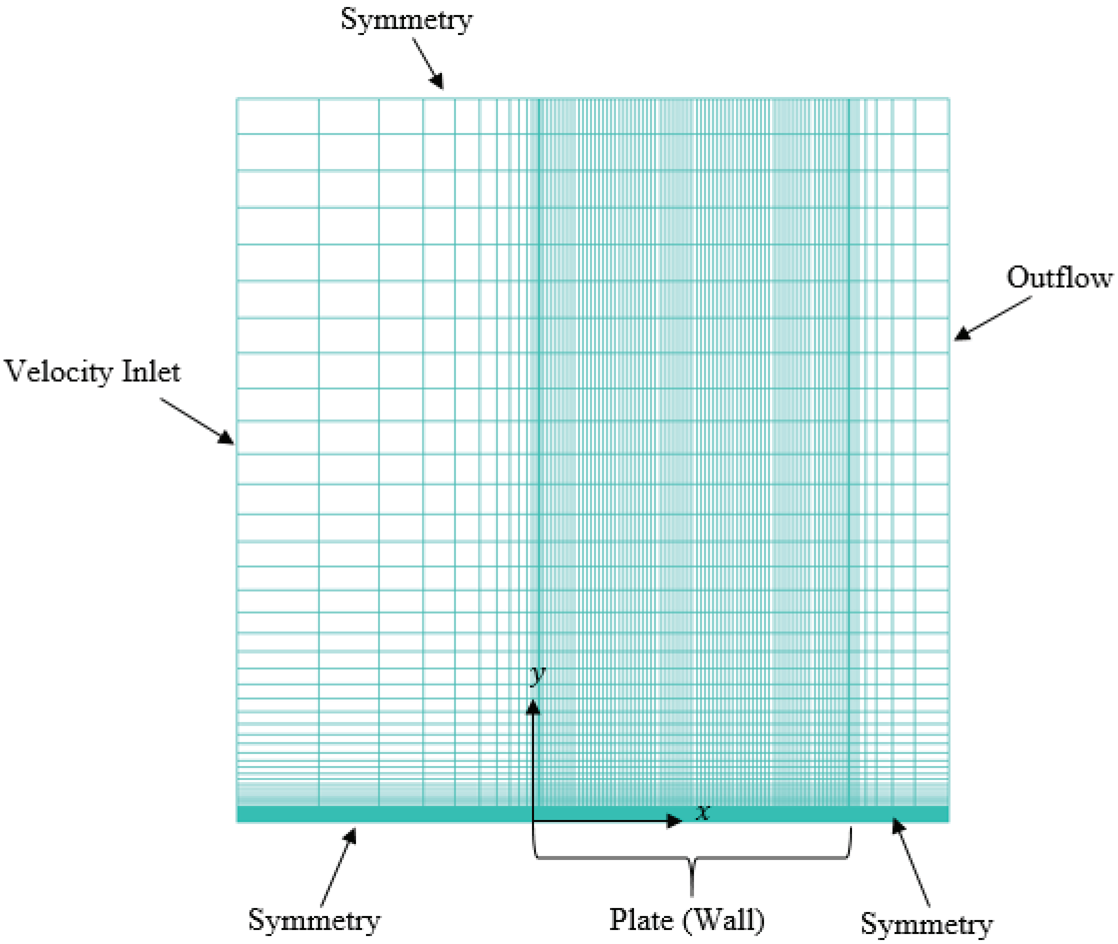

Figure 5.11: 2-D flat plate topological grid structure with 25 % of CV shown.

5.2.1 Flat Plate Mesh Validation

The flat plate solution was verified with flow data generated from other codes using the database available on the NASA Langley Turbulence Modeling Resource (TMR) [31]. A velocity profile was extracted along the plate at x=1.90334 m. The flow had a Mach number (M) of 0.2 and a Reynolds number based on a characteristic length of 1 m (Re_L) of 5×10^6. A comparison between the NASA k-ω SST flat plate results and the results found using the mesh shown in Figure 5.11 are shown in Figure 5.12. The difference in the results are negligible, validating the grid and the solver used for 2-D velocity profile generation.

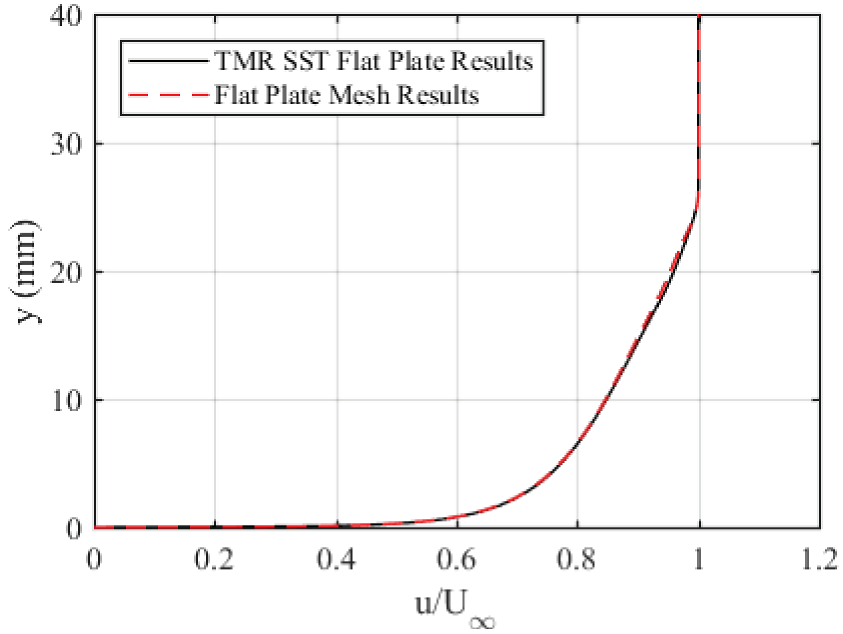

Figure 5.12: 2-D flat plate verification at x = 1.90334 m, Re_L= 5×10^6, and M = 0.2.

5.3 3-D Velocity Profile Generation

Because the turbulence structure will be altered by the screens prior to reaching the contraction [16] and the exact properties of the flow entering the contraction will be unknown, various 3-D velocity profiles will be considered. The inflow velocity profiles for 3-D analysis were created using flow through a rectangular duct, consisting of the same spanwise geometry as the settling chamber of the tunnel. The Reynolds-Stress BSL model was selected for steady analysis in computation of the 3-D flow field solution. The duct extends 6 m in the streamwise direction. Turbulent corner-flow vortices will be generated at the junction of the smooth walls due to the rectangular geometry of the duct [32]. The magnitude of the corner-flow effects entering the contraction will be unknown and determining whether or not the corner-flow will have adverse effects on the core-flow of the tunnel is paramount in characterizing the nature of the tunnel. If the corner-flow effects are small enough to have no effect on the core-flow, the flow can me modeled adequately with 2-D analysis.

The mesh consists of near orthogonal, quadrilateral control volumes (CV) densest near the floor of the duct. The mesh with the corresponding boundary conditions is shown in Figure 5.13. There are 167 CV along the *y*-axis, 133 CV along the *z*-axis, and 125 CV along the *x*-axis. This equates to a total mesh size of 2.78×10^{6} CV. The mesh was given a first cell height of 1.2×10^{-5} m at the walls. The grid spacing from each wall to its parallel symmetry plane was given a ratio of 1.05, defining the growth rate from one cell height to the next, matching the spacing characteristics of the contraction.

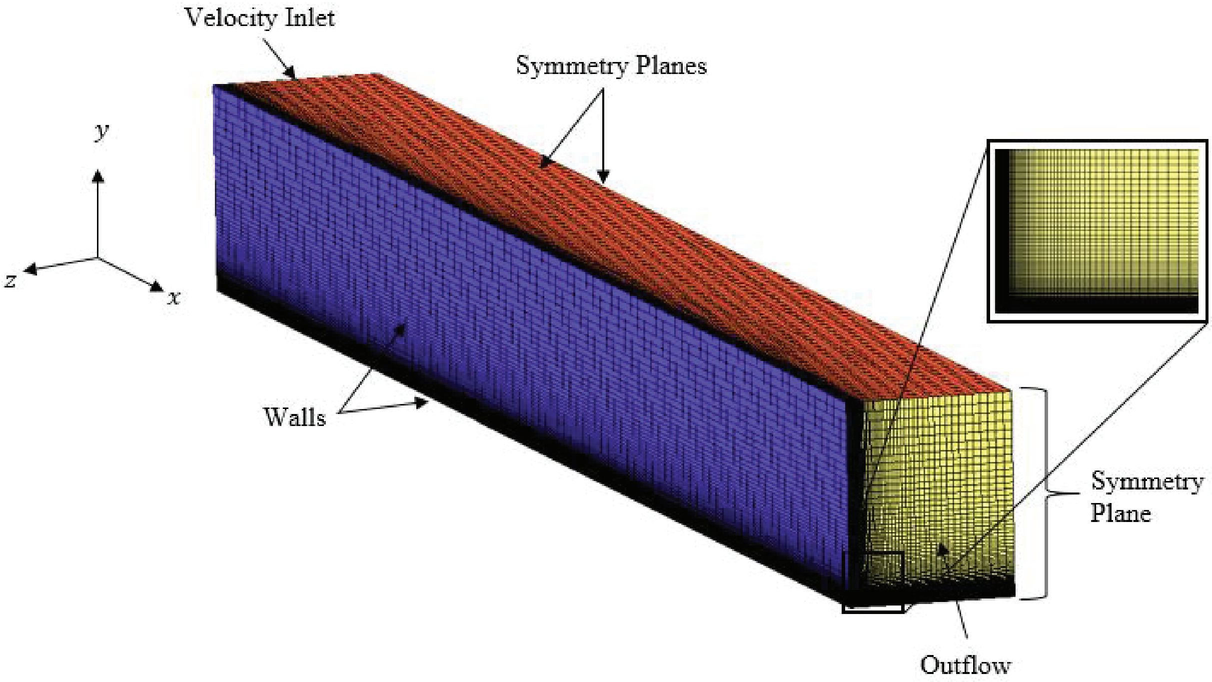

Figure 5.13: 3-D rectangular duct with corner topology.

5.3.1 Rectangular Duct Grid Convergence

Grid convergence was assessed with a criterion of the mean streamwise flow component (U) at an arbitrary point in the core-flow region of the duct. The point corresponded to the coordinate $(x, y, z) = (5 \text{ m}, -0.3 \text{ m}, 0.25 \text{ m})$. This point was chosen because the corner flow will affect the magnitude of the streamwise flow component (u) in the core region of the duct due to the nature of turbulent secondary flows in a rectangular duct [33]. The turbulent stresses acting on the flow, redirect fluid momentum torwards the corner, creating vortices mirrored over the bisector, affecting the streamwise flow components. The results of the grid convergence tests are displayed in Tables 5.4-5.6. The rectangular duct simulations had residual convergence that reached machine zero (1×10^{-15}). Only five decimal places of the solutions are given in Tables 5.4-5.6. The percent difference between each case was negligible, indicating grid convergence. A description of the CV for each grid is shown in Table 5.3.

Table 5.3: Rectangular duct CV.

Mesh	*x*-axis CV	*y*-axis CV	*z*-axis CV	Total CV
1	100	133	106	1.41×10^6
2	125	167	133	2.78×10^6

Table 5.4: Rectangular duct grid convergence for $Re_{Dh} = 1.03\times10^5$ at inlet of duct.

Mesh	U (m/s)	% Difference
1	1.56355	4.73×10^{-2}
2	1.56281	

Table 5.5: Rectangular duct grid convergence for $Re_{Dh} = 2.06\times10^5$ at inlet of duct.

Mesh	U (m/s)	% Difference
1	3.10644	3.70×10^{-2}
2	3.10549	

Table 5.6: Rectangular duct grid convergence for $Re_{Dh} = 4.12\times10^5$ at inlet of duct.

Mesh	**U (m/s)**	**% Difference**
1	6.18077	1.80×10^{-2}
2	6.17966	

Both 2-D and 3-D contraction grids with the corresponding preliminary analyses have been documented. The described numerical setups were implemented for further contraction analysis, and all contraction results are described at length in Chapter 6.

6. CONTRACTION TURBULENCE MODEL RESULTS

Chapter 6 exists to present the results obtained from both 2-D and 3-D contraction analysis, comparing the data where necessary and describing the flow throughout the entire contraction domain. The contraction was assessed using both uniform inflow velocity profiles as well as velocity profiles with a developed boundary layer, used to gauge the sensitivity between the height of the incoming boundary layer with the displacement thickness exiting the contraction. In the case of 3-D analysis, corner-flow properties were assessed to determine whether or not various corner-flow profiles entering the contraction will have adverse effects on the core-flow exiting the contraction (i.e., where future experimentation will occur).

6.1 Uniform Inflow

Figures 6.1-6.3 display the skin friction (C_f) distribution along the floor of the contraction for both cases considered (2-D and 3-D) at all three given contraction inlet Reynolds numbers with a uniform velocity inlet boundary condition. C_f is a ratio between the wall shear stress and the dynamic pressure [12]. This gives:

$$C_f = \frac{\tau_{wall}}{\frac{1}{2}\rho u^2} \tag{6.1}$$

where τ_{wall} is the shear stress at the wall, ρ is the density of the fluid, and u is the streamwise velocity component. Figures 6.4-6.6 display the pressure-coefficient (C_p) along the floor of the contraction. C_p is a ratio between the static pressure of a fluid and the dynamic pressure of a fluid [12]. This gives:

$$C_p = \frac{p - p_\infty}{\frac{1}{2}\rho {U_{TS}}^2} \tag{6.2}$$

where p is the static pressure at a given point along the wall; p_∞ is the freestream static pressure and $\frac{1}{2}\rho U_{TS}^2$ is the dynamic pressure, both referenced at the test section entrance for each velocity considered (7.5, 15, and 30 m/s). Three-dimensional contraction data were analyzed at the intersection of the contraction floor and the centerline symmetry plane. Skin friction data were smoothed using a quadratic regression scheme. Good agreement is shown between the 2-D and 3-D data, suggesting that the centerline flow closely approaches consideration as "2-D," i.e., free of corner-flow influence. The largest differences begin to manifest in the convex region of the contraction, $x/L_c \approx [0.8\text{-}1]$. Boundary-layer separation is not indicated in either domain. C_p data contains negligible difference between the 2-D and 3-D, again indicating that the centerline flow closely approximates 2-D conditions. The degree of two-dimensionality is strongest at the highest Reynolds number tested, indicating the effect of Reynolds number on the development of the sidewall boundary-layers (starting from uniform inflow to the contraction). The Reynolds number effect refers to the fact that at larger Reynolds numbers, the boundary layer is thinner. The sensitivity of the inflow will be assessed in Section 6.2.

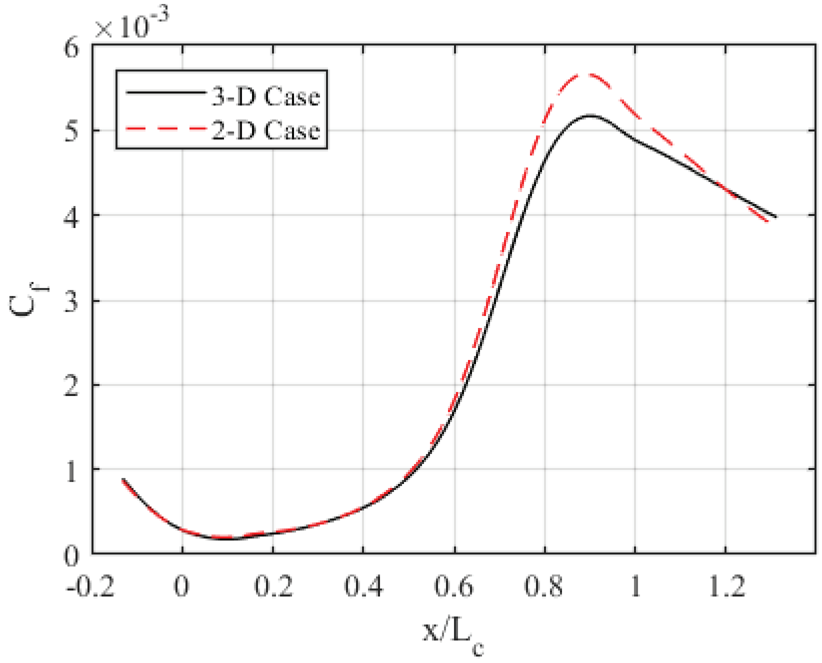

Figure 6.1: Skin-friction distribution along 2-D and 3-D contraction centerline with inflow $Re_{Dh} = 1.03\times10^5$.

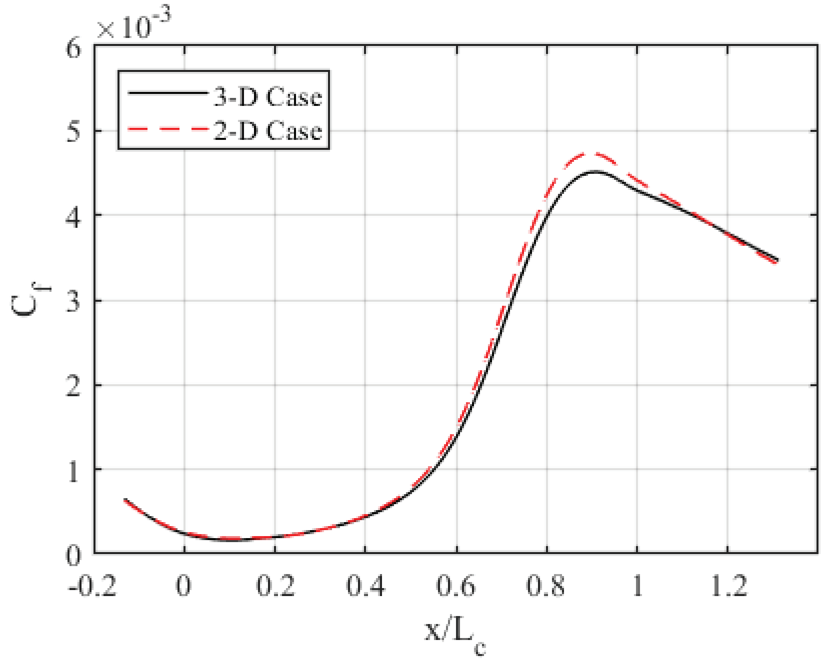

Figure 6.2: Skin-friction distribution along 2-D and 3-D contraction centerline with inflow $Re_{Dh} = 2.06\times10^5$.

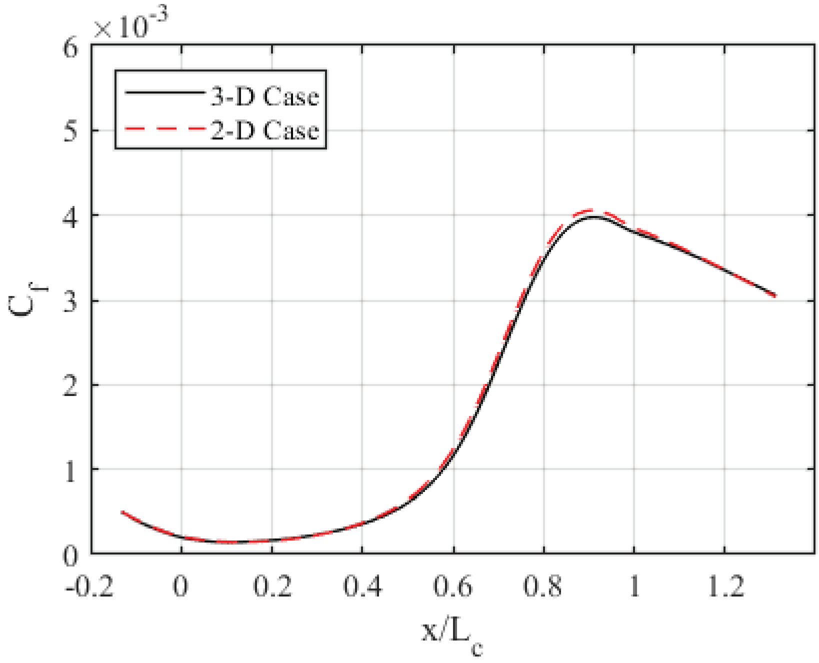

Figure 6.3: Skin-friction distribution along 2-D and 3-D contraction centerline with inflow $Re_{Dh} = 4.12\times10^5$.

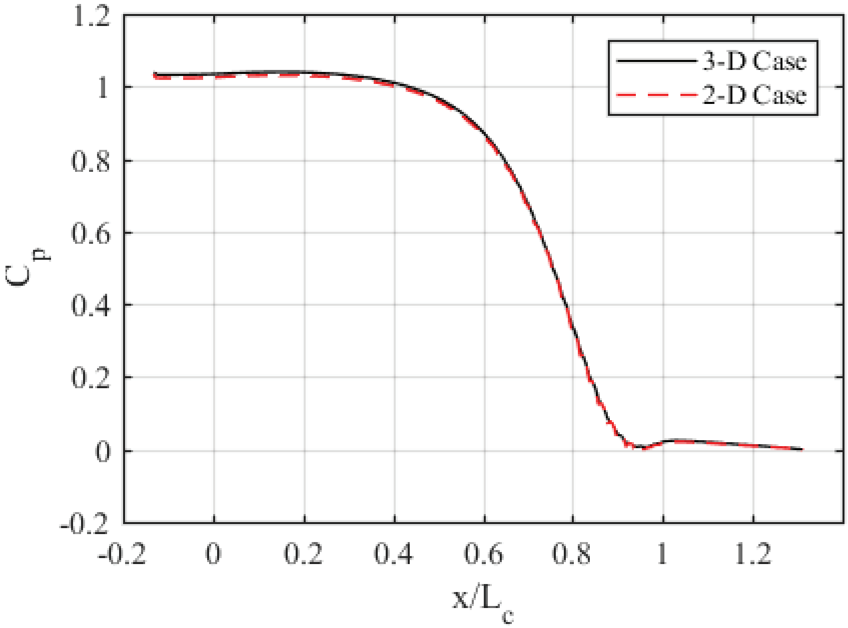

Figure 6.4: Pressure distribution along 2-D and 3-D contraction centerline with inflow $Re_{Dh} = 1.03\times10^5$.

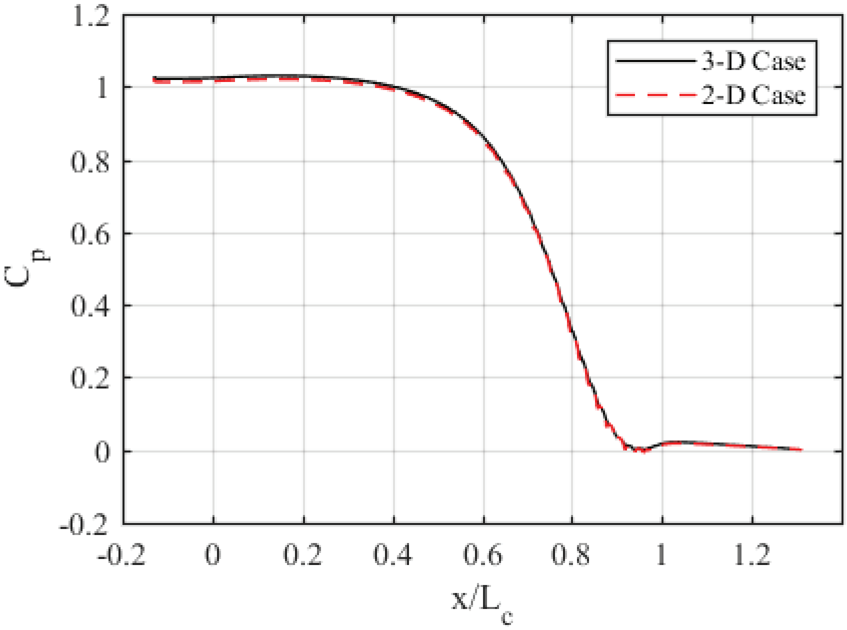

Figure 6.5: Pressure distribution along 2-D and 3-D contraction centerline with inflow $Re_{Dh} = 2.06 \times 10^5$.

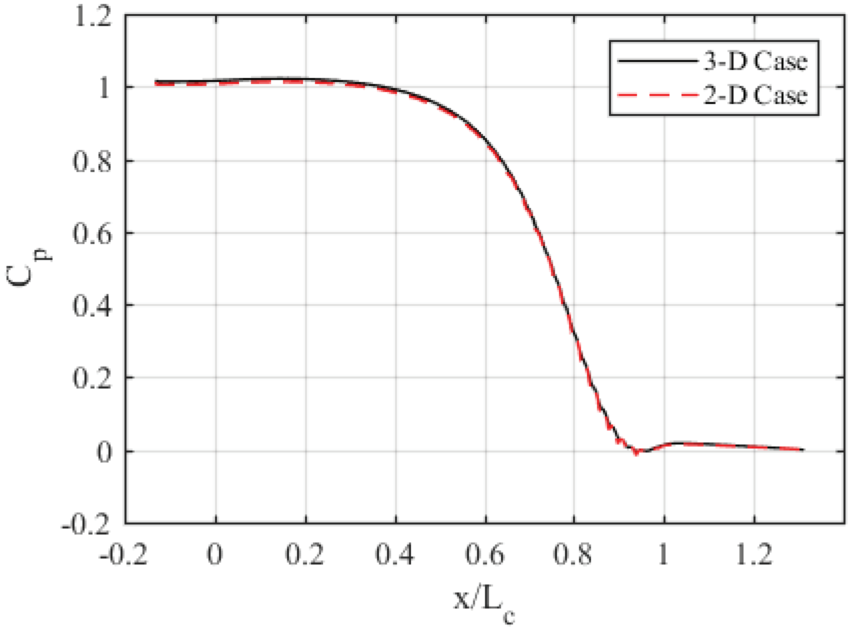

Figure 6.6: Pressure distribution along 2-D and 3-D contraction centerline with inflow $Re_{Dh} = 4.12 \times 10^5$.

The skin-friction distributions along the entire floor of the contraction are shown in Figures 6.7-6.9. The data shows the expected influence of Reynolds number on skin friction due to the presence of the boundary layer. The expected influence is due to larger dynamic pressures in higher Reynolds number flows, and accordingly, the skin friction coefficient will have a smaller magnitude in flows assessed at larger Reynolds numbers. In addition, the contours also display the corner-flow signature in the contraction. The effects are manifested in the outlet region of approximately z/W = [0.47-0.5] for all Reynolds numbers tested. In this region, the development of the boundary layer along the side wall of the contraction is affecting the resulting velocity field at the outlet of the contraction (i.e. the inlet of the test section). From the uniform-velocity inflow analysis, the core flow appears to be unaffected by the corner-flow features at the highest Reynolds number tested.

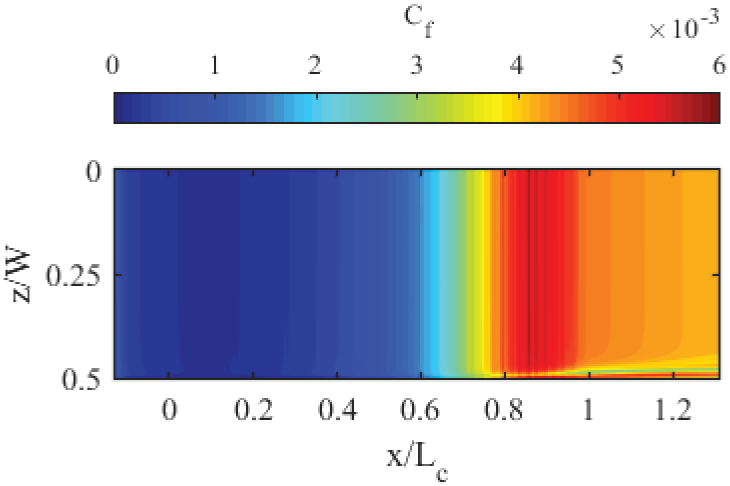

Figure 6.7: Skin-friction along contraction floor for inflow $Re_{Dh} = 1.03\times10^5$.

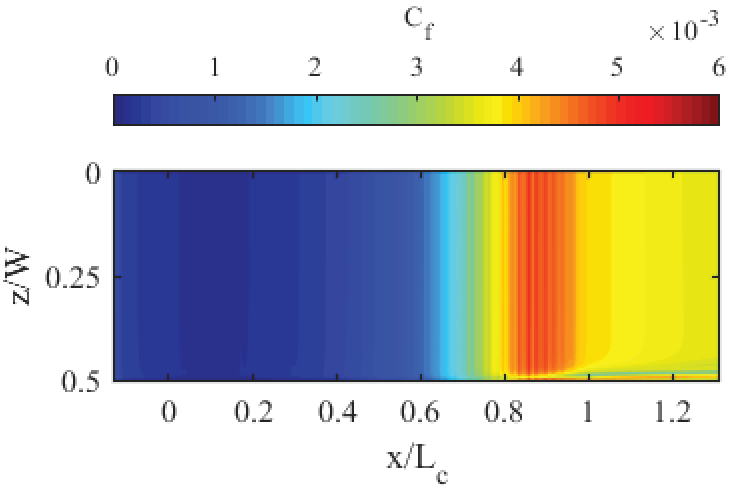

Figure 6.8: Skin-friction along contraction floor for inflow $Re_{Dh} = 2.06 \times 10^5$.

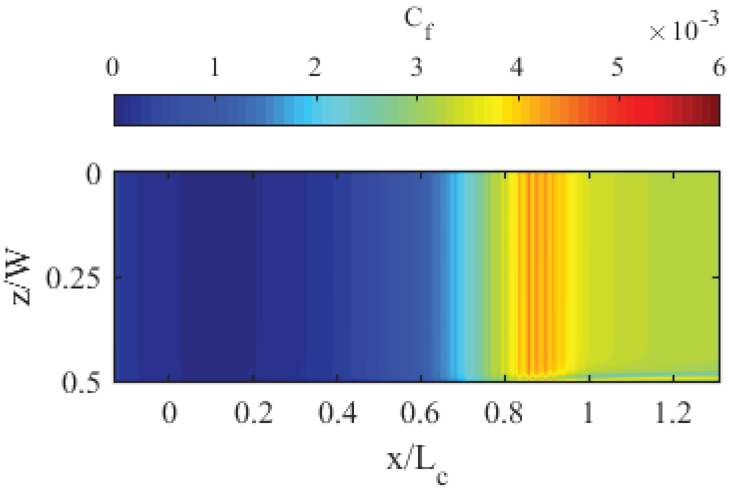

Figure 6.9: Skin-friction along contraction floor for inflow $Re_{Dh} = 4.12 \times 10^5$.

The corner-flow features for the uniform-velocity inflow analysis are shown in greater detail in Figures 6.10-6.12. The cross-sectional velocity and vorticity contours at all Reynolds numbers analyzed reveal two counter-rotating vortices, similar to the results described by Bouriga et al. [34]. According to the numerical analysis, there is a clockwise vortex pushing air away from the wall accompanied by a counterclockwise vortex pushing air towards the wall. The strength of the vorticity is dependent on the Reynolds number of the flow. The velocity profiles were non-dimensionalized with respect to the mean streamwise velocity along the centerline of the wind tunnel (U_{cl}). The computed U_{cl} for each Reynolds number assessed is documented in Table 6.1.

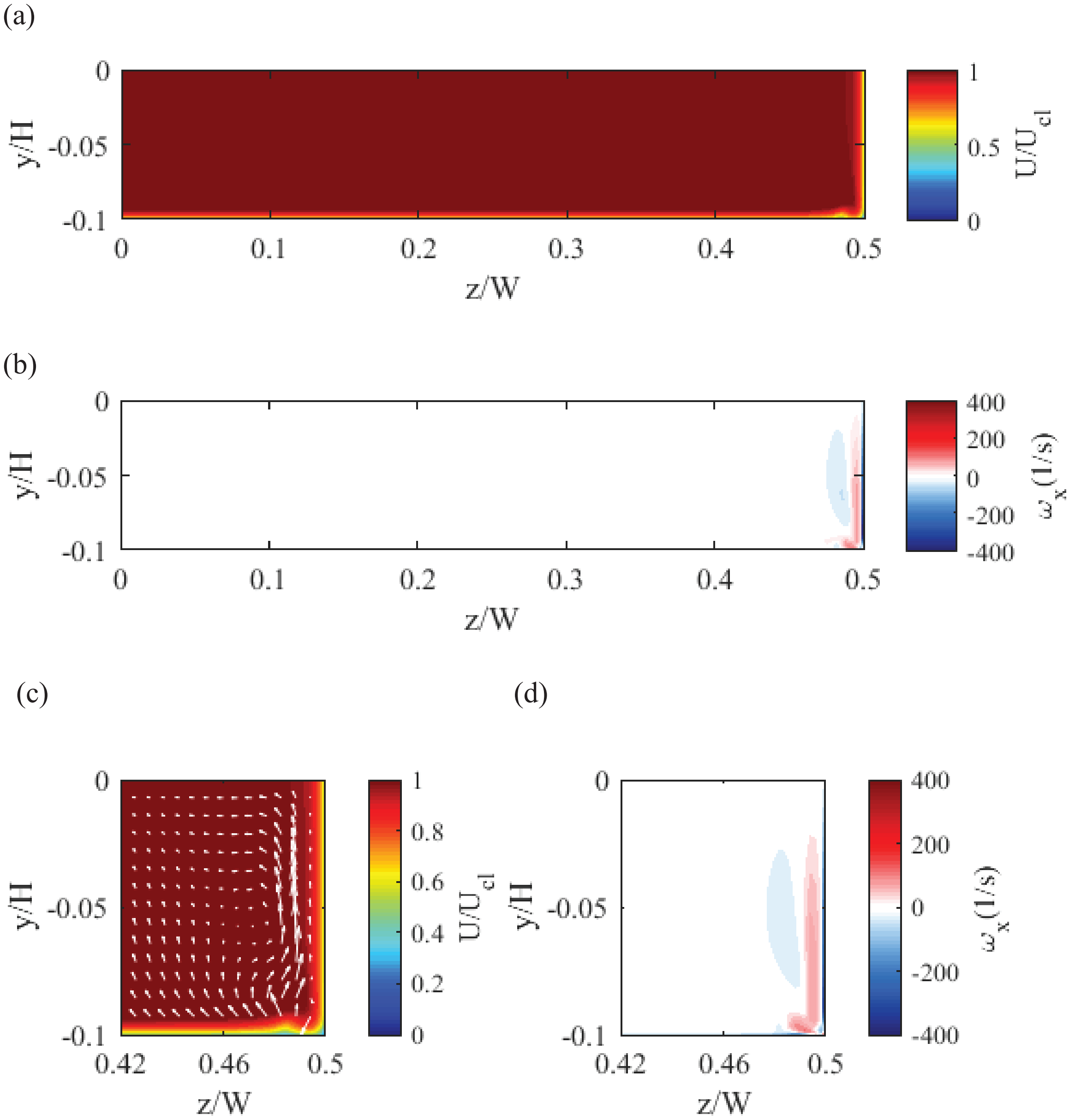

Figure 6.10: Cross-section of contraction outlet with uniform inflow at $Re_{Dh} = 1.03\times10^5$: (a) mean velocity; (b) streamwise vorticity; (c) corner velocity detail; (d) corner vorticity detail.

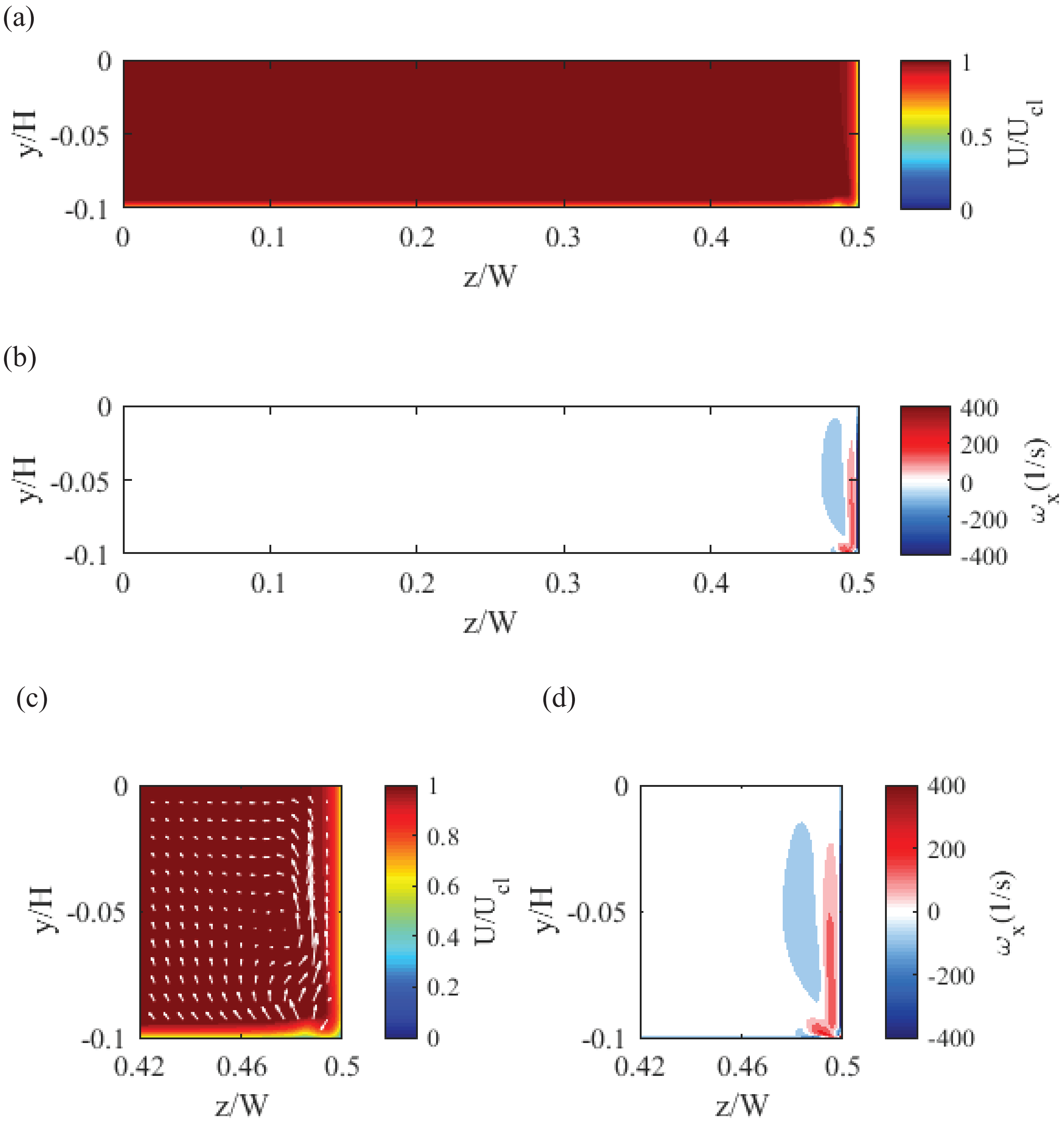

Figure 6.11: Cross-section of contraction outlet with uniform inflow at $Re_{Dh} = 2.06\times10^5$: (a) mean velocity; (b) streamwise vorticity; (c) corner velocity detail; (d) corner vorticity detail.

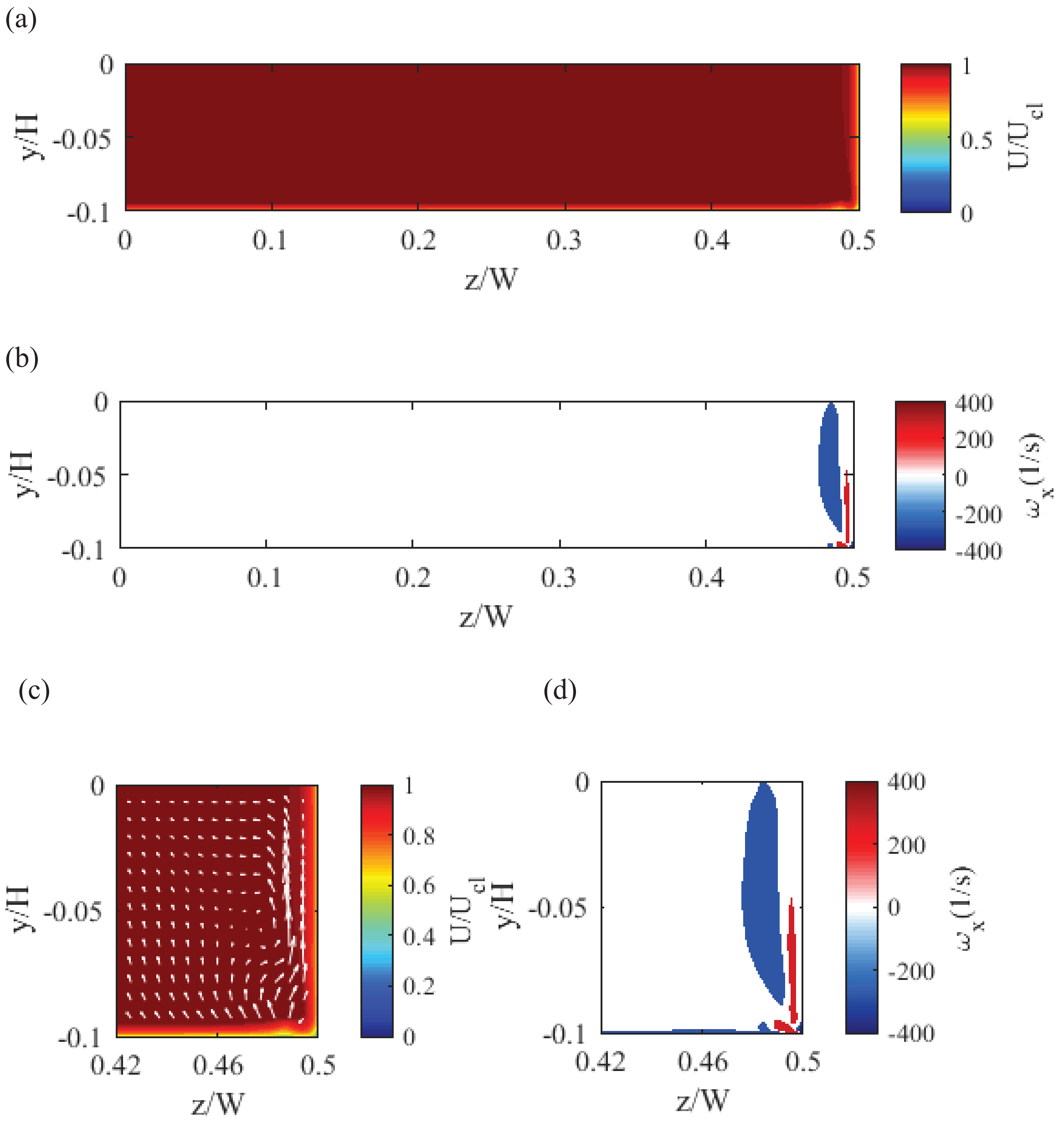

Figure 6.12: Cross-section of contraction outlet with uniform inflow at $Re_{Dh} = 4.12\times10^5$: (a) mean velocity; (b) streamwise vorticity; (c) corner velocity detail; (d) corner vorticity detail.

Table 6.1: U_{cl} for velocity profiles extracted at contraction outlet for a uniform inflow boundary condition.

Re_{Dh}	U_{cl} (m/s)
1.03×10^5	7.608
2.06×10^5	15.17
4.12×10^5	30.27

6.2 2-D Inflow Boundary Layer Effects

Because the exact properties of the flow entering the contraction can be difficult to measure in detail, various velocity inlet profiles were considered. The primary objective of assessing a range of inflow profiles as contraction inlet conditions is to quantify whether they will have adverse effects on the core flow entering the test section. This section outlines the 2-D development of different inlet velocity profiles. The series of inflow velocity profiles for 2-D analysis for are displayed in Figures 6.13-6.15 with corresponding local Reynolds numbers of the flow along the streamwise distance of the flat plate. The profiles were extracted at different distances from the leading edge of the plate. The profiles were non-dimensionalized using edge velocity (U_e), with $U_e = 0.99U_\infty$. An order of magnitude increase in Reynolds number is covered within each data set.

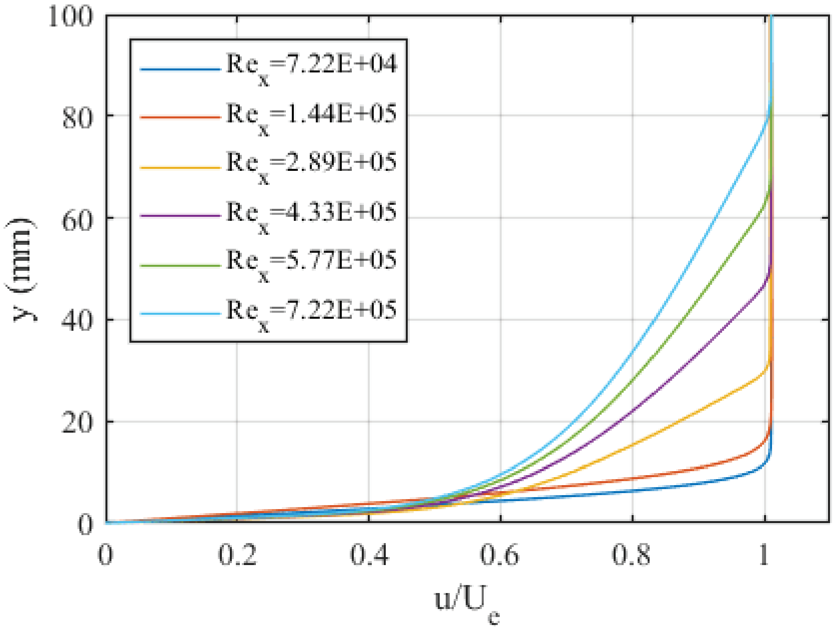

Figure 6.13: Series of 2-D inflow profiles for contraction inlet extracted from flat-plate computations for $U_\infty \approx 1.5$ m/s ($Re_{Dh} = 1.03 \times 10^5$).

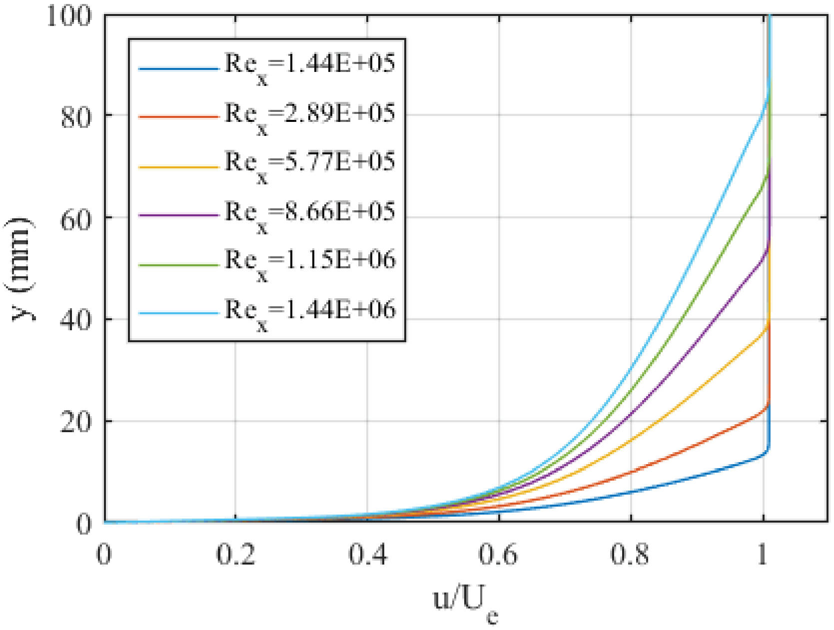

Figure 6.14: Series of 2-D inflow profiles for contraction inlet extracted from flat-plate computations for $U_\infty \approx 3$ m/s ($Re_{Dh} = 2.06 \times 10^5$).

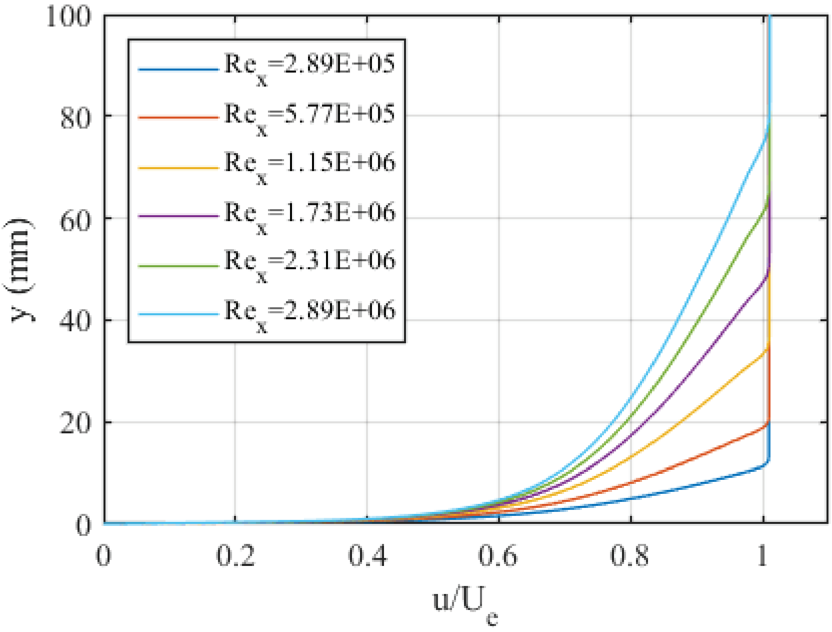

Figure 6.15*:* Series of 2-D inflow profiles for contraction inlet extracted from flat-plate computations for U∞ ≈ 6 m/s ($Re_{Dh} = 4.12\times10^5$).

Figures 6.16-6.18 display the evolution of displacement thickness along the contraction for a series of inflow profiles, including the uniform inflow condition for all specified Reynolds numbers at the inlet of the contraction. The *x*-axis gives the non-dimensional streamwise distance along the contraction and corresponds to the geometry described in Figure 5.1. The axis goes below zero because the model geometry does not start exactly at the inlet of the contraction and goes beyond one because the model accounts for some of the test section geometry. It can be concluded from the 2-D analysis that the properties of the boundary-layer, specifically the size of the displacement thickness entering the contraction, appear to have negligible influence on the resulting displacement thickness exiting the contraction. This is in agreement with previous calculations by Pook and Watmuff [20]. The results suggest that the velocity profile entering the contraction will be relatively insensitive to the velocity profile exiting the contraction, as the displacement thickness assesses the blockage caused by the boundary layer and has little variation at the contraction outlet for all assessed inflow profiles. The specifics of the resulting contraction outlet velocity profiles are assessed in greater detail for 3-D computations. This insensitivity of the contraction inflow should be viewed favorably for the qualification of the tunnel as a validation-grade facility.

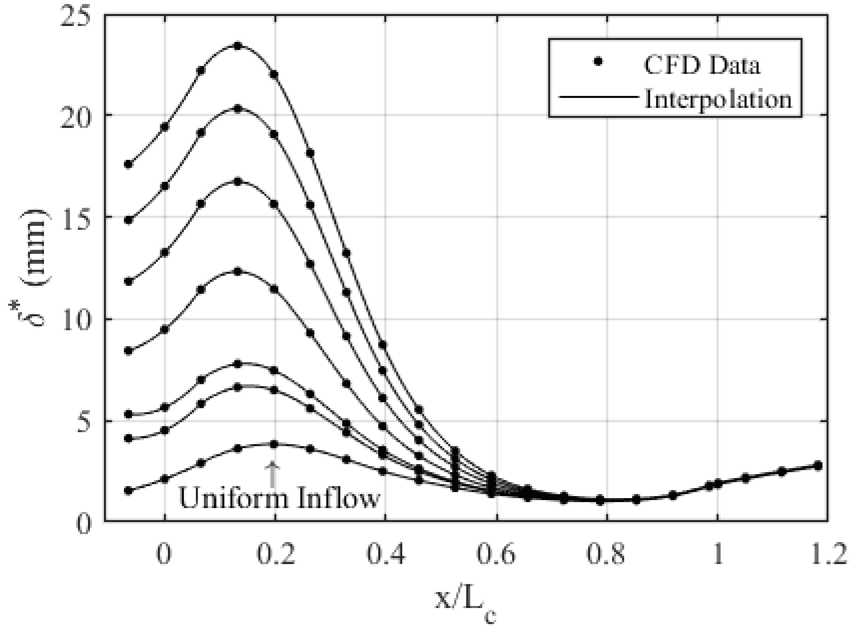

Figure 6.16: 2-D effect of δ^* entering contraction on mean outflow for $Re_{Dh} = 1.03\times10^5$ at contraction inlet.

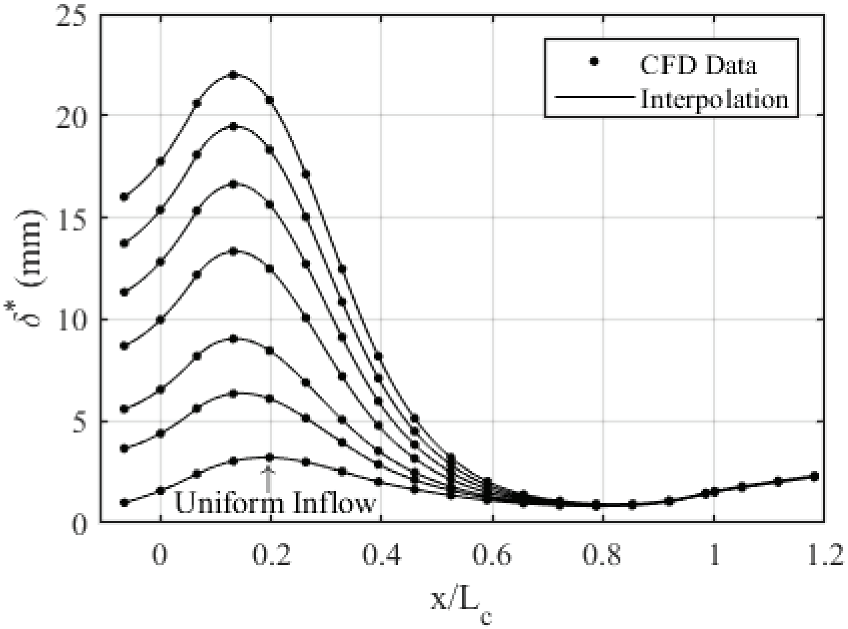

Figure 6.17: 2-D effect of δ^* entering contraction on mean outflow for $Re_{Dh} = 2.06\times10^5$ at contraction inlet.

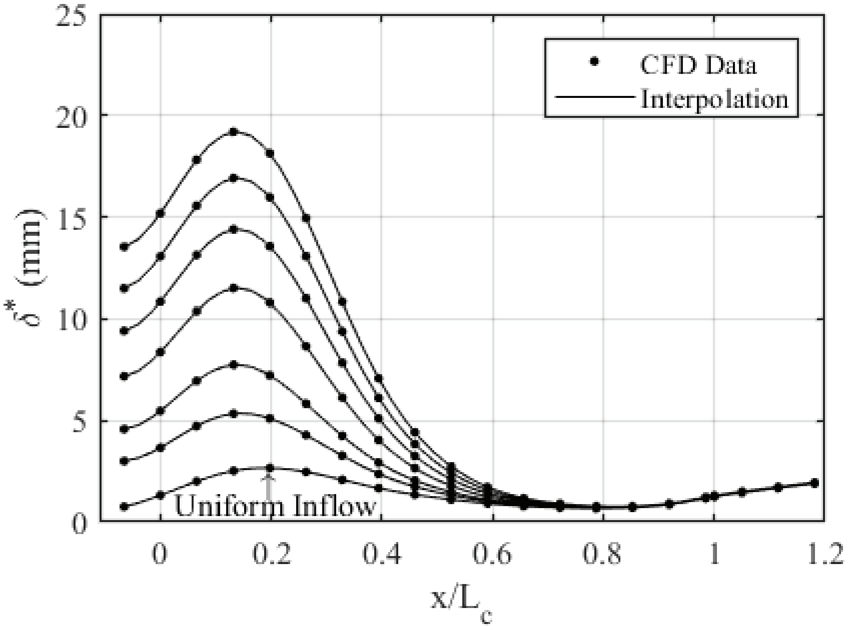

Figure 6.18: 2-D effect of δ^* entering contraction on mean outflow for $Re_{Dh} = 4.12\times10^5$ at contraction inlet.

Table 6.2 gives the average δ^* at the outlet of the contraction for each Re_{Dh} at the contraction inlet for 2-D computations. The height of the displacement thickness entering the test section varies with the Reynolds number of the flow. In particular, higher Reynolds number flows produce thinner boundary layers within the envelope of flow speeds presented, aligning with anticipated results.

Table 6.2: Average δ^* exiting contraction based on inflow Re_{Dh} for 2-D computations.

Re_{Dh}	δ^* (mm)
1.03×10^5	1.88
2.06×10^5	1.54
4.12×10^5	1.27

6.3 3-D Inflow Velocity Profile Effects

Figures 6.19-6.21 display the velocity and vorticity profiles extracted from the rectangular duct shown in Figure 5.13 at a streamwise length of 5 m for all three Reynolds numbers based on the hydraulic diameter (Re_{Dh}) at the inlet of the contraction (1.03×10^5, 2.06×10^5, and 4.12×10^5). These figures were chosen for display because they correspond to the profiles with the largest corner-flow effects, and hence the strongest influence on the uniformity of the flow exiting the contraction. These profiles were used as boundary-conditions at the inlet of the contraction and correspond to the contraction outlet profiles displayed in Figures 6.22-6.24 The velocity profiles were non-dimensionalized with respect to the streamwise center-line velocity (U_{cl}) . The center-line velocity corresponds to the streamwise velocity at the center of the duct, or $(z/\mathrm{W}, y/\mathrm{H}) = (0,0)$ in Figures 6.19-6.21. All centerline velocities at different Reynolds numbers are given in Table 6.3. The profiles align well with expected results for turbulent secondary flows in a rectangular duct [33], where the turbulent stresses redirect fluid momentum toward the corner along its bisector, creating vortices mirrored over the corner of the duct.

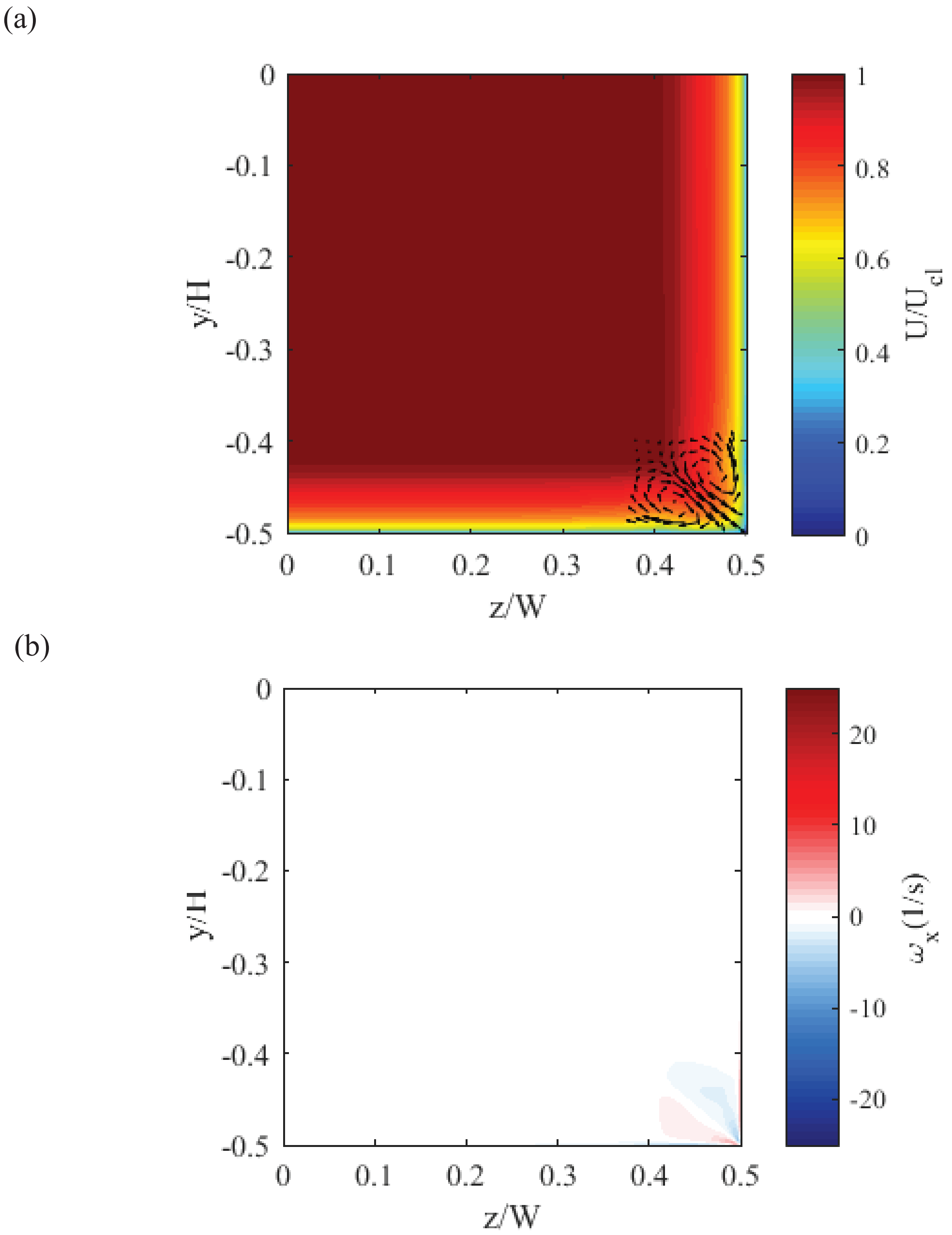

Figure 6.19: Flow cross-section extracted at $x/L_{Duct} = 0.834$ for inflow $Re_{Dh} = 1.03\times10^5$: (a) velocity contours with corner flow detail; (b) streamwise vorticity contours.

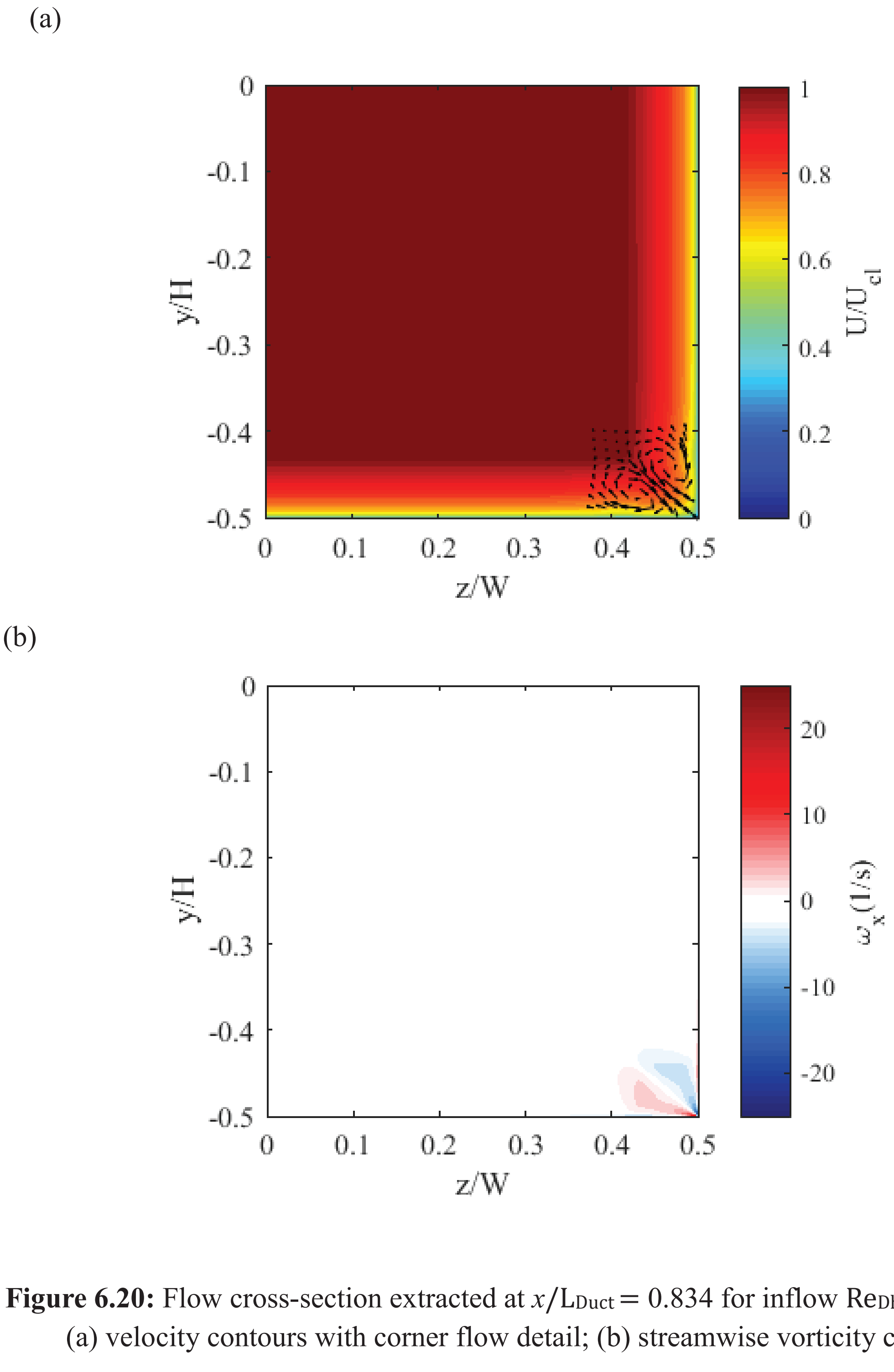

Figure 6.20: Flow cross-section extracted at $x/L_{Duct} = 0.834$ for inflow $Re_{Dh} = 2.06\times10^5$: (a) velocity contours with corner flow detail; (b) streamwise vorticity contours.

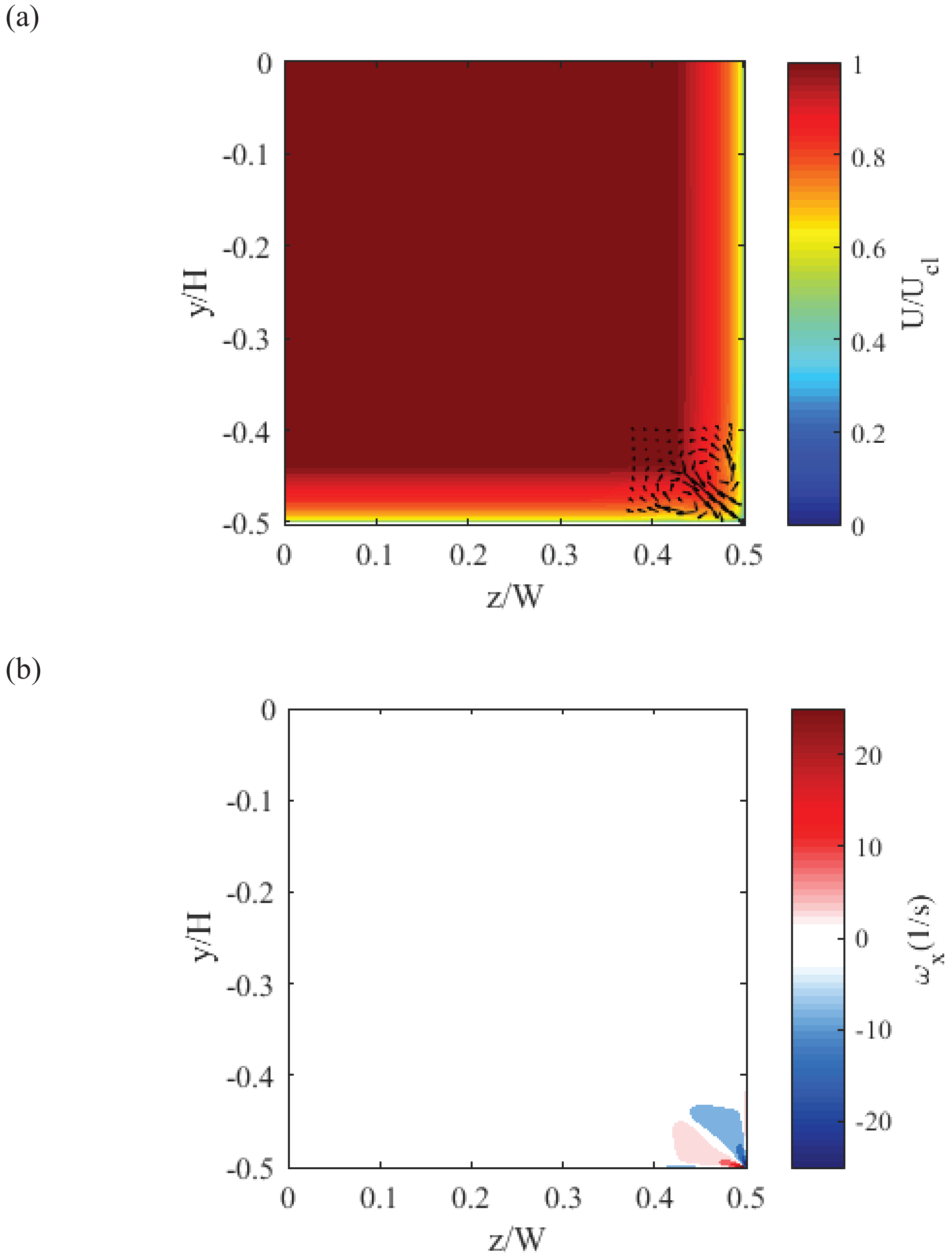

Figure 6.21: Flow cross-section extracted at $x/L_{Duct} = 0.834$ for inflow $Re_{Dh} = 4.12\times10^5$: (a) velocity contours with corner flow detail; (b) streamwise vorticity contours.

Table 6.3: U_{cl} from velocity profiles extracted at $x/L_{Duct} = 0.834$ along duct.

Re_{Dh}	U_{cl} (m/s)
1.03×10^5	1.589
2.06×10^5	3.151
4.12×10^5	6.261

Figures 6.22-6.24 display the velocity and vorticity contours at the outlet of the contraction corresponding to the velocity and vorticity profiles (used as inlet boundary conditions) shown in Figures 6.19-6.21. The results indicate that the core flow remains unaffected by the corner-flow features imposed at the inlet of the contraction. Therefore, the flow exiting the contraction appears to have minimal sensitivity to the 3-D inflow. The velocity profiles at the contraction outlet were non-dimensionalized with respect to the streamwise centerline velocity (U_{cl}) at the outlet of the contraction. U_{cl} was extracted at $(z/W, y/H) = (0,0)$ in Figures 6.22-6.24. All centerline velocities calculated at the contraction outlet, corresponding to the series of Reynolds numbers considered, are given in Table 6.4.

Table 6.4: U_{cl} from velocity profiles extracted at contraction outlet with velocity profile along duct at $x/L_{Duct} = 0.834$ used as contraction inlet boundary condition.

Re_{Dh}	U_{cl} (m/s)
1.03×10^5	7.621
2.06×10^5	15.19
4.12×10^5	30.31

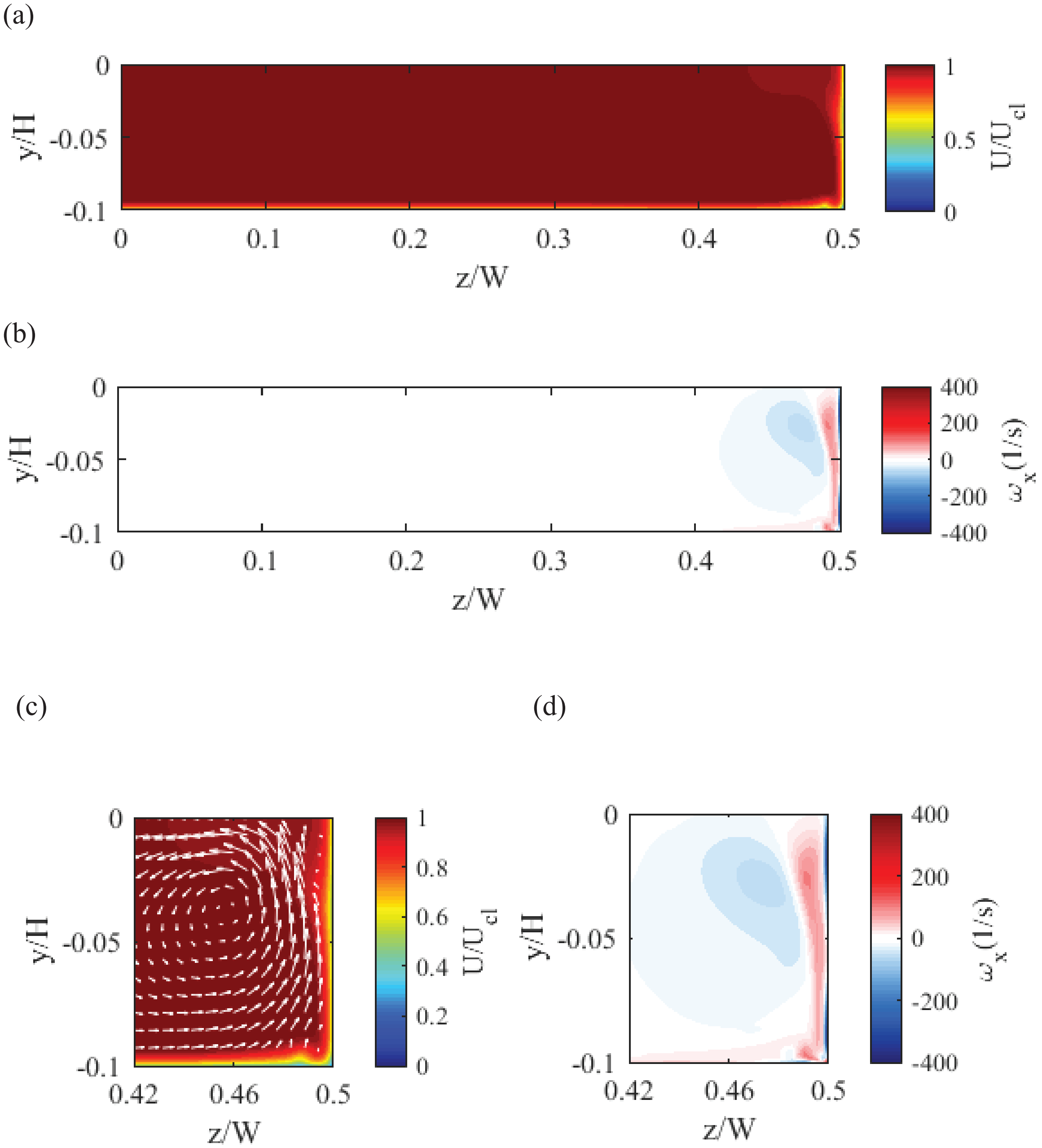

Figure 6.22: Cross-section from extracted inflow case at $Re_{Dh} = 1.03\times10^5$: (a) mean velocity; (b) streamwise vorticity; (c) corner velocity detail; (d) corner vorticity detail.

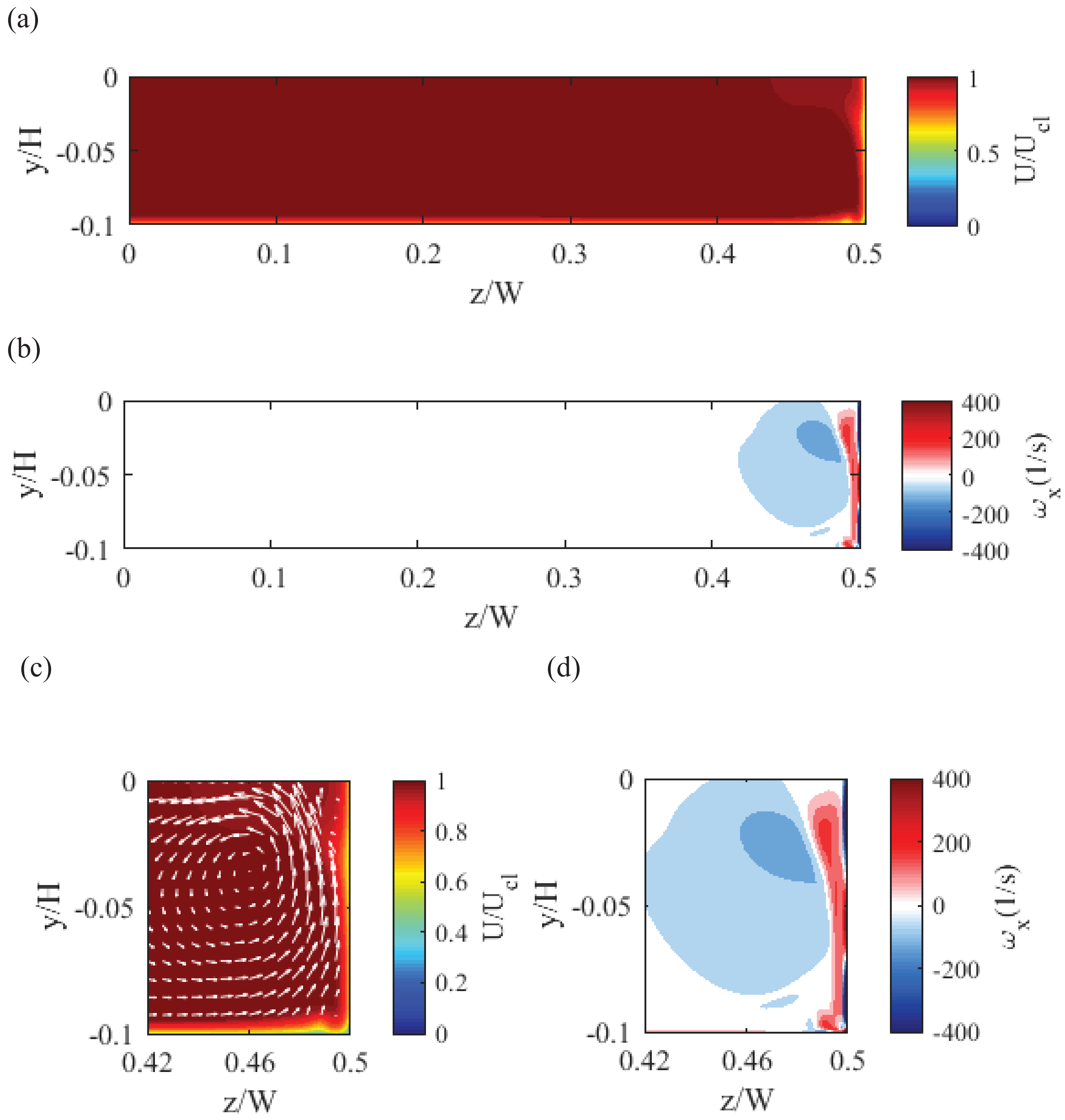

Figure 6.23: Cross-section from extracted inflow case at $Re_{Dh} = 2.06\times10^5$: (a) mean velocity; (b) streamwise vorticity; (c) corner velocity detail; (d) corner vorticity detail.

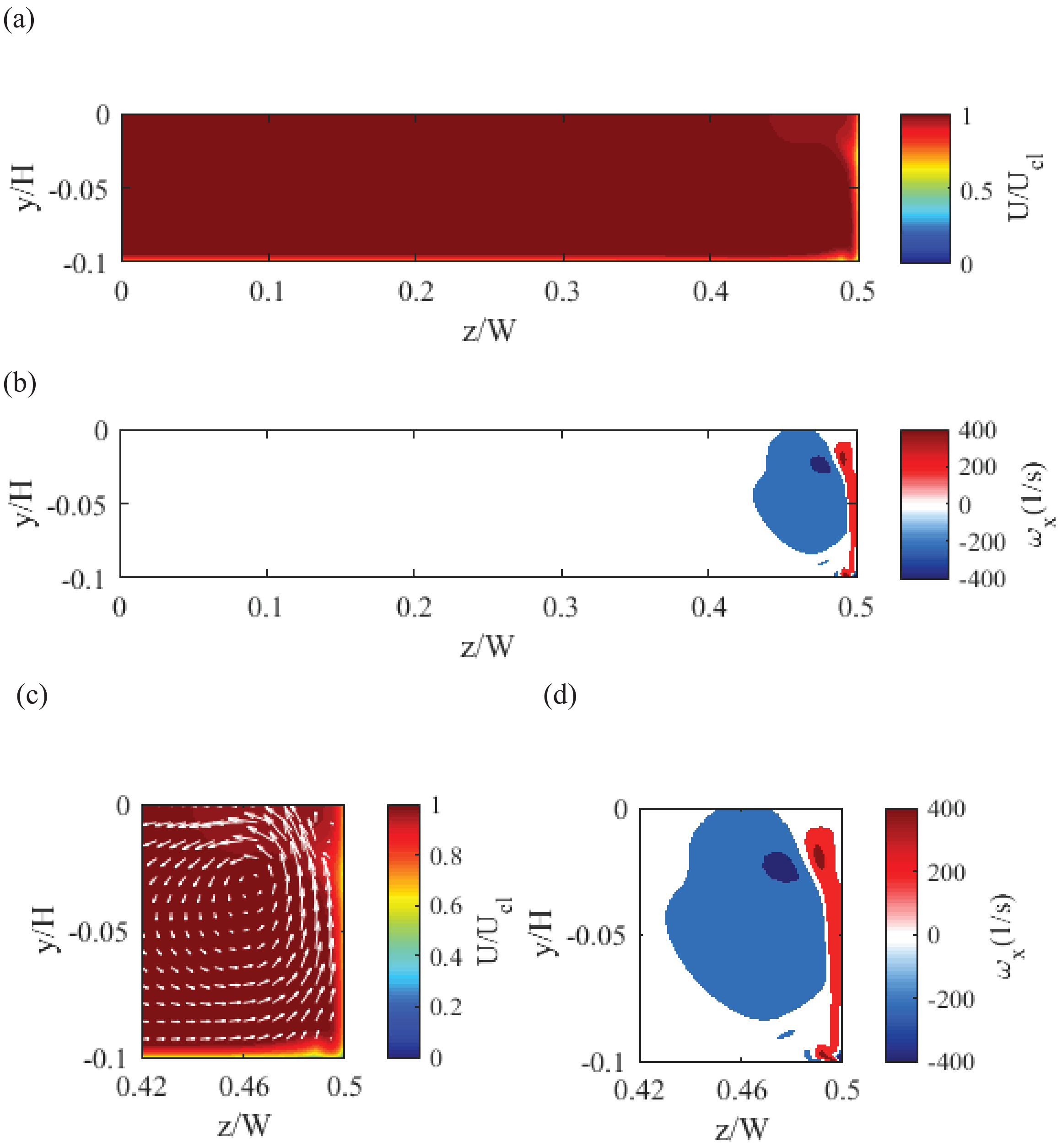

Figure 6.24: Cross-section from extracted inflow case at $Re_{Dh} = 4.12\times10^5$: (a) mean velocity; (b) streamwise vorticity; (c) corner velocity detail; (d) corner vorticity detail.

6.4 3-D Inflow Boundary-Layer Effects

Three-dimensional contraction displacement thickness data were analyzed along the center of the contraction geometry, at the intersection of the contraction floor and the centerline symmetry plane. This was motivated by the fact that future experimental measurements will take place nominally along the centerline of the test section. The boundary layer development through the center of the contraction is shown in Figures 6.25-6.27, and consists of a similar trend shown in Figures 6.16-6.18 for the 2-D contraction analysis. Similar to the 2-D analysis, it can be concluded from the 3-D analysis that the boundary layer (characterized by it's the displacement thickness) entering the contraction appears to have negligible influence on the resulting displacement thickness exiting the contraction, again confirming the calculations by Pook and Watmuff [20]. It can also be concluded that for computations involving the boundary layer development in the contraction, at the largest Reynolds numbers assessed ($Re_{Dh} = 4.12\times10^5$ at the contraction inlet), 2-D analysis should suffice. At the lower Reynolds number assessed ($Re_{Dh} = 1.03\times10^5$ at the contraction inlet), it is unclear which type of analysis is more accurate as there is a 6.59 percent difference between δ^* entering the contraction between 2-D and 3-D computations. Future experimental analysis will play a crucial role in developing a better understanding of the flow properties through the tunnel. Table 6.5 gives the average displacement thickness from all inflow velocity profiles considered, calculated at the outlet of the contraction. The results are comparable with the 2-D displacement thickness analysis presented in Figures 6.16-6.18. Percent differences between the 2-D and 3-D computations are presented in Table 6.6. The largest differences between 2-D and 3-D computations are manifested at the lowest Reynolds numbers, where the thickness of the boundary-layer is the largest.

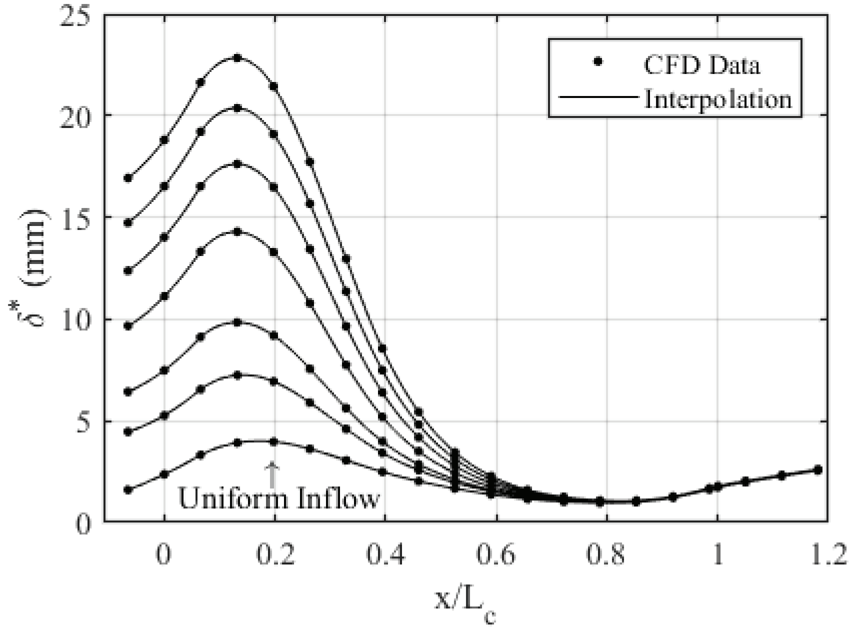

Figure 6.25: 3-D effect of δ^* entering contraction on mean outflow for $Re_{Dh} = 1.03\times10^5$ at contraction inlet.

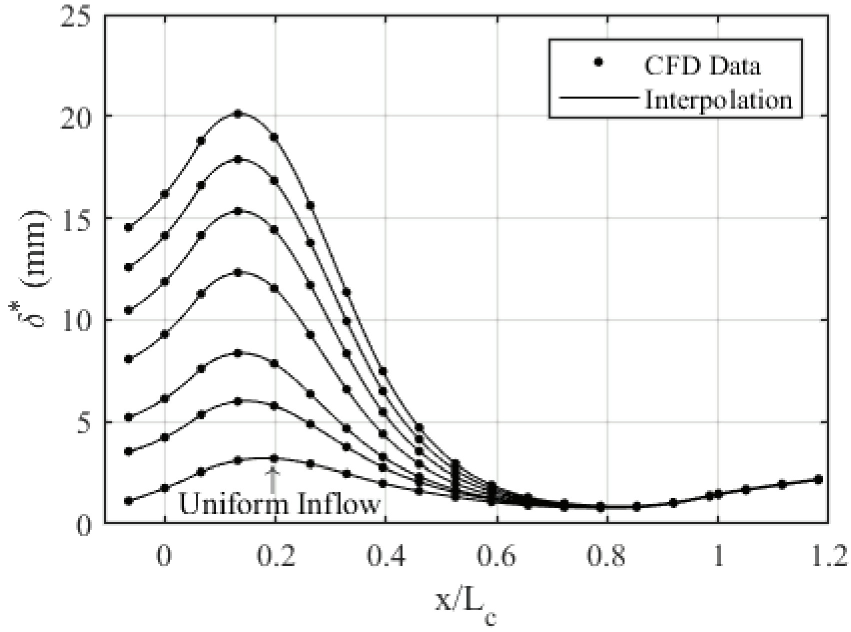

Figure 6.26: 3-D effect of δ^* entering contraction on mean outflow for $Re_{Dh} = 2.06\times10^5$ at contraction inlet.

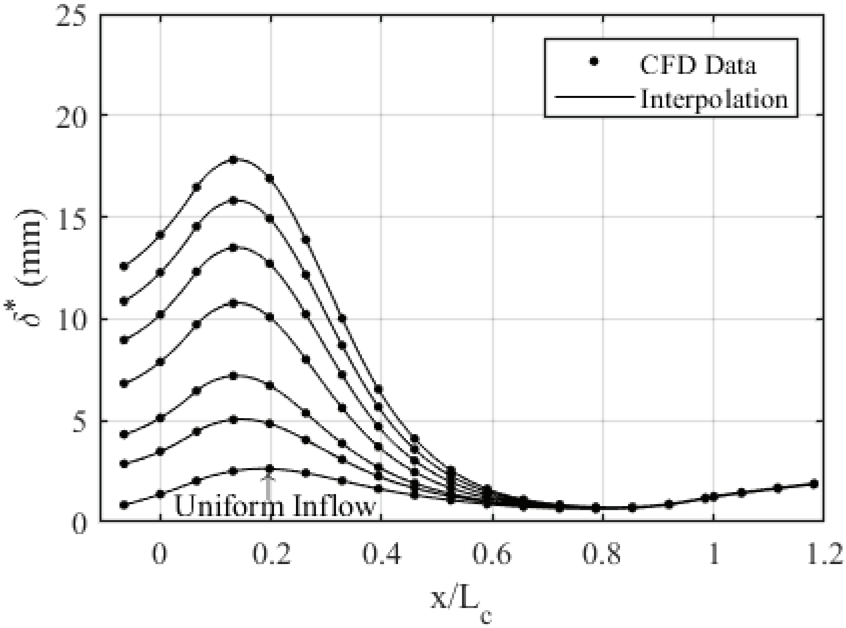

Figure 6.27: 3-D effect of δ* entering contraction on mean outflow for $Re_{Dh} = 4.12\times10^5$ at contraction inlet.

Table 6.5: Average δ* exiting the contraction based on Re_{Dh} at contraction inlet for 3-D computations.

Re_{Dh}	δ* (mm)
1.03×10^5	1.76
2.06×10^5	1.47
4.12×10^5	1.25

Table 6.6: Percent difference between average δ* exiting the contraction between 2-D and 3-D computations.

Re_{Dh}	% Difference
1.03×10^5	6.59
2.06×10^5	4.65
4.12×10^5	1.59

6.5 2-D Laminar vs. Turbulent Results

The results presented thus far suggest that the flow though the contraction follows a 2-D nature. The results also show that a uniform velocity inlet is sufficient in capturing the resulting boundary layer entering the test section. This suggests that 2-D computations through the contraction, run with a uniform inflow boundary condition, will capture the relevant physics of the resulting flow field entering the test section. There is currently no experimental data for the natural boundary layer entering the test section. In turbulent boundary-layer experiments at low Reynolds numbers that have been conducted in the previous existence of the tunnel, transition from laminar to fully turbulent flow can be forced using tripping devices while allowing the flow some distance to lose its sensitivity to upstream conditions [8]. This section exists to compare computed laminar and turbulent 2-D contraction results for future comparison with experimental results.

The development of the displacement thickness through the contraction for both laminar and k-ω SST 2-D computations is given in Figures 6.28-6.30. The turbulent results presented are taken from the uniform inflow boundary layer development presented in Section 6.2. The laminar results were computed by turning off the turbulence model in ANSYS Fluent and running a laminar case with a uniform inflow boundary condition at the contraction inlet. It is important to note that both laminar and turbulent computations were carried out at the same Reynolds numbers.

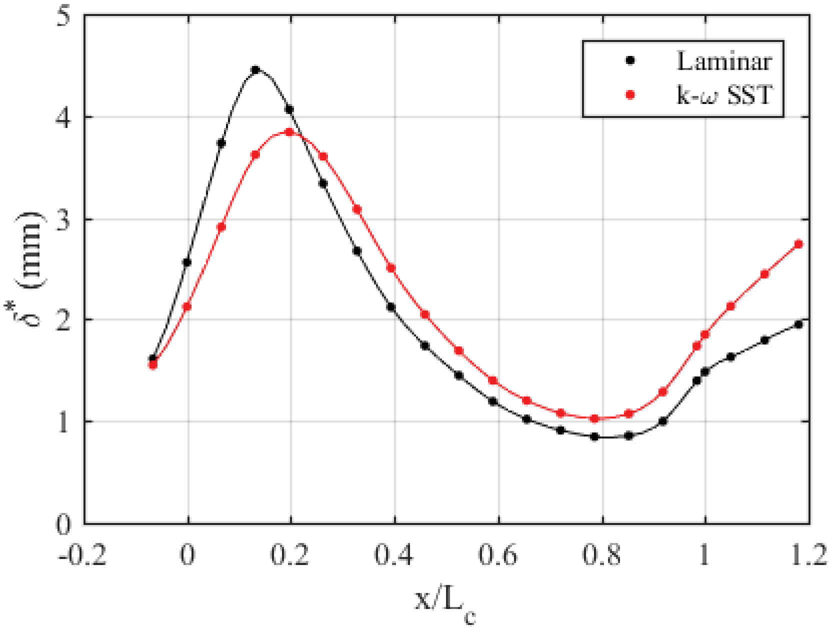

Figure 6.28: Development of δ* along the floor of the contraction for laminar and turbulent solvers at $Re_{Dh} = 1.03 \times 10^5$ at contraction inlet.

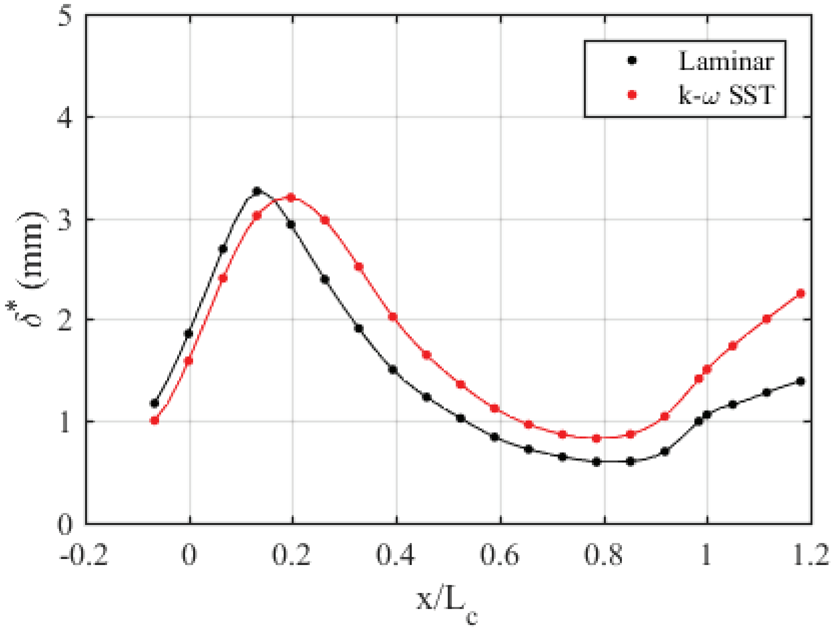

Figure 6.29: Development of δ* along the floor of the contraction for laminar and turbulent solvers at $Re_{Dh} = 2.06 \times 10^5$ at contraction inlet.

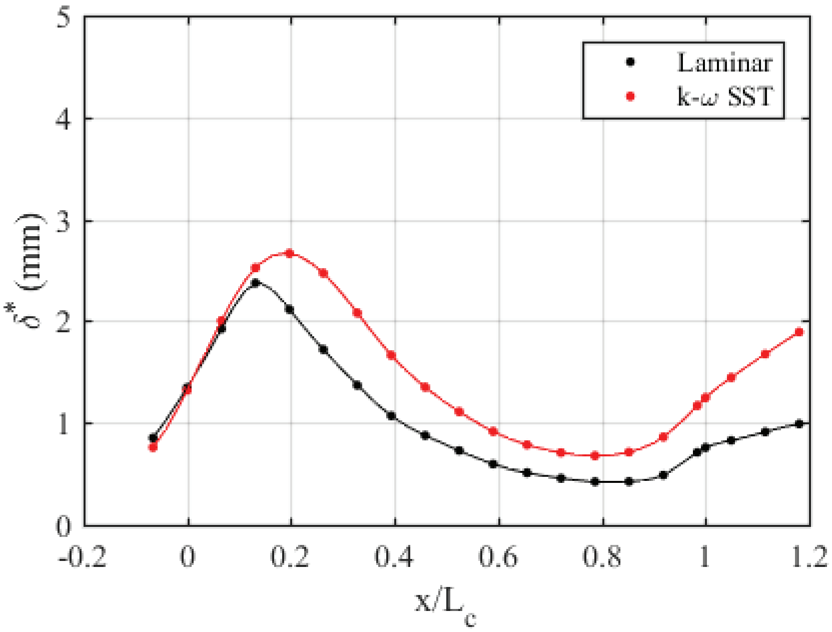

Figure 6.30: Development of δ^* along the floor of the contraction for laminar and turbulent solvers at $Re_{Dh} = 4.12\times10^5$ at contraction inlet.

A common parameter for assessing the nature of a boundary layer is the shape factor [12]. The shape factor is given by

$$H = \frac{\delta^*}{\delta_2} \tag{6.3}$$

where δ^* is the displacement thickness and δ_2 is the momentum thickness. The momentum thickness for an incompressible, flat-plate boundary layer is defined as

$$\delta_2 = \int_0^\infty \frac{u}{U_\infty}\left(1 - \frac{u}{U_\infty}\right) dy \tag{6.4}$$

where U_∞ is the free-stream velocity and u is the local streamwise flow component. For turbulent flow over a flat plate, the shape factor is given by White [12] as 1.29, whereas the Blasius result for laminar flow will yield a shape factor of 2.59. The shape factors calculated using the laminar model at the outlet of the contraction for all inflow Reynolds numbers considered are given in Table 6.7. The results are compared with the Blasius solution for laminar flow over a flat plate. The shape factors calculated using the k-ω SST model at the outlet of the contraction for all inflow Reynolds numbers considered are given in Table 6.8. The results are compared to the solution for turbulent flow over a flat plate.

Table 6.7: Shape factor assessment at contraction outlet for laminar computations.

Re_{Dh}	H	H (Blasius)	% Difference
1.03×10^5	2.797	2.59	7.69
2.06×10^5	2.836		9.07
4.12×10^5	2.855		9.73

Table 6.8: Shape factor assessment at contraction outlet for turbulent computations.

Re_{Dh}	H	H (flat plate data)	% Difference
1.03×10^5	1.570	1.29	19.58
2.06×10^5	1.504		15.32
4.12×10^5	1.440		10.99

This data will provide insight for future experimental analysis as the natural boundary layer entering the test section has not been assessed experimentally. Gaining experimental understanding with respect to the natural boundary layer development through the tunnel is important for characterizing the flow. The data suggests that the boundary layer entering the test section may very well be laminar in nature. Regardless of the natural flow conditions, it has been shown that the boundary layer can be forced fully turbulent through the test section for experimental and computational analysis [8].

It was determined from both 2-D and 3-D computations that a range of velocity profiles entering the contraction have little effect on the resulting flow exiting the contraction. This was gauged by assessing the displacement thickness throughout the contraction and determining that the displacement thickness entering the contraction has negligible influence on the displacement thickness (i.e., the blockage) entering the test section of the tunnel. Specifically, for 3-D analysis, the sensitivity between the inflow and resulting outflow was assessed by inputting turbulent duct velocity profiles and determining that that the core flow entering the test section of the tunnel remains unaffected, despite strong corner flow effects entering the contraction. The 3-D effects were assessed with visualization of the resulting velocity and vorticity profiles entering the text section. Both 2-D and 3-D analyses align with the observations of Pook and Watmuff [20], who showed that a uniform inflow condition at the inlet of the contraction appears to be sufficient to model the flow entering the test section. A full analysis of the diffuser section is included. The diffuser Reynolds numbers documented correspond to the test section velocities assessed throughout the work. This is provided in Chapter 7.

7. A PRIORI DIFFUSER ANALYSIS

ANSYS ICEM 19.1 was used to create the grids and ANSYS Fluent 19.1 was used to obtain the results. A 3-D domain was deployed for analysis. This is due to the 3-D nature of the diffuser [14], and how the 3-D geometry is likely to influence the flow. The diffuser section consists of three perforated plates with a thickness of 0.0016 m and an open area of 64%. These details are documented in Wood and Westphal [14]. For computation, the Reynolds-Stress BSL model was selected for steady analysis. The Reynolds-Stress BSL model has capabilities of solving for important turbulence flow characteristics, such as the anisotropy in the normal stresses [25] however, turbulent models can struggle to accurately predict flow-separation [35]. The pressure-based, coupled solver was implemented with second-order upwind differencing for pressure, momentum, and Reynolds Stresses terms. Again, three different Reynolds numbers of the flow were deployed for analysis corresponding to test section free-stream velocities (U_{TS}) of approximately of 7.5, 15, and 30 m/s. These Reynolds numbers were calculated with respect to the hydraulic diameter of the diffuser inlet ($D_h = 0.6929$ m). The Reynolds numbers based on the hydraulic diameter (Re_{Dh}) at the inlet of the diffuser are approximately 1.60×10^5, 3.20×10^5, and 6.41×10^5.

7.1 Diffuser Grid and Model Generation

Figure 7.1 displays the boundary conditions deployed in the diffuser as well as the grid utilized for diffuser computations. The side wall of the diffuser is removed from the figure to display the perforated plates modeled within the domain. The grid consisted of 89 CV along the *x*-axis 63 CV along the *y*-axis, and 63 CV along the *z*-axis. This equates to a total grid size of 3.45×10^5 CV. All grids were given a first cell height of 2.45×10^{-5} m at the walls. This was chosen to match a minimum y^+ value of approximately 1 [27]. The grid spacing from each wall to its parallel symmetry plane was given a ratio of 1.05, defining the growth rate from one cell height to the next, matching the spacing used in the contraction section.

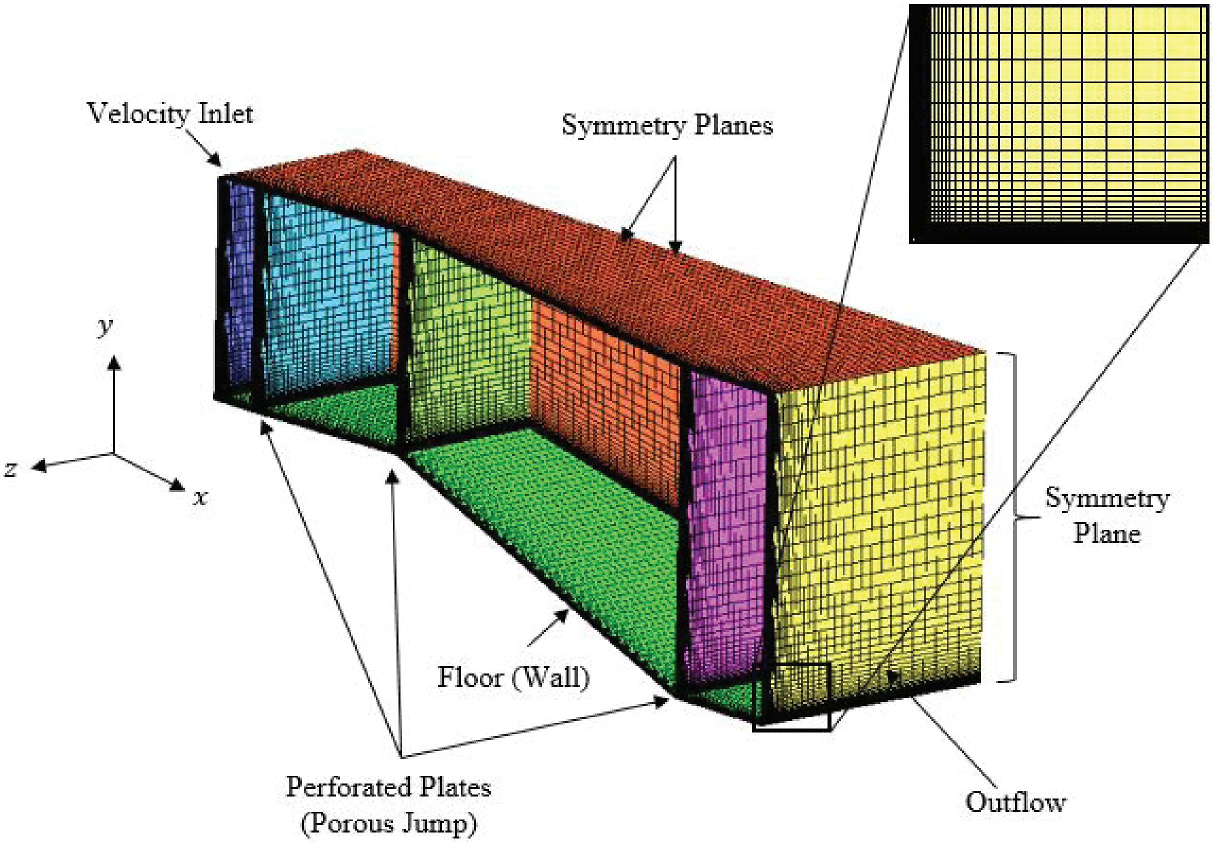

Figure 7.1: Boundary conditions and grid for diffuser simulation with corner topology.

Each perforated plate was modeled with a porous-jump boundary condition. Porous jump conditions are used to model perforated plates that have known velocity (pressure-drop) characteristics, and are essentially a 1-D simplification of a porous media model [24]. To implement the porous jump boundary condition in ANSYS Fluent, the permeability (α) and the pressure-jump coefficient (C_2) needed to be calculated. Darcy's law provides an expression for permeability [36], given by,

$$\alpha = \frac{Q\mu L}{A\Delta p} \tag{7.1}$$

where Q is the volumetric flow rate, μ is the dynamic viscosity of the fluid, L is the length of the perforated plate, A is the cross-sectional area of the porous medium, and Δp is the pressure drop across the perforated plate. The pressure drop across the plate was taken from the MATLAB analysis described in Chapter 3. The pressure-jump coefficient, C_2, can be derived based on a known pressure loss [24]. This gives:

$$C_2 = \frac{K_{grid}}{thickness} \tag{7.2}$$

where K_{grid} is the loss coefficient for the perforated plates and $thickness$ is the thickness of the plate. Table 7.1 displays the values of α and C_2 implemented for the three Reynolds numbers assessed. The value of C_2 does not change with Re_{Dh}. This is attributed to the fact that K_{grid} is a function of the geometry of the tunnel and not Re_{Dh} [18].

Table 7.1: Porous-jump coefficients.

Re_{Dh}	α (m²)	C_2 (1/m)
1.60×10^5	9.22×10^{-9}	938.52
3.20×10^5	4.61×10^{-9}	938.52
6.41×10^5	2.03×10^{-9}	938.52

7.1.1 Diffuser Grid Convergence

The 3-D diffuser section grid was verified by comparing the streamwise velocity (u) at a given point in the flow past the outlet of the diffuser, close to the center of the geometry. The Cartesian coordinate corresponding to this location is $(x, y, z) = (1.5\text{ m}, -0.3\text{ m}, 0.1\text{ m})$. The directional CVs for each grid are listed in Table 7.2, and the results of the convergence tests implemented for the considered Reynolds numbers at the inlet of the diffuser are shown in Tables 7.3-7.5. Due to the negligible difference in U between the grids described in Table 7.2, mesh 2 was deployed for analysis. The *x*-velocity residuals fell to 1×10^{-8}, however, Tables 7.3-7.5 display the results up to three decimal places.

Table 7.2: CV specifications for diffuser grid levels considered.

Mesh	***x*-axis CV**	***y*-axis CV**	***z*-axis CV**	**Total CV**
1	69	50	50	1.73×10^{5}
2	87	63	63	3.45×10^{5}

Table 7.3: Diffuser grid convergence results for inflow $Re_{Dh} = 1.60\times10^{5}$.

Mesh	**u (m/s)**	**% Difference**
1	1.577	5.1×10^{-3}
2	1.577	

Table 7.4: Diffuser grid convergence results for inflow $Re_{Dh} = 3.20\times10^{5}$.

Mesh	**u (m/s)**	**% Difference**
1	3.147	9.2×10^{-2}
2	3.144	

Table 7.5: Diffuser grid convergence results for inflow $Re_{Dh} = 6.41\times10^{5}$.

Mesh	**u (m/s)**	**% Difference**
1	6.286	7.9×10^{-2}
2	6.281	

7.2 Diffuser Analysis Results

Figures 7.2-7.7 display the C_f distributions along the floor and the wall of the diffuser as a function of Re_{Dh}. All skin-friction coefficients were calculated referenced to the uniform inlet velocity in the diffuser. There are signatures of weak flow separation through the diffuser. The regions where $C_f \approx 0$ indicates that the flow is on the verge of separation. It is imperative that these results are compared with experimental data sets as

CFD methods can struggle to predict flow separation accurately and the porous jump boundary conditions are not fully capturing the effect of the perforated plates in the diffuser. Figure 7.8 displays the C_f as a function of Re_{Dh} along the floor of the diffuser, assessed along the plane $z/W = 0$. The plot shows the locations where the porous jump boundary conditions were deployed. At these locations, the skin-friction magnitudes increase. The porous jump conditions are modeling the pressure losses through the diffuser, causing a reduction in the dynamic pressure at those locations, increasing the ratio of shear stress to dynamic pressure, i.e., the skin-friction coefficient. The plot shows that there is no separation along the center of the diffuser, however, the flow is on the verge of separation because $C_f \approx 0$. Figures 7.9-7.11 displays the streamlines through the contraction with corresponding streamwise velocity (U) profiles as a function of Re_{Dh}. The flow travels from right to left in the figures. The results show that there is a separation bubble propagating through the diffuser for a majority of the spanwise length. Figures 7.12-7.14 show the streamwise velocity profiles past the outlet of the diffuser. The results for all Reynolds numbers assessed suggest that there is no reversed flow entering the settling chamber. Although the results show that there are separation bubbles in the diffuser as well as strong corner-flow signatures, the porous jump does not model the turbulent mixing associated with the very function of the perforated plates to control separation in the diffuser. In addition, the downstream honeycomb will remove swirl and lateral mean velocity variations, straightening the flow before entering the contraction section [7]. All velocity profiles described in Figures 7.9-7.14 were non-dimensionalized with respect to the mean streamwise velocity at the center of the diffuser outlet (U_{cl}). Table 7.6 gives the values of

U_{cl} as a function of Re_{Dh}. Experimental data can help guide CFD modeling of this section, if it becomes necessary for describing the performance of the tunnel.

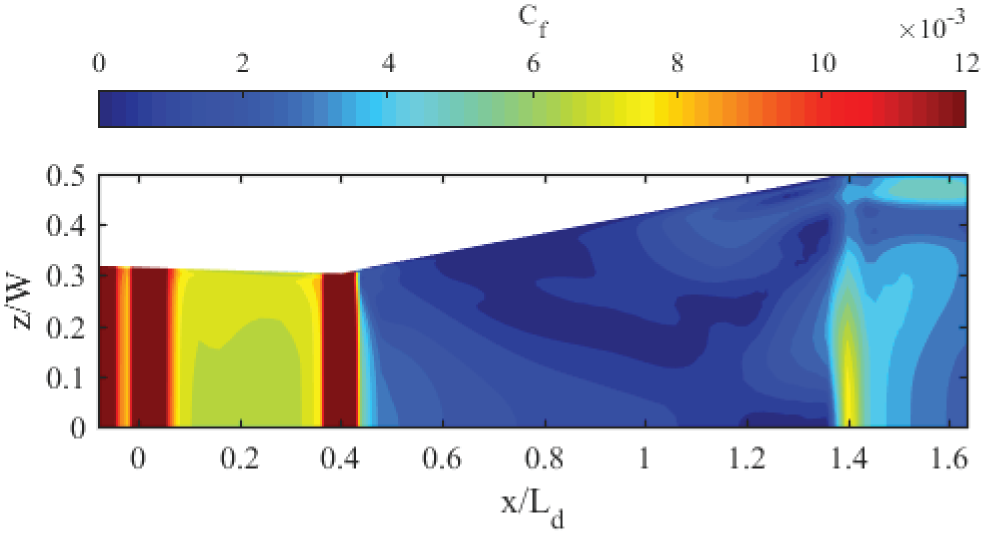

Figure 7.2: C_f distribution along diffuser floor for inflow $Re_{Dh} = 1.60\times10^5$.

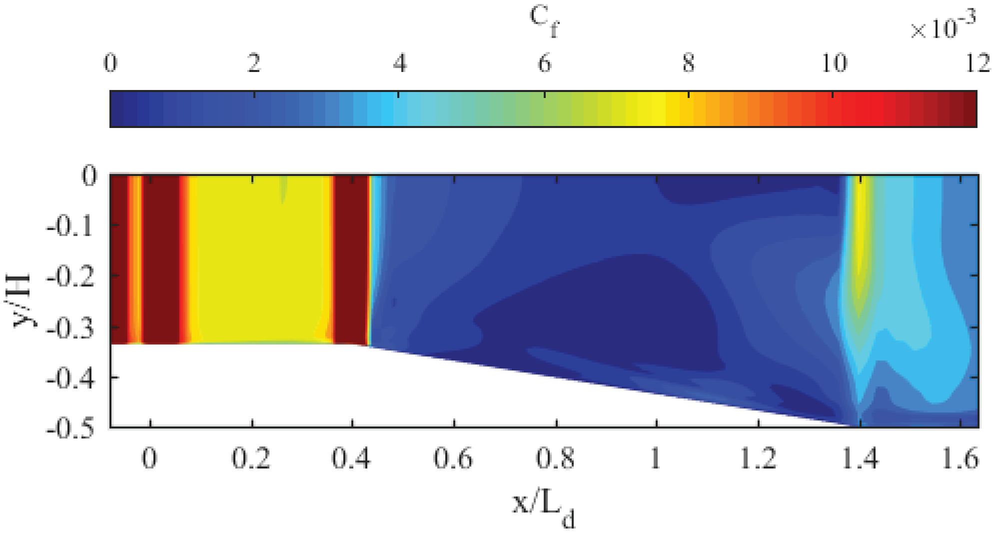

Figure 7.3: C_f distribution along diffuser sidewall for inflow $Re_{Dh} = 1.60\times10^5$.

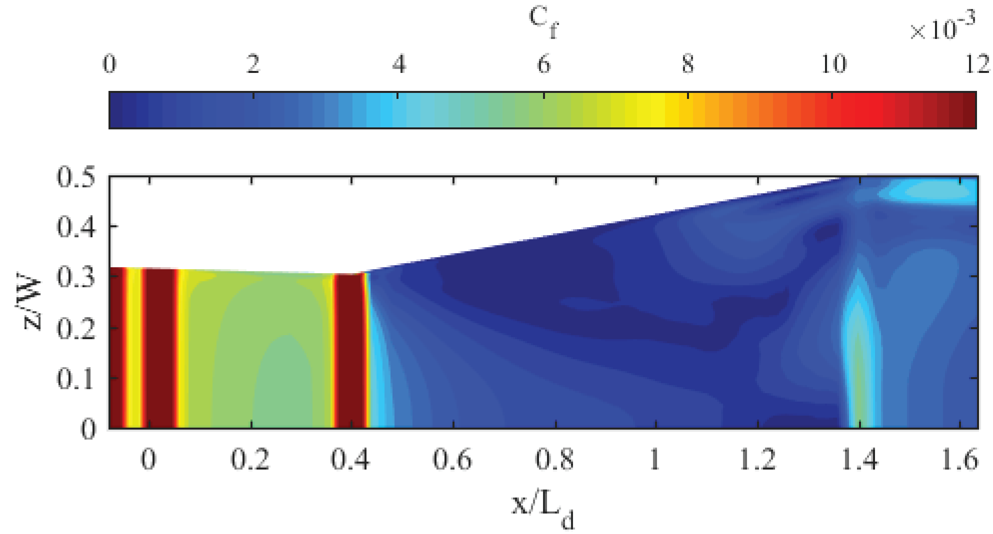

Figure 7.4: C_f distribution along diffuser floor for inflow $Re_{Dh} = 3.20\times10^5$.

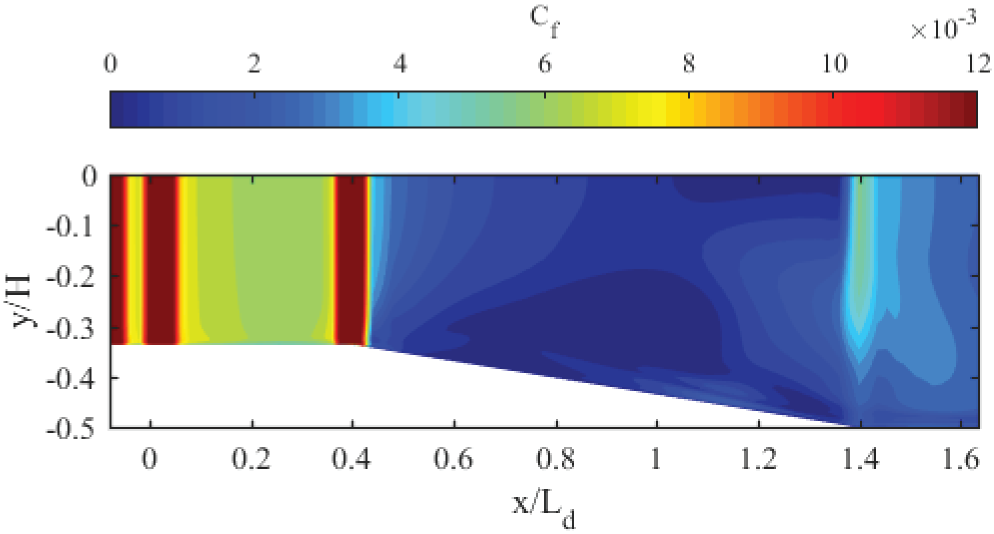

Figure 7.5*:* C_f distribution along diffuser sidewall for inflow $Re_{Dh} = 3.20\times10^5$.

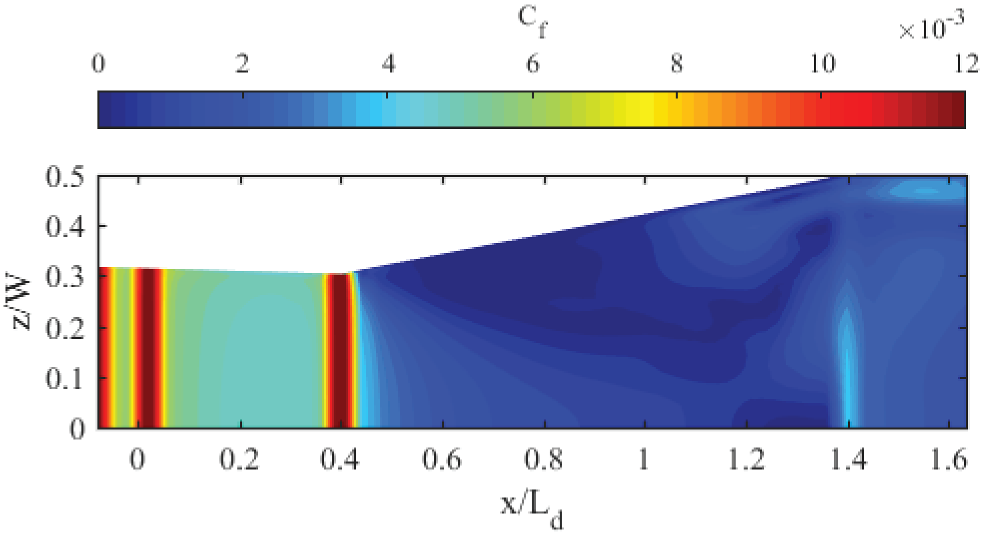

Figure 7.6: C_f distribution along diffuser floor for inflow $Re_{Dh} = 6.41\times10^5$.

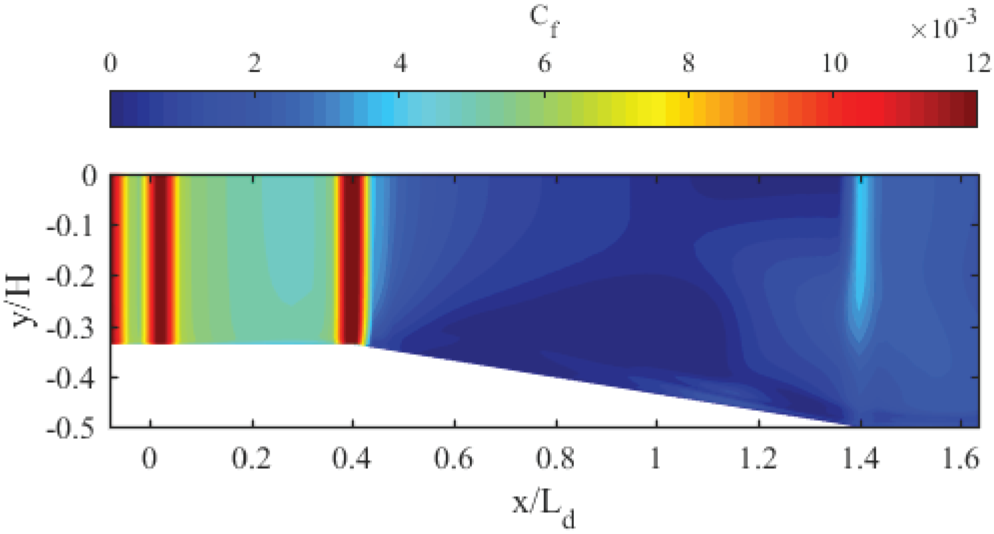

Figure 7.7: C_f distribution along diffuser sidewall for inflow $Re_{Dh} = 6.41\times10^5$.

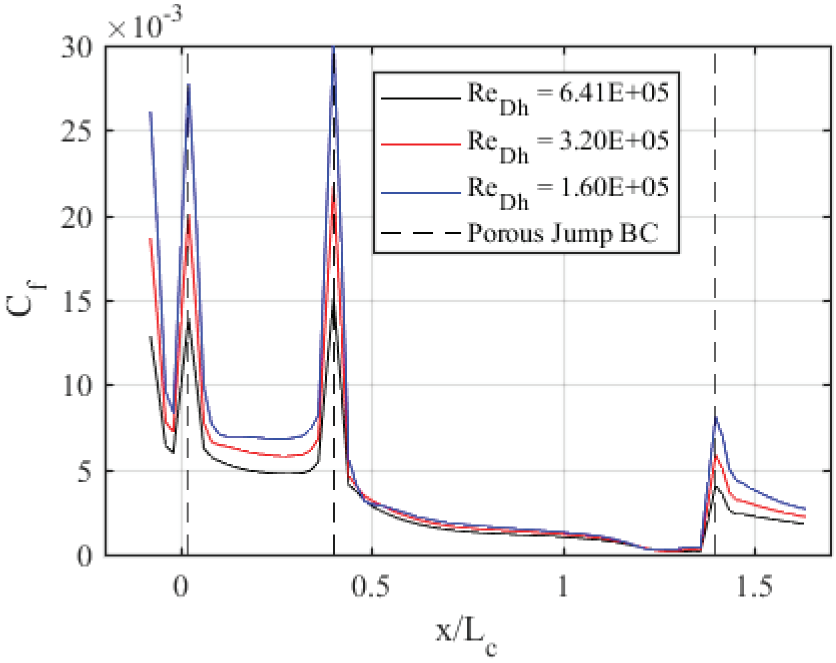

Figure 7.8: C_f distribution along diffuser floor as function of inflow Re_{Dh} assessed along centerline ($z/W = 0$).

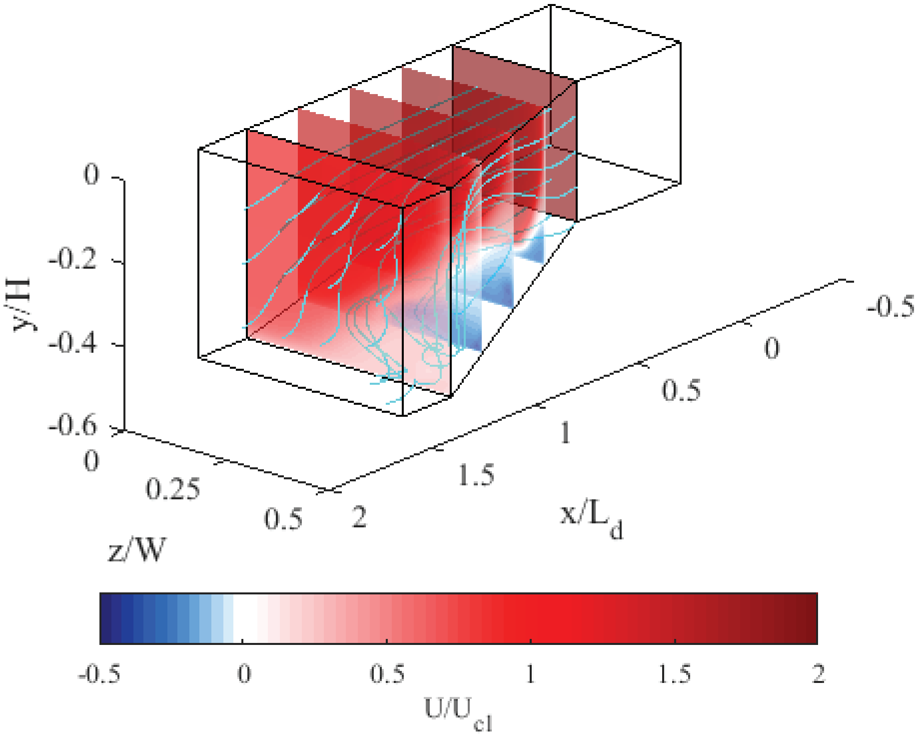

Figure 7.9: Diffuser streamlines with cross-planes of streamwise velocity for inflow $Re_{Dh} = 1.60\times10^5$.

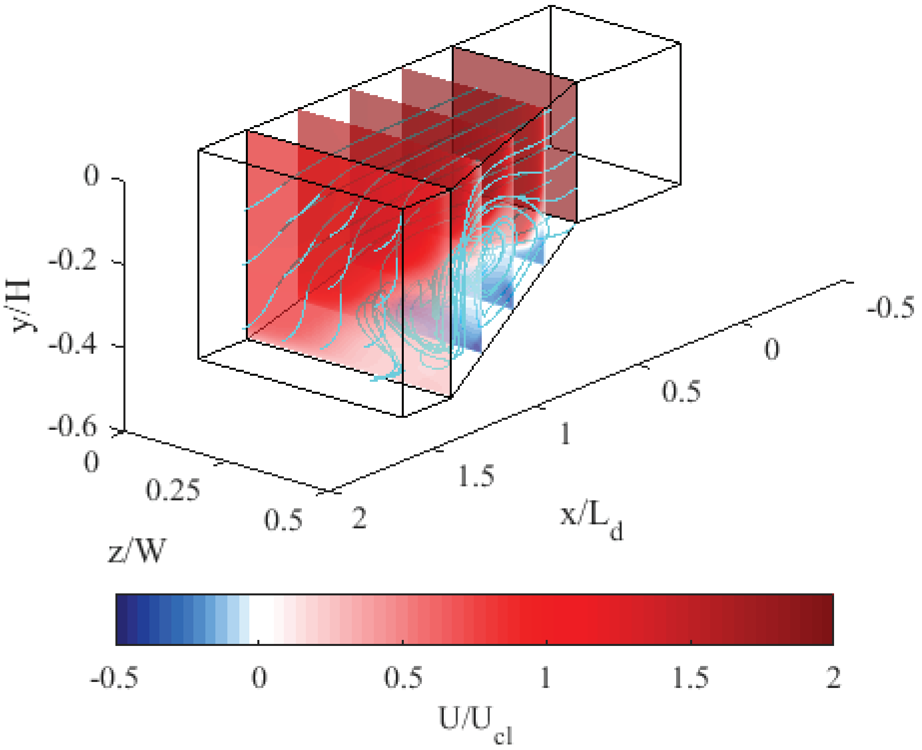

Figure 7.10*:* Diffuser streamlines with cross-planes of streamwise velocity for inflow $Re_{Dh} = 3.20\times10^5$.

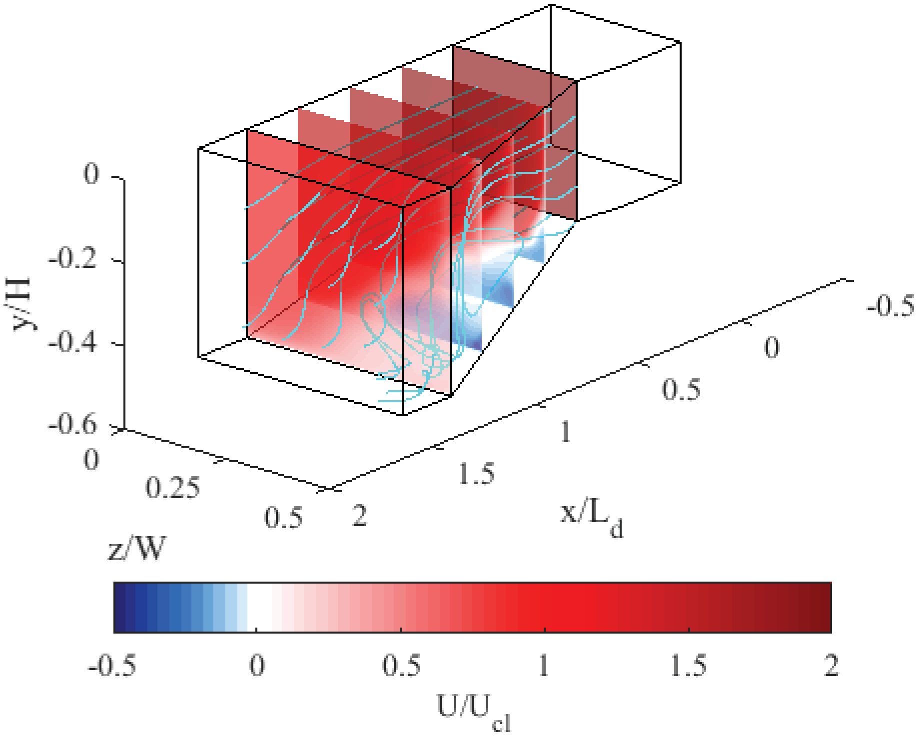

Figure 7.11: Diffuser streamlines with cross-planes of streamwise velocity for inflow $Re_{Dh} = 6.41\times10^5$.

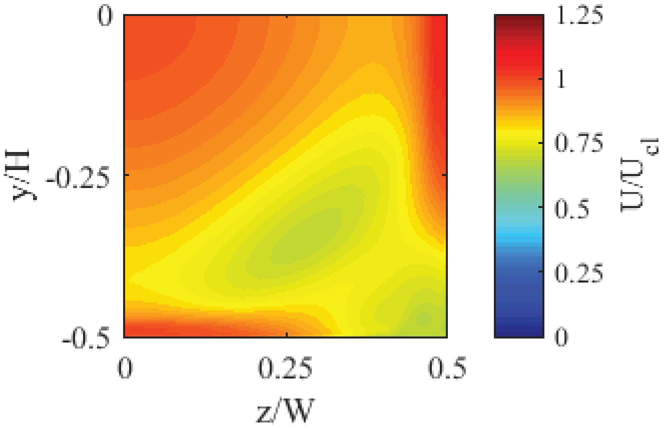

Figure 7.12: Cross-section of streamwise velocity at $x/L_d = 1.5$ (diffuser outlet) for inflow $Re_{Dh} = 1.60\times10^5$.

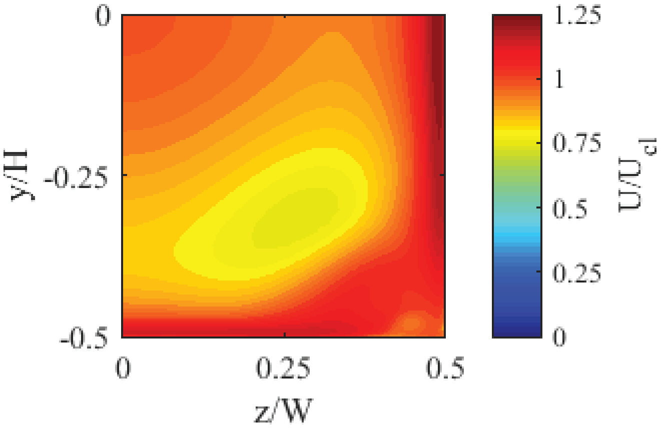

Figure 7.13: Cross-section of streamwise velocity at $x/L_d = 1.5$ (diffuser outlet) for inflow $Re_{Dh} = 3.20\times10^5$.

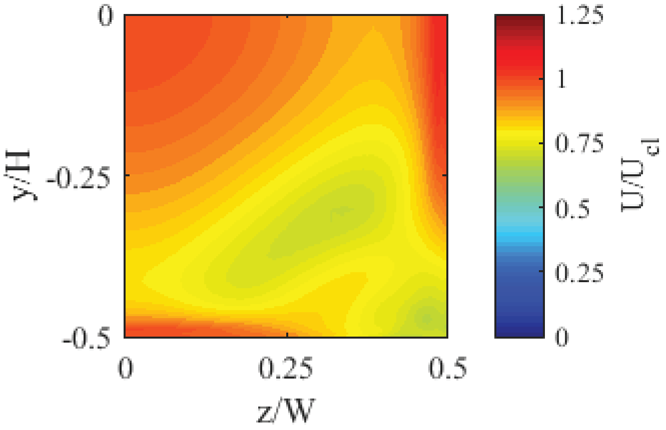

Figure 7.14: Cross-section of streamwise velocity at $x/L_d = 1.5$ (diffuser outlet) for inflow $Re_{Dh} = 6.41\times10^5$.

Table 7.6: U_{cl} used to describe all diffuser velocity profiles computed at center of diffuser outlet.

Re_{Dh}	U_{cl} (m/s)
1.60×10^5	1.753
3.20×10^5	3.223
6.41×10^5	6.995

8. CONCLUSIONS AND FUTURE WORK

This research has contributed to laying the foundational numerical analysis for future experimental comparison in a newly-constructed boundary-layer wind tunnel. This goal was achieved by deploying RANS turbulence models for analysis of the diffuser and contraction sections as functions of operating Reynolds number. This chapter exists to briefly summarize the accomplished work as well as suggest areas where future advancements can be made.

8.1 Research Summary

The tunnel was analyzed for the necessary power requirements of the centrifugal blower to achieve the desired operating envelope of the facility. The methodology for the implemented power considerations are documented with the corresponding MATLAB code shown in Appendix B. The analysis led to the conclusion that the centrifugal blower located upstream of the test section should be rated for at least 20 HP to achieve a test section velocity of approximately 30 m/s.

The geometry of the tunnel was documented throughout this work. The diffuser section was modeled based on the geometry described by Wood and Westphal [14]. Specific properties of these sections are outlined in detail. The contraction section is described as well, matching the dimensionality of the contraction described by Pook and Watmuff [20].

The contraction section of the tunnel was modeled using both 2-D and 3-D domains, with various inflow boundary-layer thicknesses and Reynolds numbers, to gauge the sensitivity between the inflow profile and resulting outflow profile. This study was useful for quantifying whether the contraction flow could be modeled as 2-D or 3-D in nature. The computations indicated that the contraction flow can be modeled as 2-D in nature. Both the 2-D and 3-D cases showed that the displacement thickness of the incoming boundary-layer at the inlet of the contraction had negligible effect on the exiting displacement thickness, which confirmed previous work by Pook and Watmuff [20]. For future CFD studies of the tunnel, the results suggest that the contraction can be modeled at high Reynolds numbers ($Re_{Dh} = 4.12 \times 10^5$ at the contraction inlet) with a 2-D domain, which is far less computationally intensive than 3-D analysis.

The diffuser section was analyzed at various Reynolds numbers to gain insight into basic flow features that may physically exist. A porous jump boundary condition was explored to model the pressure drop across perforated plates that are deployed as flow separation control devices. The results indicated separation present in the diffuser, although the effects of turbulent mixing—the primary functions of the perforated plates—were not modeled in CFD. In the physical wind tunnel, it is expected that flow non-uniformities and large-scale turbulence will be reduced as the flow passes through the honeycomb and the screens, before entering the contraction.

8.2 Recommended Future Work

It is recommended that future work should compare the CFD results presented in this thesis with experimental data. This includes assessing the contraction performance, at the same Reynolds numbers presented, by measuring the boundary layer at the test section entrance. Because present CFD models struggle to accurately predict separated flow [35], it is recommended that the diffuser performance also be quantified experimentally. By combining the strengths of CFD and experiments, it will be possible to fully understand the flow physics, allowing insight into what procedures must be followed to accurately model the boundary conditions of the tunnel.

9. REFERENCES

[1] J. Slotnick, A. Khodadoust, J. Alonso, D. Darmofal, W. Gropp, E. Lurie and D. Mavriplis, "CFD Vision 2030 Study: A Path to Revolutionary Computational Aerosciences," NASA Contractor Report, CR-2014-218178, 2014.

[2] P. Spalart and V. Venkatakrishnan, "On the role and challenges of CFD in the aerospace industry," *The Aeronautical Journal,* vol. 120, no. 1223, pp. 209-232, 2016.

[3] J. Stumpe, "Symbiosis: Why CFD and Wind Tunnels Need Each Other," *Aerospace America,* June 2018.

[4] L. Leifsson and S. Koziel, "Simulation-driven design of low-speed wind tunnel contraction," *Journal of Computational Science,* vol. 7, pp. 1-12, 2015.

[5] J. B. Barlow, W. H. J. Rae and A. Pope, Low-Speed Wind Tunnel Testing, New York, NY: John Wiley & Sons, 1999.

[6] J. Farnsworth, "Experimental Aerodynamics Laboratory," Boulder, Colorado, 2019.

[7] R. D. Mehta and P. Bradshaw, "Design rules for small low-speed wind tunnels," *The Aeronautical Journal,* vol. 83, no. 827, pp. 443-453, 1979.

[8] P. R. Sparlart and J. H. Watmuff, "Experimental and numerical study of a turbulent boundary layer with pressure gradients," *Journal of fluid Mechanics,* no. 246, pp. 337-371, 1993.

[9] G. N. Coleman and R. D. Sandberg, "A Primer on Direct Numerical Simulation of Turbulence-Methods, Procedures and Guidelines," TR AFM-09/01a, University of Southampton, 2010.

[10] P. M. Doran, Bioprocess Engineering Principles, Elsevier Ltd. , 2013.

[11] R. Hibbler, Fluid Mechanics, Pearson Prentice Hall, 2015.

[12] F. M. White, Fluid Mechanics, New York, NY: McGraw-Hill, 2009.

[13] J. E. Sandeep, S. Abhilash, S. J. Jiss, M. Abhay and K. D. Heuy, "Comparative study of boundary layer control around an ordinary airfoil and a high lift airfoil with secondary blowing," *Computers and Fluids,* vol. 164, pp. 50-63, 2018.

[14] D. H. Wood and R. V. Westphal, "Measurements of the free-stream fluctuations above a turbulent boundary," *The Physics of Fluids,* vol. 31, no. 10, pp. 2834-2840, 1988.

[15] R. Mehta, "The Aerodynamic Design of Blower Tunnels with Wide-Angle Diffusers," *Progress in Aerospace Sciences,* vol. 18, pp. 59-120, 1979.

[16] R. D. Mehta, "Turbulent boundary layer perterbed by a screen," *AIAA Journal,* vol. 23, no. 9, pp. 1335-1342, 1985.

[17] M. Blanco, J. Battiato and K. Disotell, "Sensitivity Study of Contraction Flow for Boundary-Layer Validation Wind Tunnel," in *AIAA Aviation and Aeronautics Forum and Exposition*, Dallas, 2019.

[18] W. T. Eckert, K. W. Mort and J. Jope, "Aerodynamic Design Guidelines and Computer Program for Estimation of Subsonic Wind Tunnel Performance," NASA, Moffett Field, California, 1976.

[19] S. Tavoularis, Measurement in Fluid Mechanics, New York, NY: Cambridge University Press, 2005.

[20] D. A. Pook and J. H. Watmuff, "Streak generation in wind tunnnels," *Physics of Fluids,* vol. 26, no. 7, pp. 1-19, 2014.

[21] J. H. Bell and R. Mehta, "Contraction design for small low-speed wind tunnels," NASA Contractor Report, CR-182747, 1988.

[22] P. Bradshaw, "Turbulent Secondary Flows," *Annual Review of Fluid Mechanics,* vol. 19, pp. 53-74, 1987.

[23] M. Bouriga, J.-S. M. F. Lemyre-Baron and J. Weiss, "Preliminary Experimental and Numerical Investigations of the Flow in the Contraction of a Boundary Layer Wind Tunnel," *Transactions of the Canadian Society for Mechanical Engineering,* vol. 38, no. 4, pp. 517-532, 2014.

[24] ANSYS, ANSYS Fluent theory guide, 2018.

[25] F. Menter, A. Garnaruk and Y. Egorov, "Explicit Algebraic Reynolds Stress Models for Anisotropic Wall-Bounded Flows," *Progress in Flight Physics,* vol. 3, pp. 89-104, 2012.

[26] F. Menter, "Trends and Challenges in Modelling Complex Turbulent Flows," in *Proceedings of the 14th International Conference on Fluid Flow Technologies*, Budapest, Hungary, 2009.

[27] "Compute Grid Spacing for a Given Y+," Pointwise, 27 November 2018. [Online]. Available: http://www.pointwise.com/yplus/.

[28] J. Dumais, "On the Curl of a Vector Field," *The American Mathematical Monthly,* vol. 89, no. 7, pp. 469-473, 1982.

[29] O. Wyler, "Invariant Definitions for Vector Calculus," *The American Mathematical Monthly,* vol. 75, no. 4, pp. 394-396, 1968.

[30] D. C. Wilcox, Turbulence Modeling for CFD, La Canada, California: DCW Industries, Inc., 1993.

[31] "SST-V Expected Results-2D Zero Pressure Gradient Flat Plate," 12 February 2018. [Online]. Available: http://turbmodels.larc.nasa.gov/flatplate_sst.html. [Accessed 23 November 2018].

[32] H. Fujita, H. Yokosawa and M. Hirota, "Secondary Flow of the Second Kind in Rectangular Ducts with One Rough Wall," *Experimental Thermal and Fluid Science,* vol. 2, pp. 72-80, 1989.

[33] C. G. Speziale, "Analytical Methods for the Developement of Reynolds-Stress Closures in Turbulence," NASA CR 182017, 1990.

[34] M. Bouriga, J.-S. Lemyre-Baron, F. Morency and J. Weiss, "Preliminary experimental and numerical investigations of the flow in the contraction of a boundary layer wind tunnel," *Transactions of the Canadian Society for Mechanical Engineering,* vol. 38, no. 4, pp. 517-532, 2014.

[35] R.-D. Cecora, B. Eisfeld, A. Probst, S. Crippa and R. Radespiel, "Differential Reynolds Stress Modeling for Aeronautics," *AIAA Journal,* vol. 53, no. 3, pp. 739-755, 2014.

[36] J. Byran, A. Kantzas and S. Taheri, Fundamentals of Fluid Flow in Porous Media, 2018.

[37] R. Basak, D. Mitra and A. Mazumdar, "Design of Various Components of an Open Circuit Blower Tunnel without Exit Diffuser," *International Journal of Advances in Science and Technology,* vol. 2, no. 6, pp. 88-93, 2011.

APPENDIX A: ADDITIONAL POWER CONDISERATION CODE EXPRESSIONS

This appendix documents the additional expressions that were implemented in MATLAB to account for the power considerations necessary to choose a centrifugal blower. This appendix contains a full description of various expressions used in the code that were not described in Chapter 3.

A.1 Calculating Expansion Loss Coefficient

The equations shown below were provided by Eckert, Mort, and Jope [12]. The net expansion loss coefficient for a diffuser, K_{exp}, depends on the cross-sectional shape as well as the equivalent cone angle of the section. The equivalent cone angle denotes an imaginary conical section containing an inlet and outlet area as well as a length identical to the actual section. This angle is disparate from the actual geometry of a tunnel containing a square, or rectangular diffuser.

A.1.1 Expansion Loss Coefficient for Square Cross-Section Diffusers

For a square cross-section diffuser, the expressions are,

for $0° < 2\theta < 3°$:

$$K_{exp_{Square}} = 9.62274 \times 10^{-2} - 2.07582 \times 10^{-3}(2\theta) \tag{A1.1}$$

for $3° \leq 2\theta \leq 10°$:

$$\begin{aligned} K_{exp_{Square}} = {} & 1.22156 \times 10^{-1} - 2.29480 \times 10^{-2}\,(2\theta) + 5.50704 \\ & \times 10^{-3}\,(2\theta)^2 - 4.08644 \times 10^{-4}\,(2\theta)^3 \\ & - 3.84056 \times 10^{-5}\,(2\theta)^4 + 8.74969 \\ & \times 10^{-6}\,(2\theta)^5 - 3.65217 \times 10^{-7}\,(2\theta)^6 \end{aligned} \tag{A1.2}$$

and for $2\theta > 10°$:

$$K_{exp_{Square}} = -1.321685 \times 10^{-1} + 2.293315 \times 10^{-2}\,(2\theta) \tag{A1.3}$$

A.1.2 Expansion Loss Coefficient for Rectangular Cross-Section Diffusers

For a two-dimensional diffuser with a square up-stream end cross section, the expansion loss coefficient are,

for $0° < 2\theta < 3°$:

$$K_{exp_{Rectangular}} = 1.0 \times 10^{-1} - 5.333333 \times 10^{-3}\,(2\theta) \tag{A2.1}$$

for $3° \leq 2\theta < 9°$:

$$\begin{aligned} K_{exp_{Reclangular}} = {} & 3.23334 \times 10^{-1} - 5.82939 \times 10^{-2}\,(2\theta) - 4.97151 \\ & \times 10^{-2}\,(2\theta)^2 + 1.99093 \times 10^{-2}\,(2\theta)^3 - 1.98630 \\ & \times 10^{-3}\,(2\theta)^4 + 2.06857 \times 10^{-5}\,(2\theta)^5 + 3.81387 \\ & \times 10^{-6}\,(2\theta)^6 \end{aligned} \tag{A2.2}$$

for $9° \leq 2\theta \leq 10°$:

$$K_{exp_{Rectangular}} = 5.72853 - 1.21832\,(2\theta) + 7.08483 \times 10^{-2}\,(2\theta)^2 \tag{A2.3}$$

and for $2\theta > 10°$:

$$K_{exp_{Rectangular}} = -1.36146 + 1.986460 \times 10^{-1}\,(2\theta) \tag{A2.4}$$

A.1.3 Planarity of the Diffuser

The extent to which the diffuser is planar, δ_p, is given by the following ratio,

$$\delta_p = smaller\ of\ \frac{h_2 - h_1}{w_2 - w_1}\ or\ \frac{w_2 - w_1}{h_2 - h_1} \tag{A3.1}$$

If the ratio provided in Equation A3.1 is negative,

$$\delta_p = 0 \tag{A3.2}$$

The net expansion loss coefficient for a diffuser is given by the expression

$$K_{exp} = K_{exp_{Square}} + \left(1 - \delta_p\right)\left(K_{exp_{Rectangular}} - K_{exp_{Square}}\right) \qquad \text{(A4)}$$

APPENDIX B: MATLAB CODE

This appendix documents the entire code that was implemented in MATLAB to account for the power considerations necessary to choose a centrifugal blower. The code asks the user to define the geometry of the tunnel, the properties of the air, the desired test section speed, the internal flow structure (i.e. perforated plate, screens and the honeycomb) properties, and the efficiency of the blower. After the desired inputs are set, using the functions provided by Eckert, Mort, and Jope [18], the code outputs the total pressure at various locations along the tunnel, a table documenting all of the inputs, and a table containing all outputs essential for assessing the power requirements of the tunnel. The code was implemented with the intent that that future power analysis can be carried out for altered design iterations.

B.1 Code Inputs

Tables B.1-B.3 contain the inputs required to run the code. The tables give the variables as they were defined in the code with the intention of allowing future users to track the variables throughout the script. Full descriptions are included. All of the geometry inputs described in Table B.1 are defined in m.

Table B.1: Geometry inputs.

Variable	Description
`fan_i_width`	Inlet width of fan duct
`fan_i_height`	Inlet height of fan duct
`fan_duct_length`	Length of fan duct
`diff_i_width`	Inlet width of diffuser
`diff_i_height`	Inlet height of diffuser
`diff_o_width`	Outlet width of diffuser
`diff_o_height`	Outlet height of diffuser
`diff_length`	Length of diffuser
`sc_width`	Width of settling chamber
`sc_height`	Height of settling chamber
`sc_length`	Length of settling chamber
`con_i_width`	Inlet width of contraction
`con_i_height`	Inlet height of contraction
`con_o_width`	Outlet width of contraction
`con_o_height`	Outlet height of contraction
`con_length`	Length of contraction
`ts_width`	Width of test section
`ts_height`	Height of test section
`ts_length`	Length of test section

Table B.2: Air property inputs.

Variable	Description
`ts_vel`	Test section free stream velocity (m/s)
`rho`	Air density (kg/m^3)
`mew`	Dynamic viscosity (kg/m*s)
`gamma`	Specific heat of air
`eta_f`	Efficiency of blower (%)
`p_t_atm`	Atmospheric pressure (pa)

Table B.3: Internal flow structure inputs.

Variable	Description
`grids_open_area`	Open area of grids (%)
`num_of_grids`	Number of grids throughout tunnel
`grid_length`	Thickness of each grid (m)
`mesh_open_area`	Open area of mesh (%)
`num_of_screens`	Number of screens throughout tunnel
`screen_wire_diameter`	Diameter of screen wire (m)
`cell_size`	Cell size of hexagonal honeycomb (m^2)
`cell_length`	Length of honeycomb (m)
`roughness`	Surface roughness of honeycomb (m)
`beta_h`	Honeycomb porosity

B.2 Code Outputs

Tables B.4-B.8 contain selected outputs. The outputs documented were essential in solving for the power required to drive the flow through the tunnel. The variables as they were used in the script are provided with corresponding descriptions.

Table B.4: Pressure loss coefficient outputs.

Variable	Description	Variable	Description
`K_fan`	Pressure loss coefficient through fan duct	`Ko_fan`	Pressure loss coefficient through fan duct referenced to test section
`K_diff`	Pressure loss coefficient through duffuser	`Ko_diff`	Pressure loss coefficient through diffuser referenced to test section
`K_grids`	Pressure loss coefficient through grids	`Ko_grids`	Pressure loss coefficient through grids referenced to test section
`K_honey`	Pressure loss coefficient through honeycomb	`Ko_honey`	Pressure loss coefficient through honeycomb referenced to test section
`K_sc`	Pressure loss coefficient through settling chamber	`Ko_sc`	Pressure loss coefficient through settling chamber referenced to test section
`K_screens`	Pressure loss coefficient through screens	`Ko_screens`	Pressure loss coefficient through screens referenced to test section
`K_ts`	Pressure loss coefficient through test section	`Ko_ts`	Pressure loss coefficient through test section referenced to test section
`K_exit`	Pressure loss coefficient at tunnel exit	`Ko_exit`	Pressure loss coefficient at tunnel exit referenced to test section
`K_total`	Total pressure loss coefficient through tunnel	`Ko_total`	Total pressure loss coefficient though tunnel referenced to test section

Table B.5: Total pressure outputs.

Variable	Description
`p_t_fan_kpa`	Total pressure at outlet of fan duct (kPa)
`p_t_diff_kpa`	Total pressure at inlet of diffuser (kPa)
`p_t_sc_kpa`	Total pressure in settling chamber (kPa)
`p_t_con_kpa`	Total pressure at contraction outlet (kPa)
`p_t_ts_kpa`	Total pressure in test section (kPa)

Table B.6: Reynolds number outputs.

Variable	Description
`RN_fan`	Reynolds number with hydraulic diameter as characteristic length at fan duct outlet
`RN_diff`	Reynolds number with hydraulic diameter as characteristic length at diffuser inlet
`RN_sc`	Reynolds number with hydraulic diameter as characteristic length in settling chamber
`RN_con`	Reynolds number with hydraulic diameter as characteristic length at contraction outlet
`RN_ts`	Reynolds number with hydraulic diameter as characteristic length in test section

Table B.7: Friction coefficient outputs.

Variable	Description
`lambda_fan`	Friction coefficient through fan duct
`lambda_diff`	Friction coefficient through diffuser
`lambda_honey`	Friction coefficient through honeycomb
`lambda_sc`	Friction coefficient through settling chamber
`lambda_con`	Friction coefficient through contraction
`lambda_ts`	Friction coefficient through test section

Table B.8: Blower power outputs.

Variable	Description
`P_Input`	Power necessary to drive the tunnel with no test section blockage (HP)
`P_Input_kw`	Power necessary to drive the tunnel with no test section blockage (kW)
`P_Required`	Power necessary to drive the tunnel with 30% test section blockage (HP)
`P_Required_kw`	Power necessary to drive the tunnel with 30% test section blockage (kW)

B.3 MATLAB Script

Below is the code used to solve for the power requirements of the blower in its entirety. Essential variables have been documented above. The code contains notes that are intended to make the logic simple to follow.

```
%% User-Defined Geometry

% Note: The code below focuses specifically on a wind tunnel with a
% diffuser containing a square inlet. The loss in a circular or conical
% diffuser cannot be calculated using this code as is.

geometry_prompt={'Fan Duct Inlet Width (m)', 'Fan Duct Inlet Height
(m)',...
    'Fan Duct Length (m)','Diffuser Inlet Width (m)','Diffuser Inlet
Height (m)', ...
    'Diffuser Outlet Width (m)','Diffuser Outlet Height (m)', ...
    'Diffuser Length (m)','Settling Chamber Width (m)', ...
    'Settling Chamber Height (m)','Settling Chamber Length (m)', ...
    'Contraction Inlet Width (m)','Contraction Inlet Height (m)', ...
    'Contraction Outlet Width (m)','Contraction Outlet Height (m)', ...
    'Contraction Length (m)','Test Section Width (m)', ...
    'Test Section Height (m)','Test Section Length (m)'};

geometry_title='Dimensions';
geometry_dims=[1,40];
geometry_definput=
{'0.635','0.808','0.38','0.607','0.807','1','1.2','1','1',...
    '1.2','1.165','1','1.2','1','0.24','1.524','1','0.24','3'};
geometry_answer=inputdlg(geometry_prompt,geometry_title, ...
    geometry_dims,geometry_definput);

% Fan Duct Geometry

fan_i_width=str2double(geometry_answer{1,1});
fan_i_height=str2double(geometry_answer{2,1});
fan_duct_length=str2double(geometry_answer{3,1});

% Diffuser Geometry
diff_i_width=str2double(geometry_answer{4,1});
diff_i_height=str2double(geometry_answer{5,1});
diff_o_width=str2double(geometry_answer{6,1});
diff_o_height=str2double(geometry_answer{7,1});
diff_length=str2double(geometry_answer{8,1});

% Settling Chamber Geometry
```

```
sc_width=str2double(geometry_answer{9,1});
sc_height=str2double(geometry_answer{10,1});
sc_length=str2double(geometry_answer{11,1});

% Contraction Geometry
con_i_width=str2double(geometry_answer{12,1});
con_i_height=str2double(geometry_answer{13,1});
con_o_width=str2double(geometry_answer{14,1});
con_o_height=str2double(geometry_answer{15,1});
con_length=str2double(geometry_answer{16,1});

% Test Section Geometry
ts_width=str2double(geometry_answer{17,1});
ts_height=str2double(geometry_answer{18,1});
ts_length=str2double(geometry_answer{19,1});



%% Calculate Areas w/Inputs

% Fan Duct

A_i_fan=fan_i_width*fan_i_height;
A_o_fan=diff_i_width*diff_i_height;

% Diffuser
A_i_diff=diff_i_width*diff_i_height;
A_o_diff=diff_o_width*diff_o_height;

%Settling Chamber
A_sc=sc_width*sc_height;

% Contraction
A_i_con=con_i_width*con_i_height;
A_o_con=con_o_width*con_o_height;

% Test Section
A_ts=ts_width*ts_height;

%% User-Defined Fluid Properties,Blower Efficiency, and "Factor of
Safety"
fluid_prompt={'Test Section Speed (m/s)','Density (kg/m^3)',...
    'Dynamic Viscosity (kg/m-s)',...
    'Specific Heat Ratio of Fluid.[Given is the Specific heat of
air]'...
    'Blower Efficiency (%)','Atmospheric Pressure (Pa)'};
fluid_title='Tunnel Properties';
fluid_dims=[1,40];
fluid_definput={'30','1.1498','1.8274E-5','1.4','84.84','101325'};
fluid_answer=inputdlg(fluid_prompt,fluid_title,...
    fluid_dims,fluid_definput);

% Test Section Velocity
ts_vel=str2double(fluid_answer{1,1});
```

```
% Fluid Properties
rho=str2double(fluid_answer{2,1});
mew=str2double(fluid_answer{3,1});
% Specific Heat
gamma=str2double(fluid_answer{4,1});
% Blower Efficiency
eta_f=str2double(fluid_answer{5,1})/100;
eta_f_percent=str2double(fluid_answer{5,1});
% Atmospheric Pressure
p_t_atm=str2double(fluid_answer{6,1});
p_t_atm_kpa=p_t_atm*0.001;
message=...
msgbox('All Velocities are calculated Assuming Incompressible Flow'...
,'Warning');

%% Calculate other velocities in the wind tunnel

% Velocities in the Contraction
con_o_vel=ts_vel;
con_i_vel=(con_o_vel*A_o_con)/A_i_con;

% Velocity in the Settling Chamber
sc_o_vel=con_i_vel;
sc_i_vel=sc_o_vel;

% Velocity in the Diffuser

diff_o_vel=sc_i_vel;
diff_i_vel=(A_o_diff*diff_o_vel)/A_i_diff;

% Velocity at the fan duct inlet

fan_o_vel=diff_i_vel;
fan_i_vel=(A_o_fan*fan_o_vel)/A_i_fan;


%% Reynolds Numbers



% Test Section
Dh_ts=(4*A_ts)/((2*ts_width)+(2*ts_height));
RN_ts=(rho*ts_vel*Dh_ts)/mew;

% Settling Chamber

Dh_sc=(4*A_sc)/((2*sc_width)+(2*sc_height));
RN_sc=(rho*sc_i_vel*Dh_sc)/mew;

% Contraction Section
Dh_con=(4*A_o_con)/((2*con_o_width)+(2*con_o_height));
RN_con=(rho*con_o_vel*Dh_con)/mew;

% Diffuser
Dh_diff=(4*A_i_diff)/((2*diff_i_width)+(2*diff_i_height));
```

```
RN_diff=(rho*diff_i_vel*Dh_diff)/mew;

% Fan Duct
if A_i_fan < A_o_fan
Dh_fan=(4*A_i_fan)/((2*fan_i_width)+(2*fan_i_height));
else
Dh_fan=Dh_diff;
end

RN_fan=(rho*diff_i_vel*Dh_fan)/mew;
%% Lambdas(Friction Coefficient For Smooth Pipes) Calculation

% Test Section
syms lambda_1

sym_ts_lambda=vpasolve(((log10(lambda_1*(RN_ts^2))-0.8)^-2)-lambda_1
...
    == 0,lambda_1);

lambda_ts=double(sym_ts_lambda);

%Settling Chamber
syms lambda_2

sym_sc_lambda=vpasolve(((log10(lambda_2*(RN_sc^2))-0.8)^-2)-lambda_2
...
    == 0,lambda_2);

lambda_sc=double(sym_sc_lambda);

%Contraction
syms lambda_3

sym_con_lambda=vpasolve(((log10(lambda_3*(RN_con^2))-0.8)^-2)-lambda_3
...
    == 0,lambda_3);

lambda_con=double(sym_con_lambda);

%Diffuser
syms lambda_4

sym_diff_lambda=vpasolve(((log10(lambda_4*(RN_diff^2))-0.8)^-2)-
lambda_4 ...
    == 0,lambda_4);

lambda_diff=double(sym_diff_lambda);

%Fan Duct
syms lambda_5

sym_fan_lambda=vpasolve(((log10(lambda_5*(RN_fan^2))-0.8)^-2)-lambda_5
...
    == 0,lambda_5);
```

```
lambda_fan=double(sym_fan_lambda);
%% Loss in the Test Section, Contraction Section, and Settling Chamber

% Formulas Taken from "Aerodynamic Design Guidlines and Computer
% Program for Estimation of Subsonic Wind Tunnel Performance"
% Eckert,Jope,Mort-1976
%Nasa Ames Research Center

%Test Section Loss
K_ts=(lambda_ts*ts_length)/Dh_ts; %Section 1 pg.6

%Settling Chamber Loss
K_sc=(lambda_sc*sc_length)/Dh_sc; %Section 1 pg. 6

%Contraction Section Loss
K_con=0.32*((lambda_con*con_length)/Dh_con); %Section 3 pg. 6

%Fan Duct Loss
K_fan=(lambda_fan*fan_duct_length)/Dh_fan;
%% Calculating the Net Expansion Loss Coefficient (Kexp) for the dif-
fuser

%Solving for Kexp based on user defined inputs


%The equations below are from appendix B of "Aerodynamic Design Guide-
lines
%and computer Program for Estimation of Subsonic WInd Tunnel Perfor-
mance".


%Solving for the diffuser cone angle
two_theta=2*atand((sqrt(A_o_diff)-
sqrt(A_i_diff))/(diff_length*sqrt(pi)));
theta=two_theta/2;

% Term for a square cross-section diffuser (Kexp_square)

if (0<two_theta) && (two_theta<3)

    Kexp_square=9.62274E-2-(2.07582E-3*(two_theta)); %Equation B8

elseif (3<=two_theta) && (two_theta<=10)


    Kexp_square=(1.22156E-1)-(2.29480E-2*(two_theta))+(5.50704E-3* ...
        (two_theta^2))-(4.086644E-4*(two_theta^3))-(3.84056E-5*...
        (two_theta^4))+(8.74969E-6*(two_theta^5))-(3.65217E-7 * ...
        (two_theta^6)); %Equation B7

else
```

```
Kexp_square=-1.321685E-1+(2.93315E-2*(two_theta)); %Equation B9

end

% Term for a two_dimensional diffuser with a square upstream-end
% cross-section (Kexp_square)

if (0< two_theta) &&  (two_theta <3)

Kexp_2D_Rectangular=1.0E-1 - (5.333333E-3*two_theta); %Equation B12

elseif (3<= two_theta) && (two_theta <9)

 Kexp_2D_Rectangular=3.23334E-1-(5.82939E-2*(two_theta))- ...
        (4.97151E-2*(two_theta^2))+(1.99093E-2*(two_theta^3)) - ...
        (1.98630E-3*(two_theta^4))+(2.06857E-5*(two_theta^5))+...
        (3.81387E-6*(two_theta^6)); %Equation B10

elseif (9<= two_theta) && (two_theta<=10)

Kexp_2D_Rectangular=5.72853-(1.21832*two_theta)+ ...
        (7.08483E-2*(two_theta^2)); %Equation B11

else

 Kexp_2D_Rectangular=-1.36146+(1.986460E-1*(two_theta)); %Equation B13

end

%Solving for the extent to which the diffuser is planar. Corresponds to
% an equation found on page 37 (Appendix B) of the report

delta_test1=(diff_o_height-diff_i_height)/(diff_o_width-diff_i_width);
delta_test2=(diff_o_width-diff_i_width)/(diff_o_height-diff_i_height);

if (delta_test1<0) && (delta_test2<0)

    delta_s=0;

elseif delta_test1 >= delta_test2

delta_s=delta_test2;

else

delta_s=delta_test1;
end

%Setting conditionals to solve for a final Kexp

%The equation, B14 gives...
%Kexp=Kexp_basic + (1-delta_s)*(Kexp_additional-Kexp_basic). Kexp_basic
```

```
%in this case will be Kexp_square. If the diffuser is a 2-D diffuser,
the
%Kexp_additional will be defined by Kexp_2D_rectangular. If not, the
%Kexp_additional will be 0. In this case, Kexp=Kexp_basic.

Kexp_basic=Kexp_square;
Kexp_additional=Kexp_2D_Rectangular;

if diff_i_width < diff_o_width

    Kexp=Kexp_basic+((1-delta_s)*(Kexp_additional-Kexp_basic)); %Equa-
tion B14

else

    Kexp=Kexp_basic;

end



%% Loss in the Diffuser

%Area Ratio Calculation
diff_AR=A_o_diff/A_i_diff;

%Simplifying the Loss equation with constants

diff_constant_1=(diff_AR+1)/(diff_AR-1);
diff_constant_2=lambda_diff/(8*sind(theta));
diff_constant_3=((diff_AR-1)/diff_AR)^2;

%Diffuser Loss

K_diff=(Kexp+(diff_constant_1*diff_constant_2))*diff_constant_3; %Sec-
tion 6 pg.7


%% User Defined Internal Wind-Tunnel Structures

flow_prompt={'How much open area do the grids provide? (%)', ...
    'How many grids are there?', 'Length of Each Grid (m)', ...
    'How much open area does the mesh provide? (%)','How many screens
are there?', ...
    'Screen Wire Diameter','Cell Size of hexagonal honeycomb? (m)',...
    'Length of honeycomb (m)',...
    'Surface Roughness of Honeycomb (m) [Note:Given input is the sur-
face roughness of aluminum]',...
    'Porosity of Honeycomb (%)'};

flow_title='Internal Wind Tunnel Geometry';
flow_dims=[1,40];
```

```
flow_definput={'64','3','0.0016','62.9','4','1.14E-
4','0.00476','0.038','1.5E-6','96.6'};
flow_answer=inputdlg(flow_prompt,flow_title,...
    flow_dims,flow_definput);

% Grid Properties
grids_open_area=str2double(flow_answer{1,1})/100;
grids_open_area_percentage=str2double(flow_answer{1,1});
num_of_grids=str2double(flow_answer{2,1});
grid_length=str2double(flow_answer{3,1});

% Mesh Properties
mesh_open_area=str2double(flow_answer{4,1})/100;
mesh_open_area_percentage=str2double(flow_answer{4,1});
num_of_screens=str2double(flow_answer{5,1});
screen_wire_diameter=str2double(flow_answer{6,1});
% Honeycomb Properties
cell_size=str2double(flow_answer{7,1});
cell_length=str2double(flow_answer{8,1});
roughness=str2double(flow_answer{9,1});
beta_h=str2double(flow_answer{10,1})/100;
beta_h_percentage=str2double(flow_answer{10,1});




%% Loss from the grids in diffuser (perforated plates)


%Simplying the terms in the equation

grids_A=A_i_diff;

grids_Aflow=grids_open_area*grids_A;

grids_constant_1=sqrt((1/2)*(1-(grids_Aflow/grids_A))); %First term of
loss Eq.

grids_constant_2=1-(grids_Aflow/grids_A); %Second Term of loss Eq.

grids_constant_3=grids_A/grids_Aflow; %Third term of loss Eq.

K_grids=(((grids_constant_1+grids_constant_2)*grids_constant_3)^2) ...
    * num_of_grids; %Equation in section 12, page 9 of the report


%% Loss From the Screens

K_mesh=1.3; %This is assuming average circular metal wire

% K_mesh=1 for new metal wire
% K_mesh=2.1 for silk thread
```

```
%Note:The screens are located upstream of the settling chamber
% for this particular wind tunnel. If the screens are moved to another
%location, the code would have to be changed accordingly.

mesh_A=A_sc;
mesh_Aflow=mesh_open_area*mesh_A;

if (0<=RN_sc) && (RN_sc<=400)

    K_RN=((78.5*(1-(RN_sc/354)))/100)+1.01; %Equation B15

else

    K_RN=1;

end

% Simplifying the loss equation

mesh_constant_1=1-(mesh_Aflow/mesh_A);
mesh_constant_2=((mesh_A/mesh_Aflow)-1)^2;

K_screens=((K_RN*K_mesh*mesh_constant_1)+mesh_con-
stant_2)*num_of_screens;
% The equation above is equation from section 13.

%% Loss in the honeycomb

%The honeycomb section describes by Wood and Westphal gives 0.0025 wall
%thickness Aluminum.(hexagonal section)

%Cell size:0.476 cm = 0.00476 m
%Cell length: 3.8 cm = 0.038 m

%Note: From Barlow, Rae, and Pope , "Low-Speed wind tunnel testing",
%"Porosity is typically in the vicinity of 0.8"




%Honeycomb Hydraulic Diameter for a hexagonal section
Dh_honey=cell_size;

%Reynolds Number used to find the loss in the Honeycomb

RN_honey=(rho*sc_o_vel*Dh_honey)/mew;

if (RN_honey <= 275)

lambda_honey=0.375*(RN_honey^-0.1)*((roughness/Dh_honey)^0.4); %Section
9
```

```
else

 lambda_honey=0.214* ((roughness/Dh_honey)^0.4); %Section 9

end

% The equation used to calculate the loss in the honeycomb was found in
% a book entitled "Low-Speed Wind Tunnel Testing" by Barlow, Rae, and
Pope
% on page 90. (Eq 3.43). This equation is also provided in the Eckert
% report on page 8. (Section 9).

%Simplifying the equation

honey_constant_1=((cell_length/Dh_honey)+3);
honey_constant_2=(1/beta_h)^2;
honey_constant_3=((1/beta_h)-1)^2;

K_honey=(lambda_honey*honey_constant_1*honey_constant_2)+honey_con-
stant_3;
%% Loss Due to kinetic energy of exiting flow

% Mach Number at exit
%Defining the mach number and Area of the test section
c=343; %Speed of sound in m/s

M_exit=ts_vel/c;

% The constants below correspond to section 7, page 8 of the report.
% Simplifying the constants

Exit_1=((gamma-1)/2)*(M_exit^2);
Exit_2=gamma/(gamma-1);
Exit_3=gamma*(M_exit^2);

K_exit=(2*(((1+Exit_1)^Exit_2)-1))/Exit_3; %Page 8

%Summing all of the K Values
K_total=K_con+K_sc+K_diff+K_grids+K_honey+K_screens+K_ts+K_exit;
%% Converting to Ko (loss must be referenced to the test section)

% Test Section does not need converted
Ko_ts=K_ts;

%Defining the mach number and Area of the test section
c=343; %Speed of sound in m/s

M_o=(ts_vel)/c;
A_o=A_ts;
```

```
% All of the constants for simplifying the Ko equation will be given
the
% Variable Z to avoid confusion.

%Z1=1+[((gamma-1)/2)*M_o^2]
%Z2=1+[((gamma-1)/2)*M_section^2]
%Z3=(A_o*M_section)/(A_section*M_o)

%Plugging the constants into the equation found in section 18 of
%"Aerodynamic Design Considerations...." Gives...

%Ko=K*[Z3*sqrt(Z1/Z2)]

%The first constant, Z1, is the same for all of the sections

Z1=1+(((gamma-1)/2)*M_o^2);

%For the calculation, local conditions are defined by the smallest-area
end

% Contraction Section
M_con=con_o_vel/c;
Z2_con=1+(((gamma-1)/2)*M_con^2);
Z3_con=(A_o*M_con)/(A_o_con*M_o);
Ko_con=K_con*(Z3_con*sqrt(Z1/Z2_con));

% Settling Chamber
M_sc=sc_i_vel/c;
Z2_sc=1+(((gamma-1)/2)*M_sc^2);
Z3_sc=(A_o*M_sc)/(A_sc*M_o);
Ko_sc=K_sc*(Z3_sc*sqrt(Z1/Z2_sc));

%Diffuser
M_diff=diff_i_vel/c;
Z2_diff=1+(((gamma-1)/2)*M_diff^2);
Z3_diff=(A_o*M_diff)/(A_i_diff*M_o);
Ko_diff=K_diff*(Z3_diff*sqrt(Z1/Z2_diff));

%Grids
M_grids=diff_i_vel/c;
Z2_grids=1+(((gamma-1)/2)*M_grids^2);
Z3_grids=(A_o*M_grids)/(A_i_diff*M_o);
Ko_grids=K_grids*(Z3_grids*sqrt(Z1/Z2_grids));

%Honeycomb


M_honey=sc_i_vel/c;
Z2_honey=1+(((gamma-1)/2)*M_honey^2);
Z3_honey=(A_o*M_honey)/(A_sc*M_o);
Ko_honey=K_honey*(Z3_honey*sqrt(Z1/Z2_honey));

%Screens
M_screens=sc_i_vel/c;
Z2_screens=1+(((gamma-1)/2)*M_screens^2);
```

```
Z3_screens=(A_o*M_screens)/(A_sc*M_o);
Ko_screens=K_screens*(Z3_screens*sqrt(Z1/Z2_screens));

%Exit
M_exit=ts_vel/c;
Z2_exit=1+(((gamma-1)/2)*M_exit^2);
Z3_exit=(A_o*M_exit)/(A_ts*M_o);
Ko_exit=K_exit*(Z3_exit*sqrt(Z1/Z2_exit));

%Fan Duct
if A_i_fan < A_o_fan
M_fan=fan_i_vel/c;
else
M_fan=M_diff;
end

Z2_fan=1+(((gamma-1)/2)*M_fan^2);
Z3_fan=(A_o*M_fan)/(A_o_fan*M_o);
Ko_fan=K_fan*(Z3_fan*sqrt(Z1/Z2_fan));

%% Solving for the power input


% Summing all of the Ko's
Ko_to-
tal=Ko_con+Ko_sc+Ko_diff+Ko_grids+Ko_honey+Ko_screens+Ko_ts+Ko_exit+Ko_
fan;



% Eckert,Mort and Jope give,
% P_input=[Ko_total*(rho_o^2)*A_o*(V_o^3)]/(2*eta_f*rho_f)
% where rho_f is the static density at the fans, eta_f is the effi-
ciency of
% the blower (%), V_o is the T.S. velocity, A_o is the cross-sectional
area of
% the T.S., rho_o is the density in the T.S., and Ko_total is the
% summation of the section total pressure losses refernced to the T.S.
% conditions.

rho_o=rho;
rho_f=rho;
A_o=A_ts;
V_o=ts_vel;



%The equation below corresponds to the assumption that rho_o=rho_f;

P_input=(Ko_total*(rho_o)*A_o*(V_o^3))/(2*eta_f); %(Watts)

% Conversion from Watts to Horsepower
P_Input=P_input*0.00134102;

% Conversion to Kw
P_Input_kw=P_input/1000;
```

```
%% "Factor of Safety"

% To implement the "factor of safety", a K for an internal flow ob-
struction
% was added to the calculation. The equation used was provided by Eck-
ert,
% on page 9, section 11 of the report. The blockage considered was a
% Forward facing step that faces the flow and spans the full width of
the
% test section. The maximum height of the obstruction was taken at 30%
of
% the height of the test section. Epsilon was taken as 1 and Cd was
taken
% as 1.1 (the step is a bluff body).

Cd=1.1;
epsilon=1;
A_flow_drag=(ts_height-(0.3*ts_height))*ts_width; %m^2
S=(0.3*ts_height)*ts_width; %m^2 (Drag area of flow obstruction)
K_drag=Cd*(S/A_flow_drag)*epsilon;



% Calculating Velocity based on geometry
V_drag=(A_ts*V_o)/A_flow_drag;

%Mach Number
M_drag=V_drag/c;

% Referencing Loss to the Test Section
Z1=1+(((gamma-1)/2)*M_o^2);
Z2_drag=1+(((gamma-1)/2)*M_drag^2);
Z3_drag=(A_o*M_drag)/(A_flow_drag*M_o);
Ko_drag=K_drag*(Z3_drag*sqrt(Z1/Z2_drag));

Ko_to-
tal_new=Ko_con+Ko_sc+Ko_diff+Ko_grids+Ko_honey+Ko_screens+Ko_ts+...
    Ko_exit+Ko_drag;

%% Calculating the New Power Input with the Internal flow Obstruction

%The equation below corresponds to the assumption that rho_o=rho_f;

P_required=(Ko_total_new*(rho_o)*A_o*(V_o^3))/(2*eta_f); %(Watts)

% Conversion from Watts to Horsepower
P_Required=P_required*0.00134102;

% Conversion to Kw
P_Required_kw=P_required/1000;

%% Outputting the Results to the User

% All prompts in this section are given the variable TXT
```

```
TXT_1=['In order to drive the tunnel with a test section velocity of '
...
    num2str(V_o),' m/s,','the power requirment of the blower is ', ...
    num2str(P_Input),' HP.'];
disp(TXT_1);

TXT_2=['Accounting for a flow obstruction in the test section that
spans'...
    ' the entire width of the the test section and has a height of 30%
of'...
    ' the test section height,' ];
disp(TXT_2);

TXT_3=['implemented to err on the side of caution,'...
   ' the power requirement is ' num2str(P_Required),' HP.'];
disp(TXT_3)

TXT_4=['The velocity of the air leaving the outlet of the blower
should'...
    ' be approximately ' num2str(fan_i_vel), ' m/s.'];
disp(TXT_4)

%% Pressure Constants

% Eckert et al. (Page 10) gives an expression that accounts for the
% Pressure difference across the wind tunnel, determining the minimum
% required structural strength for each section.

%List of Required inputs
% 1.) p_t_atm = atmospheric(barometric) pressure, (N/m^2) (Pa)
% 2.) p_t_sc = total (stagnation) pressure in the circuit settling
chamber
% 3.) q_o = test section dynamic pressure (rho_o*V_o^2)/2

% Test Section Dynamic Pressure (pa)
q_o=(rho_o*(V_o^2))/2;
% Test Section Dynamic Pressure (Kpa)
q_o_kpa=q_o*0.001;
% All constants for the calculation are given the variable W
W_1=gamma/(gamma-1);
W_2=(gamma-1)/2;

%% Solving for Dynamic Pressures in Each Section
% Solving for the Dynamic Pressures in each section...
% q in the test section (Pa)(q=dynamic pressure)
q_ts=q_o;
% q in the test section (Kpa)
q_ts_kpa=q_ts*0.001;
% Taking the downstream (outlet) velocity of the Contraction
V_con=con_o_vel;
% q in the contraction (Pa)
q_con=(rho*(V_con^2))/2;
% q in the contraction (KPa)
q_con_kpa=q_con*0.001;
% Velocity in the Settling Chamber
```

```
V_sc=sc_i_vel;
% q in the settling Chamber (Pa)
q_sc=(rho*(V_sc^2))/2;
% q in the settling Chamber (KPa)
q_sc_kpa=q_sc*0.001;
% Velocity in the diffuser (Inlet)
V_diff=diff_i_vel;
% q in the Diffuser (Pa)
q_diff=(rho*(V_diff^2))/2;
% q in the Diffuser (KPa)
q_diff_kpa=q_diff*0.001;
% Velocity in the fan duct (outlet)
V_fan=fan_o_vel;
% q in the fan duct (Pa)
q_fan=(rho*(V_fan^2))/2;
% q in the Fan duct (KPa)
q_fan_kpa=q_fan*0.001;

%% Solving for the Total Pressure at the Inlet
% Solving for the total pressure at the inlet requires using the
% Pressure loss coefficients (K's) calculated throughout the
% tunnel and relating them to the dynamic pressures (q's). The total
% pressure at the inlet of the tunnel was assigned the variable
% p_t_fan

% Total Pressure at Fan Outlet (Pa)
p_t_fan=p_t_atm + ((K_exit+K_ts)*q_ts) + (K_con*q_con) + ...
    ((K_sc+K_honey+K_screens)*q_sc) + ((K_grids+K_diff)*q_diff) + ...
    (K_fan*q_fan);
% Total Pressure at Fan Outlet (KPa)
p_t_fan_kpa=p_t_fan*0.001;
%% Pressure Differential in the Fan Duct (Outlet)
% The Equation used to solve for the pressure loss is found in Appendix
A
% of the Eckert Paper (Page 33). The equation is Delta_pi=p_t_atm-pi
% where p_t_atm is the atmoshperic pressure (pa) and pi is the local
static
% pressure (pa) in the section.

% Local Static Pressure Denominator
p_fan_den=(1+(W_2*(M_fan^2)))^W_1;
% Local Static Pressure (Pa)
p_fan=p_t_fan/p_fan_den;
% Local Static Pressure (KPa)
p_fan_kpa=p_fan*0.001;
% Pressure Differential (Pa)
delta_p_fan=abs(p_t_atm-p_fan);
% Pressure Differential (KPa)
delta_p_fan_kpa=abs(p_t_atm_kpa-p_fan_kpa);
%% Pressure Differential in the Diffuser (Inlet)
% Total Pressure at Fan Outlet (Pa)
p_t_diff=p_t_atm + ((K_exit+K_ts)*q_ts) + (K_con*q_con) + ...
    ((K_sc+K_honey+K_screens)*q_sc) + ((K_grids+K_diff)*q_diff);
% Total Pressure at Fan Outlet (KPa)
p_t_diff_kpa=p_t_diff*0.001;
```

```
% Local Static Pressure Denominator
p_diff_den=(1+(W_2*(M_diff^2)))^W_1;
% Local Static Pressure (Pa)
p_diff=p_t_diff/p_diff_den;
% Local Static Pressure (KPa)
p_diff_kpa=p_diff*0.001;
% Pressure Differential (Pa)
delta_p_diff=abs(p_t_atm-p_diff);
% Pressure Differential (KPa)
delta_p_diff_kpa=abs(p_t_atm_kpa-(p_diff_kpa));
%% Pressure Differential in Settling Chamber
% Total Pressure (Pa)
p_t_sc=p_t_atm + ((K_exit+K_ts)*q_ts) + (K_con*q_con) + ...
    ((K_sc+K_honey+K_screens)*q_sc);
% Total Pressure (KPa)
p_t_sc_kpa=p_t_sc*0.001;
% Local Static Pressure Denominator
p_sc_den=(1+(W_2*(M_sc^2)))^W_1;
% Local Static Pressure (Pa)
p_sc=p_t_sc/p_sc_den;
% Local Static Pressure (KPa)
p_sc_kpa=p_sc*0.001;
% Pressure Differential (Pa)
delta_p_sc=abs(p_t_atm-p_sc);
% Pressure Differential (KPa)
delta_p_sc_kpa=delta_p_sc*0.001;
%% Pressure Differential in the Contraction
% Total Pressure (Pa)
p_t_con=p_t_atm + ((K_exit+K_ts)*q_ts) + (K_con*q_con);
% Total Pressure (KPa)
p_t_con_kpa=p_t_sc*0.001;
% Local Static Pressure Denominator
p_con_den=(1+(W_2*(M_con^2)))^W_1;
% Local Static Pressure (Pa)
p_con=p_t_con/p_con_den;
% Local Static Pressure (KPa)
p_con_kpa=p_con*0.001;
% Pressure Differential (Pa)
delta_p_con=abs(p_t_atm-p_con);
% Pressure Differential (KPa)
delta_p_con_kpa=abs(p_t_atm_kpa-p_con_kpa);
%% Pressure Differential in the Test Section
% Total Pressure (Pa)
p_t_ts=p_t_atm + ((K_exit+K_ts)*q_ts);
% Total Pressure (KPa)
p_t_ts_kpa=p_t_ts*0.001;
% Local Static Pressure Denominator
p_ts_den=(1+(W_2*(M_o^2)))^W_1;
% Local Static Pressure (Pa)
p_ts=p_t_ts/p_ts_den;
% Local Static Pressure (KPa)
p_ts_kpa=p_ts*0.001;
% Pressure Differential (Pa)
delta_p_ts=abs(p_t_atm-p_ts);
% Pressure Differential (KPa)
delta_p_ts_kpa=abs(p_t_atm_kpa-p_ts_kpa);
%% Calculating P_statics + q_local
```

```
% In Pa
p_fan_q=p_fan+q_fan;
p_diff_q=p_diff+q_diff;
p_sc_q=p_sc+q_sc;
p_con_q=p_con+q_con;
p_ts_q=p_ts+q_ts;

% In Kpa
p_fan_q_kpa=p_fan_kpa+q_fan_kpa;
p_diff_q_kpa=p_diff_kpa+q_diff_kpa;
p_sc_q_kpa=p_sc_kpa+q_sc_kpa;
p_con_q_kpa=p_con_kpa+q_con_kpa;
p_ts_q_kpa=p_ts_kpa+q_ts_kpa;



%% Pressure Check
% Diffuser Pressure Check Location
x_p_diff=fan_duct_length;
% Settling Chamber Pressure Check Location
x_p_sc=diff_length+sc_length;
% Contraction Pressure Check Location
x_p_con=diff_length+sc_length+con_length;
% Test Section Pressure Check Location
x_p_ts=diff_length+sc_length+con_length;
% Pressure Check Locations (m)
x_p_values=[x_p_diff x_p_diff x_p_sc x_p_con x_p_ts];
% Static Pressures (Pa)
p_values=[p_fan p_diff p_sc p_con p_ts];
% Static Pressures (KPa)
p_values_kpa=[p_fan_kpa p_diff_kpa p_sc_kpa p_con_kpa p_ts_kpa];
% P_static+local_q (Pa)
p_static_q_values=[p_fan_q p_diff_q p_sc_q p_con_q p_con_q];
% P_static+local_q (KPa)
p_static_q_values_kpa=[p_fan_q_kpa p_diff_q_kpa p_sc_q_kpa p_con_q_kpa
p_con_q_kpa];
%P_total in the Fan Duct (Pa)
p_total_fan=[p_t_fan p_t_fan p_t_fan p_t_fan p_t_fan];
%P_total in the Fan Duct (Kpa)
p_total_fan_kpa=[p_t_fan_kpa p_t_fan_kpa p_t_fan_kpa p_t_fan_kpa
p_t_fan_kpa];
% P_total in the Diffuser (Pa)
p_total_diff=[p_t_diff p_t_diff p_t_diff p_t_diff p_t_diff];
% P_total in the Diffuser (KPa)
p_total_diff_kpa=[p_t_diff_kpa p_t_diff_kpa p_t_diff_kpa p_t_diff_kpa
p_t_diff_kpa];
% P_total in the Settling Chamber (Pa)
p_total_sc=[p_t_sc p_t_sc p_t_sc p_t_sc p_t_sc];
% P_total in the Settling Chamber (KPa)
p_total_sc_kpa=[p_t_sc_kpa p_t_sc_kpa p_t_sc_kpa p_t_sc_kpa
p_t_sc_kpa];
% P_total in the contraction (Pa)
p_total_con=[p_t_con p_t_con p_t_con p_t_con p_t_con];
% P_total in the contraction (KPa)
```

```
p_total_con_kpa=[p_t_con_kpa p_t_con_kpa p_t_con_kpa p_t_con_kpa
p_t_con_kpa];
% P_total in the Test Section (Pa)
p_total_ts=[p_t_ts p_t_ts p_t_ts p_t_ts p_t_ts];
% P_total in the Test Section (KPa)
p_total_ts_kpa=[p_t_ts_kpa p_t_ts_kpa p_t_ts_kpa p_t_ts_kpa
p_t_ts_kpa];

% Pressure Check Plot (Kpa)
plot(x_p_values,p_values_kpa,'--o',x_p_values,p_static_q_values_kpa,'--
x',...
    x_p_values,p_total_fan_kpa,'--*',x_p_values,p_to-
tal_diff_kpa,x_p_values,p_total_sc_kpa,x_p_values,...
    p_total_con_kpa,x_p_values,p_total_ts_kpa);
xlabel('Location (m)');
ylabel('Pressure (Kpa)');
title('Pressure Check');
legend('p static', 'p-static + q-local','Total p at Fan Duct Out-
let',...
    'Total p at Diff Inlet','Total p in SC','Total p at Con Outlet',...
    'Total P in TS','Location','southwest');

%% Plotting the Pressure differential along the Length of the Tunnel
%Note: STATIC inside tunnel to ambient pressure.


%Test Section Length
l_t=7.069;

% Pressure Differential Locations (m)
x_p_values=[x_p_diff x_p_sc x_p_con]./l_t;

% P_Differentials (Kpa)
p_differential_kpa=[delta_p_diff_kpa delta_p_sc_kpa...
    delta_p_con_kpa];
%Creating Plot
figure
plot(x_p_values,p_differential_kpa,'--x')
%Axes Labels
xlabel('x/L_t')
ylabel('\Delta P_w (kPa gauge)');
% Title
%title('Wall Pressure Differential');

%Creating Labels for each point
%Fan Duct Outlet
% lab_x1=x_p_diff;
% lab_y1=delta_p_fan_kpa;
% label_1='Fan Duct Outlet \rightarrow   ';
% text(lab_x1,lab_y1,label_1,'HorizontalAlignment','right');
%Diffuser Inlet
lab_x2=x_p_diff/l_t;
lab_y2=delta_p_diff_kpa;
label_2='   \leftarrow Diffuser Inlet';
text(lab_x2,lab_y2,label_2);
```

```
%Settling Chamber
lab_x3=x_p_sc/l_t;
lab_y3=delta_p_sc_kpa;
label_3='   \leftarrow Settling Chamber';
text(lab_x3,lab_y3,label_3);
set(gcf,'color','w');
set(gca,'fontsize',12)
set(gca,'FontName','Times New Roman')
set(gcf,'units','points','position',[300 300 350 250])
%Contraction Outlet/Test Section
lab_x4=x_p_con/l_t;
lab_y4=delta_p_ts_kpa;
label_4='Test Section Inlet \rightarrow  ';
text(lab_x4,lab_y4,label_4,'HorizontalAlignment','right');

%% Mass and Volumetric Flow Rates
% Mass Flow Rate(m_dot)= rho*V*A (Should Be Constant throughout the
Tunnel)

% Mass Flow Rate at the Fan Duct Outlet
m_dot_fan=rho*V_fan*A_o_fan;
% Mass Flow Rate at the Diffuser Inlet
m_dot_diff=rho*V_diff*A_i_diff;
% Mass Flow Rate through the Grids
m_dot_grids=m_dot_diff;
% Mass Flow Rate through the Settling Chamber
m_dot_sc=rho*V_sc*A_sc;
% Mass Flow Rate through the Honeycomb
m_dot_honey=m_dot_sc;
% Mass Flow Rate through the Screens
m_dot_screens=m_dot_sc;
% Mass Flow Rate at the Contraction Outlet
m_dot_con=rho*V_con*A_o_con;
% Mass Flow Rate through the Test Section
m_dot_ts=rho*V_o*A_ts;
% Mass Flow Rate at the Exit
m_dot_exit=m_dot_ts;

% Volumetric Flow Rate (v_dot)=V*A (Should Be Const.)
% Volume Flow Rate at the Fan Duct Outlet
v_dot_fan=V_fan*A_o_fan;
% Volume Flow Rate at the Diffuser Inlet
v_dot_diff=V_diff*A_i_diff;
% Volume Flow Rate through the Grids
v_dot_grids=v_dot_diff;
% volume Flow Rate through the Settling Chamber
v_dot_sc=V_sc*A_sc;
% Volume Flow Rate through the Honeycomb
v_dot_honey=v_dot_sc;
% Volume Flow Rate through the Screens
v_dot_screens=v_dot_sc;
% Volume Flow Rate at the Contraction Outlet
v_dot_con=V_con*A_o_con;
% Volume Flow Rate through the Test Section
v_dot_ts=V_o*A_ts;
% Volume Flow Rate at the Exit
```

```
v_dot_exit=v_dot_ts;

%% Putting the Inputs into a table
% Defining the Figure
f_1=figure('Name', 'Input Summary', 'Position', [400 400 450 200]);
% 1st Row
T1_R1={'Fan Duct Inlet Width',fan_i_width,'Test Section Speed
(m/s)',V_o...
    ,'Grid Open Area (%)',grids_open_area_percentage};
% 2nd Row
T1_R2={'Fan Duct Inlet Height',fan_i_height,'Density (kg/m^3)',rho,...
    'Number of Grids',num_of_grids};
% 3rd Row
T1_R3={'Fan Duct Length',fan_duct_length,'Dynamic Viscosity (kg/m-
s)'...
    ,mew,'Length of Each Grid (m)',grid_length};
% 4th Row
T1_R4={'Diffuser Inlet Width',diff_i_width,'Specific Heat Ra-
tio',gamma,...
    'Mesh Open Area (%)',mesh_open_area_percentage};
% 5th Row
T1_R5={'Diffuser Inlet Height',diff_i_height,'Blower Efficiency
(%)',...
    eta_f_percent,'Number of Screens',num_of_screens};
% 6th Row
T1_R6={'Diffuser Outlet Width',diff_o_width,'Atmospheric Pressure
(Kpa)',...
    p_t_atm_kpa,'Screen Wire Diameter (m)',screen_wire_diameter};
% 7th Row
T1_R7={'Diffuser Outlet Height',diff_o_height,'','','Honeycomb Cell
Size (m)',cell_size};
% 8th Row
T1_R8={'Diffuser Length',diff_length,'','','Honeycomb Length
(m)',cell_length};
% 9th Row
T1_R9={'Settling Chamber Width',sc_width,'','','Surface Roughness
(m)',...
    roughness};
% 10th Row
T1_R10={'Settling Chamber Height',sc_height,'','','Honeycomb Porosity
(%)',...
    beta_h_percentage};
% 11th Row
T1_R11={'Settling Chamber Length',sc_length,'','','',''};
% 12th Row
T1_R12={'Contraction Inlet Width',con_i_width,'','','',''};
% 13th Row
T1_R13={'Contraction Inlet Height',con_i_height,'','','',''};
% 14th Row
T1_R14={'Contraction Outlet Width',con_o_width,'','','',''};
% 15th Row
T1_R15={'Contraction Outlet Height',con_o_height,'','','',''};
% 16th Row
T1_R16={'Contraction Length',con_length,'','','',''};
% 17th Row
T1_R17={'Test Section Width',ts_width,'','','',''};
% 18th Row
```

```
T1_R18={'Test Section Height',ts_height,'','','',''};
%19th Row
T1_R19={'Test Section Length',ts_length,'','','',''};
% Table Data
dat_1=[T1_R1;T1_R2;T1_R3;T1_R4;T1_R5;T1_R6;T1_R7;T1_R8;T1_R9;T1_R10;...
    T1_R11;T1_R12;T1_R13;T1_R14;T1_R15;T1_R16;T1_R17;T1_R18;T1_R19];
%Column Labels
T1_column={'          Geometry Inputs (m)         ','Values',...
    '            Fluid Inputs             ','Values',...
    '          Flow Straightener Inputs          ','Values'};

% Width of Column
column_width={'auto','auto','auto'};
% Putting Everything in a UItable
T_1=uitable('Units','Normalized','ColumnWidth',column_width,...
    'Position',[.2 .1 1.9 .9],'Data', dat_1,'ColumnName', T1_column);




%% Putting the Results in a table
% 1st Row
T2_R1={K_fan,K_diff K_grids K_honey K_sc K_screens K_con ...
    K_ts K_exit K_total};
% 2nd Row
T2_R2={Ko_fan,Ko_diff Ko_grids Ko_honey Ko_sc Ko_screens Ko_con ...
    Ko_ts Ko_exit Ko_total};
% 3rd Row
T2_R3={A_o_fan,A_i_diff A_i_diff A_sc A_sc A_sc A_o_con A_ts A_ts ''};
% 4th Row
T2_R4={q_fan_kpa,q_diff_kpa q_diff_kpa q_sc_kpa q_sc_kpa q_sc_kpa
q_con_kpa ...
    q_ts_kpa q_ts_kpa ''};
% 5th Row
T2_R5={p_fan_kpa p_diff_kpa  p_diff_kpa p_sc_kpa p_sc_kpa p_sc_kpa ...
    p_con_kpa p_ts_kpa p_ts_kpa ''};
% 6th Row
T2_R6={p_t_fan_kpa p_t_diff_kpa p_t_diff_kpa p_t_sc_kpa p_t_sc_kpa
p_t_sc_kpa ...
    p_t_con_kpa p_t_ts_kpa p_t_ts_kpa ''};
% 7th Row
T2_R7={M_fan M_diff M_grids M_honey M_sc M_screens M_con M_o M_o ''};
% 8th Row
T2_R8={V_fan V_diff V_diff V_sc V_sc V_sc V_con V_o V_o ''};
% 9th Row
T2_R9={m_dot_fan m_dot_diff m_dot_grids m_dot_honey m_dot_sc
m_dot_screens ...
    m_dot_con m_dot_ts m_dot_exit ''};
% 10th Row
T2_R10={v_dot_fan v_dot_diff v_dot_grids v_dot_honey v_dot_sc
v_dot_screens ...
    v_dot_con v_dot_ts v_dot_exit ''};
% 11th Row
T2_R11={Dh_fan Dh_diff '' Dh_honey Dh_sc '' Dh_con Dh_ts '' ''};
% 12th Row
T2_R12={RN_fan RN_diff '' RN_sc RN_sc '' RN_con RN_ts '' ''};
```

```
% 13th Row
T2_R13={lambda_fan lambda_diff '' lambda_honey lambda_sc '' lambda_con
lambda_ts ...
    '' ''};
% 14th Row
T2_R14={'' '' '' '' '' '' '' '' '' P_Input};
% 15th Row
T2_R15={'' '' '' '' '' '' '' '' '' P_Input_kw};
% 16th Row
T2_R16={'' '' '' '' '' '' '' '' '' P_Required};
% 17th Row
T2_R17={'' '' '' '' '' '' '' '' '' P_Required_kw};


% Defining the Figure
f_2=figure('Name', 'Result Summary', 'Position', [400 400 450 200]);

% Table Data
dat_2=[T2_R1;T2_R2;T2_R3;T2_R4;T2_R5;T2_R6;T2_R7;T2_R8;T2_R9;T2_R10;...
    T2_R11;T2_R12;T2_R13;T2_R14;T2_R15;T2_R16;T2_R17];
% Labels for Each Column
T2_column={'Fan Duct (Outlet)','Diffuser (Inlet)','Grids','Honey-
comb','Settling Chamber','Screens',...
    'Contraction (Outlet)','Test Section','Exit','Total'};

% Labels for Each Row
T2_row={'K','Ko','A (m^2)','Dynamic Pressure (Kpa)','Static Pressure
(Kpa)',...
    'Total Pressure (Kpa)','Mach Number','V (m/s)','mdot (kg/s)','vdot
(m^3/s)',...
    'Dh (m)','Re_Dh','Friction Coefficient','Power Input (HP)','Power
Input (kW)',...
    'Power Requirement (HP)','Power Requirement (kW)'};


% Putting Everything in a UItable
T_2=uitable('Units','Normalized','Position',[.2 .1 1.9 .9],'Data',
dat_2,...
   'ColumnName', T2_column,'RowName',T2_row);
```